



ulm university universität
uulm

**Fakultät für
Naturwissenschaften**

Institute of Theoretical
Physics

The Effects of Casimir Interactions in Experiments on Gravitationally-induced Entanglement

Bachelor Thesis

Submitted by:

Jan Bulling
jan.bulling@uni-ulm.de
1109395

Supervised by:

Marit O. E. Steiner, Julen S. Pedernales, Martin B. Plenio

In this work it was shown by calculating the relative dynamical phase build-up, that Casimir interactions between a conducting Faraday shield and macroscopic Schrödinger-cat states can destroy measurable entanglement due to stochastic variations in the initial setup and due to the thermal motion of the shield.

Contents

1	Introduction	5
1.1	Feynman's Gedankenexperiment	5
2	A first look	6
2.1	Time evolution under a gravitational potential	10
2.2	Entanglement measures	11
2.3	Issues with the idealized experimental procedure	15
3	Casimir effect	17
3.1	Proximity force approximation	19
3.2	Casimir forces between a conducting plate and a dielectric sphere	21
3.3	Imperfect plate and spheres	23
4	The particle in front of a static shield	26
4.1	Entanglement generation	29
4.2	The optimal setup	34
4.2.1	Orientation	34
4.2.2	Separation, mass and superposition size	40
4.3	Trapping the particle	43
4.4	Discussions	48
5	The consequences of a thermal shield	50
5.1	Thickness and size of the shield	50
5.1.1	Shielding Coulomb-Interactions	51
5.1.2	Shielding Casimir-Interactions	53
5.1.3	Gravitational effects of the shield	54
5.2	Thermal shield vibrations	54
5.3	Entanglement in front of a thermal shield	57
5.3.1	Analytic dynamics	61
5.3.2	Small shields	66
5.4	Discussions of the effects of the thermal shield	67
6	Discussion and outlook	69
	Bibliography	72

Contents

A	Ancillary calculations	78
A.1	Evolution under a gravitational Hamiltonian	78
A.1.1	Using time dependent perturbation theory	78
A.1.2	Using an exact time evolution	79
A.2	Exemplary calculation of E_N	79
A.3	Polarizability of a dielectric sphere	80
A.4	Blocking of the shield	81
A.5	Thermal harmonic oscillator	82
B	Primary calculations	83
B.1	Average density matrix	83
B.2	Density matrix vibrating plate	85
B.3	Time evolution in front of a thermal plate	86
C	Additional figures	88

1 Introduction

Newton (1687)

Keplers law are inverse square of gravitational force

Maskelyne (1774) Gravitational force of a mountain [1, 2]

Cavendish (1798) Gravitational force via torsion pendulum

1.1 Feynman's Gedankenexperiment

2 A first look

Testing the quantum nature of gravity is no easy task and many proposals seek to detect gravitationally induced entanglement between two masses [3–6] as a form of proof. For all these proposals, gravity is assumed to be mediated by a gravitational field. During a time evolution, this field (like any other external field) can only perform local operations (LO) on the states of the test masses. If gravity is now assumed to behave classically, the propagation between the masses can be described by a classical communication (CC) channel [6, 7]. These LOCC operations however cannot turn an initially unentangled state into an entangled one [8, 9]. It immediately follows, that if one measures the involved masses to be entangled after a mutual gravitational interaction, gravity necessarily has to be quantum in some way. It is important to note, that the opposite of this statement is not true. Measuring unentangled masses does not directly imply the classicality of the gravitational field. This can be seen by considering operations that are non-LOCC and also produce unentangled states like for example the swap operation $|\psi\rangle_A |\phi\rangle_B \rightarrow |\phi\rangle_A |\psi\rangle_B$. This operations obviously can't induce entanglement to initially unentangled states, but requires the perfect exchange of quantum information between the states - which is not possible using classical communication alone. In other words: If one prepares masses initially in a pure product state and measures *any* state which cannot be obtained by LOCC-operations after some final time evolution, it is impossible for gravity to behave classical. One can even go so far and define the term ***quantum gravity*** as any interaction mediated by gravity that cannot be described by LOCC operations alone [7].

A plausible and logical idea for an experiment to test for gravitational induced entanglement is described in this chapter - which is, as a reminder, enough to prove a quantum nature of gravity. It requires the generation of coherent delocalized quantum superpositions of massive objects either as so-called Schrödinger-cat states or squeezed gaussian states [6, 10]. Theses masses are brought close enough together for gravity to have a measurable effect. The distances between different parts of the spatial superpositions must have different distances to the delocalized second mass. As a result - and of course *if gravity behaves quantum* - the states should get entangled. To see this, consider the ideal simplification of a real experimental setup where two bodies with mass m are trapped in an harmonic potential well (like for example an levitated particle in an optical or magnetic trap) with frequency ω separated by a distance d . The local Hamiltonian of the system is given by

$$\hat{H}_0 = \sum_{i=1,2} \frac{\hat{p}_i^2}{2m} + \frac{1}{2}m\omega^2 \hat{x}_i^2 \quad (2.1)$$

where \hat{x} and \hat{p} are the position and momentum operators satisfying the canonical commutation relation $[\hat{x}_i, \hat{p}_j] = i\hbar\delta_{ij}$. For now, all non-gravitational interactions between the masses have been ignored. In the low energy regime, where the energy transfer during a process is far below the Planck scale $m_p c^2 \sim 10^{19}$ GeV, gravity can be traded as an effective field theory with tools available similar to those for the electromagnetic field and QED [11]. In the non-relativistic limit $v \ll c$, the gravitational interaction can be described by a Newtonian $1/r$ potential acting on the center-of-mass positions, with all classical quantities are replaced by quantum operators [10–12]. Spatial superpositions lead to superpositions of the metric and consequently (in the non-relativistic limit) to a superposed Newtonian potential. The interaction Hamiltonian \hat{H}_G should therefore be describable by

$$\hat{H}_G = -\frac{Gm^2}{|d - \hat{x}_1 + \hat{x}_2|}, \quad (2.2)$$

where $G = 6.6743 \times 10^{-11} \text{ m}^3\text{kg}^{-1}\text{s}^{-2}$ is the gravitational constant. The separation of the masses d is chosen much larger than the extension of the delocalization (in this setup comparable to the position variance of the harmonic oscillator). This condition is realistic given that the biggest spatial delocalization ever achieved in matter wave experiments is in the order of 500 nm [13]. Expanding the Hamiltonian \hat{H}_G for small \hat{x}_i , only the second order term proportional to $(\hat{x}_1 - \hat{x}_2)^2$ can induce entanglement [3]. The zeroth order term is just a overall energy offset, the first order term $\propto (\hat{x}_1 - \hat{x}_2)$ as well as the terms \hat{x}_i^2 result only in a local interaction for each mass separately. The coupling term $-(\hat{x}_1\hat{x}_2 + \hat{x}_2\hat{x}_1) = -2\hat{x}_1\hat{x}_2$ however is very interesting as it couples both oscillators and can thus mediate entanglement. Introducing the ladder operators, the Hamiltonian $\hat{H} = \hat{H}_0 + \hat{H}_G$ can be expressed as [11]:

$$\hat{H} = \sum_{i=1,2} \hbar\omega\hat{a}_i^\dagger\hat{a}_i - \frac{Gm^2}{d^3} \left(\sqrt{\frac{\hbar}{2m\omega}} \right)^2 (\hat{a}_1\hat{a}_2 + \hat{a}_1\hat{a}_2^\dagger + \hat{a}_1^\dagger\hat{a}_2 + \hat{a}_1^\dagger\hat{a}_2^\dagger) \quad (2.3)$$

Applying the *rotating-wave approximation*¹, the terms $\hat{a}_1\hat{a}_2 + \hat{a}_1^\dagger\hat{a}_2^\dagger$ can be dropped. Defining the coupling strength g of the interaction as $g = Gm/\omega d^3$, eq (2.3) can be rewritten as

$$\hat{H} = \sum_{i=1,2} \hbar\omega\hat{a}_i^\dagger\hat{a}_i - \hbar g (\hat{a}_1\hat{a}_2^\dagger + \hat{a}_1^\dagger\hat{a}_2). \quad (2.4)$$

Now, for simplicity and as a simple example, the evolution of the initial Fock state $|\psi(0)\rangle = |10\rangle$ is considered. The gravitational interaction H_G can be treated as a time dependent perturbation and the state evolution is given as (for calculation see appendix A.1.1) [11]

$$|\psi(t=0)\rangle = |10\rangle \xrightarrow{\text{time } t} |\psi(t)\rangle = \mathcal{N} \left(|10\rangle - igt |01\rangle + \mathcal{O}(g^2) \right) \quad (2.5)$$

¹This approximation is known from quantum optics, where all fast oscillating terms in the Hamiltonian can be dropped [7, 11]. In the interaction picture, the ladder operators evolve as $\hat{a}(t) = \hat{a}e^{-i\omega t}$. The terms like $\hat{a}_1(t)\hat{a}_2(t)$ oscillate with frequency 2ω whereas $\hat{a}_1^\dagger(t)\hat{a}_2(t)$ does not oscillate at all. Due to the small coupling, this approximation works very well here.

where \mathcal{N} is an appropriate normalization constant. The evolved state (2.5) is entangled and cannot be reduced into a product of two oscillator Fock states. The entanglement is very small since it is proportional to the gravitational coupling constant gt ². Another interesting result, which underlines the false inference of a classical gravity from observed non-entanglement discussed above can be seen by considering the time evolution of a coherent product state $|\alpha\rangle \otimes |\beta\rangle$ where $\hat{a}|\alpha\rangle = \alpha|\alpha\rangle$. The time evolution is derived in appendix A.1.2 and results in

$$e^{-i\hat{H}t/\hbar}(|\alpha\rangle \otimes |\beta\rangle) = |e^{-i\omega t}(\alpha \cos gt - \beta \sin gt)\rangle \otimes |e^{-i\omega t}(-\alpha \sin gt + \beta \cos gt)\rangle. \quad (2.6)$$

This state is clearly a product state and thus not entangled. But for a time $t_0 = \pi/2g$ the state is effectively the swapped initial state $|\beta\rangle \otimes |\alpha\rangle$ up to a local phase. This swap operation is however, as established earlier, not possible under a LOCC protocol. Thus, even if the resulting state after time evolution under a gravitational interaction is unentangled, we can rule out the classicality of gravity [7, 11]. Gravity must therefore be capable of transmitting quantum information and must be described by a quantum channel.

Experimentally, one requires the ability to generate spatial superpositions of two massive objects with large enough coherence times. Usually the weak gravitational interaction requires coherence times in the order of 100 ms – 10 s for any meaningful and measurable entanglement to build up. The masses should additionally be massive enough for their gravitational effects to be measurable. These requirements impose huge experimental and engineering challenges. To contextualize: The most massive object ever put into a spatial superposition in matter-wave interferometry is in the order of 4×10^{-23} kg [13], whereas the smallest object whose gravitational field has been measured was just below 100 mg [14] - a difference of 19 orders of magnitude. One way to experimentally create such spatial superpositions is giving the masses a spin-1/2 degree of freedom. For example, a nitrogen-vacancy diamonds can be used [6], where the NV site provides the required spin of 1/2. An applied magnetic gradient $\partial_x B$ functions like a “beam splitter” and creates a delocalized state. The extend of this superposition can be calculated and separations in the order of 100 μ m are theoretically achievable [6]. Levitated, trapped particles isolated and shielded in a vacuum can increase environmental isolation by avoiding contact with surrounding noise. The additional forces due to the trapping potential or the gravitational acceleration can be studied in advance. In this thesis, I assume that all required states and superpositions can be prepared experimentally.

The general and idealized problem considered is illustrated in fig. 2.1. Two massive bodies with masses M_A and M_B are initially separated by a center-to-center distance $2L$. The masses are prepared in a coherent delocalized quantum superposition Schrödinger-cat-like state in, for now, a parallel orientation as depicted in fig. 2.1. The extension of the superposition is denoted by Δx and is the same for both masses. It is important to choose the positions of the masses such that the distances between each part of the

²The amount of entanglement can for example be quantified with the later introduced *logarithmic negativity* E_N . For this state, it is given by $E_N(|\psi(t)\rangle\langle\psi(t)|) \simeq 2tg/\log 2 + \mathcal{O}(g^2) \geq 0$.

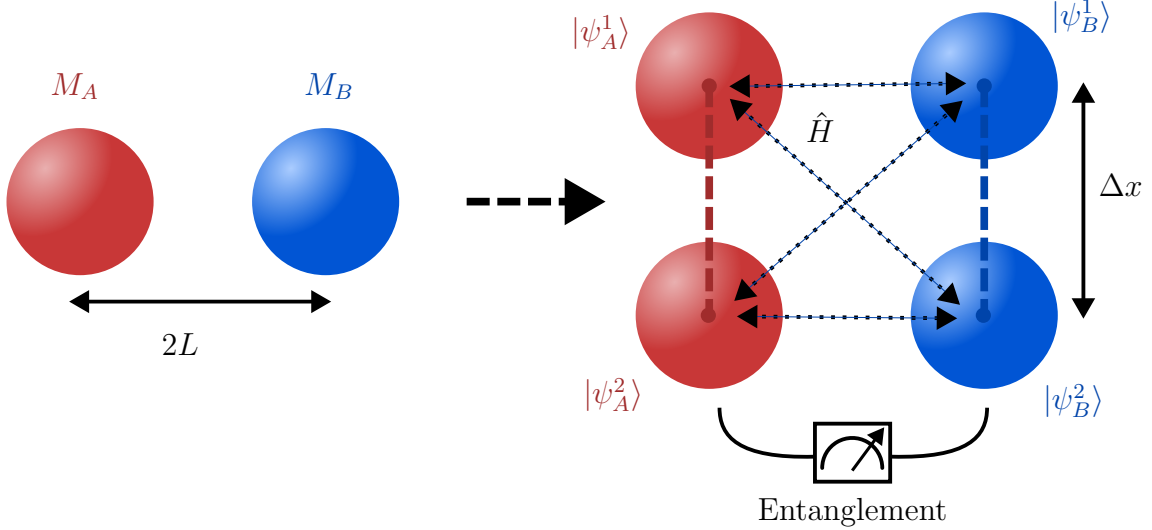


Figure 2.1: Schematic figure of the proposed experiment with two masses prepared in a spatial superposition state. The gravitational interaction \hat{H} induces different phases to each of the superpositions due to the different distances between all masses. This results in measurable entanglement after some time evolution.

delocalized mass A and B are not always identical. Otherwise, all built up phases are the same and no entanglement is observable. With the notation introduced in fig. 2.1, the initial state at $t = 0$ is given by

$$|\psi(t=0)\rangle = \frac{1}{2} (|\psi_A^1\rangle + |\psi_A^2\rangle) \otimes (|\psi_B^1\rangle + |\psi_B^2\rangle). \quad (2.7)$$

The state evolves under a Hamiltonian \hat{H} and after some time the position of each mass is measured and checked for entanglement. For now I assume that all interactions except gravity can be neglected. In reality, electromagnetic forces and Casimir-Polder interactions [15, 16] need to be considered.

As established earlier in this chapter, with some assumptions made, gravitational interaction can generate entanglement. In the time scales of the experiment, the acceleration of the masses due to the mutual gravitational interaction can be neglected³. The Hamiltonian therefore only needs to include the gravitational potential

$$\hat{V} = -\frac{GM_A M_B}{|\hat{D}|} \quad (2.8)$$

where \hat{D} is the distance operator between the masses. It depends on the individual positions \hat{x}_A and \hat{x}_B . During time evolution, the different parts of the superpositions

³Take for example a silica sphere ($\rho = 2648 \text{ kg/m}^3$) with $R = 10^{-5} \text{ m}$ separated by $2L = 4R$. The mutual gravitational acceleration for each sphere is around $a = GM/(2L)^2 = 5 \times 10^{-13} \text{ m/s}^2$ which results for $t \sim 1 \text{ s}$ in a distance traveled of $\sim 10^{-13} \text{ m}$.

built up different local phases. I am interested in calculating, how much entanglement one can expect from this kind of interactions.

2.1 Time evolution under a gravitational potential

Proposition 2.1. *The time evolution under a static and constant Hamiltonian $\hat{H} = \hat{V}(\hat{x}_i) = \text{const.}$ is given by the eigenenergies of the system $\hat{V} |n\rangle = V_n |n\rangle$ proportional to $e^{-iV_n t/\hbar}$.*

Proof. This is a trivial statement. The time evolution is governed by the Schrödinger equation

$$i\hbar \frac{\partial}{\partial t} |\psi(t)\rangle = \hat{H} |\psi(t)\rangle. \quad (2.9)$$

The formal solution of this first order PDE is given by

$$|\psi(t)\rangle = e^{-i\hat{V}t/\hbar} |\psi(t=0)\rangle. \quad (2.10)$$

The constant (hermitian) potential operator can be expressed in the energy-eigenbasis $\{|n\rangle\}$ as $\hat{V} |n\rangle = V_n |n\rangle$. The initial state can be expressed as a superposition in the same eigenstates like $|\psi\rangle = \sum_n c_n |\psi_n\rangle$. Putting both together and using the Taylor expansion of the exponential function, one arrives at the simple form

$$|\psi(t)\rangle = \sum_n e^{-i\hat{V}t/\hbar} |n\rangle \langle n|\psi\rangle = \sum_{n,k} \frac{(-i\hat{V}t/\hbar)^k}{k!} |n\rangle c_n |\psi_n\rangle \quad (2.11)$$

$$= \sum_{n,k} \frac{(-iV_n t/\hbar)^k}{k!} c_n |\psi_n\rangle = \sum_n e^{-iV_n t/\hbar} c_n |\psi_n\rangle \quad (2.12)$$

where in the second to last step $\hat{V}^k |n\rangle = \hat{V}^{k-1} \hat{V} |n\rangle = \hat{V}^{k-1} |n\rangle V_n = \dots = V_n^k |n\rangle$ was used. \square

Using the preceding proposition, the initial state eq. (2.7) can be evolved in time. The potential operator eq. (2.8) acts on every state in the $\{|\psi_A^1\rangle, |\psi_A^2\rangle\} \otimes \{|\psi_B^1\rangle, |\psi_B^2\rangle\}$ basis differently. This is because of the different distances between the states $|\psi_A^i\rangle$ and $|\psi_B^j\rangle$ for different $i, j \in \{1, 2\}$. This results in phases ϕ_{ij} to be built up during time evolution according to proposition 2.1. The state $|\psi(t)\rangle$ after some time evolution is therefore given as

$$|\psi(t)\rangle = \frac{1}{2} \left(e^{i\phi_{11}} |\psi_A^1\rangle |\psi_B^1\rangle + e^{i\phi_{12}} |\psi_A^1\rangle |\psi_B^2\rangle + e^{i\phi_{21}} |\psi_A^2\rangle |\psi_B^1\rangle + e^{i\phi_{22}} |\psi_A^2\rangle |\psi_B^2\rangle \right), \quad (2.13)$$

where the \otimes symbol was omitted. The phases are

$$\phi \equiv \phi_{11} = \phi_{22} = \frac{GM_A M_B}{2\hbar L} t \quad \text{and} \quad \phi_{12} = \phi_{21} = \frac{GM_A M_B}{\hbar \sqrt{4L^2 + (\Delta x)^2}} t. \quad (2.14)$$

Assuming again that the superposition size Δx is much smaller than the distance L between the masses - like before in eq. (2.2) - the phases $\phi_{12} = \phi_{21}$ can be expanded and a global phase ϕ can be factored:

$$\phi_{12} = \phi_{21} \approx \frac{GM_A M_B}{\hbar} \left[\frac{1}{2L} - \frac{(\Delta x)^2}{16L^3} \right] t \equiv \phi - \Delta\phi. \quad (2.15)$$

The state eq. (2.13) can now be expressed in the form

$$|\psi(t)\rangle = e^{i\phi} \frac{1}{\sqrt{2}} \left[|\psi_A^1\rangle \otimes \frac{|\psi_B^1\rangle + e^{-i\Delta\phi} |\psi_B^2\rangle}{\sqrt{2}} + |\psi_A^2\rangle \otimes \frac{e^{-i\Delta\phi} |\psi_B^1\rangle + |\psi_B^2\rangle}{\sqrt{2}} \right], \quad (2.16)$$

where the entanglement dynamics can be directly seen. This state is entangled, if it is not representable as a product state $|\psi\rangle \neq |\psi_A\rangle \otimes |\psi_B\rangle$. That is the case, if the states containing $|\psi_B^i\rangle$ are not both equal to each other (i.e. differ only by a phase) and thus cannot be factored. The system is therefore entangled, if and only if $\Delta\phi \neq k\pi$ with integer $k \in \mathbb{Z}$.

In order to assess in a more quantitative way how entangled the state $|\psi\rangle$ is, a more sophisticated entanglement measure is needed. In the next chapter, the **logarithmic negativity** is motivated and introduced. In the rest of this thesis, I will repeatedly opt for this measure.

2.2 Entanglement measures

Checking whether an arbitrary state ρ is entangled or not is no easy task. In fact, this problem is known to be NP-hard [17]. A state $\rho_{AB} \in \mathcal{H}_A \otimes \mathcal{H}_B$ is called entangled, if it is **non-separable**, that is, it cannot be expressed as a tensor product of two subsystems $\rho_A \in \mathcal{H}_A$ and $\rho_B \in \mathcal{H}_B$. Only for specific cases - like the case of two qubits or qubit-qutrit - a simple sufficient criterion for determining the separability of a general mixed state is known: The positive partial transpose (PPT) criterion states, that if the partial transpose of the density matrix is positive ($\rho^{\Gamma_A} > 0$ ⁴), the state ρ is separable [8, 9]. In other words, if ρ^{Γ_A} has negative eigenvalues, ρ is guaranteed to describe an entangled state. The inverse is true, if and only if the dimension of $\rho_A \otimes \rho_B$ is 2×2 or 3×2 [8] - otherwise, only having non-negative eigenvalues doesn't necessarily result in an unentangled system (such states are called "bound states"). The partial transpose with respect to a subsystem i can be understood in the same way as the partial trace, where the operation (in this case the transform) is performed only on indices corresponding the subsystem ρ_i . To see the necessity of the PPT criterion, consider a separable mixed state ρ , which can be generally expressed as

$$\rho = \sum p_i \rho_A^i \otimes \rho_B^i. \quad (2.17)$$

⁴A matrix is defined as positive ("positive definite"), if all eigenvalues are positive.

The partial transpose is in this case trivial:

$$\rho^{\Gamma_A} = \sum p_i (\rho_A^i)^T \otimes \rho_B^i. \quad (2.18)$$

Since the transpose preserves eigenvalues, the transposed subsystem A is still positive $(\rho_A^i)^T > 0$ and describes again a valid quantum state. It follows, that ρ^{Γ_A} is positive as well. If somehow ρ^{Γ_A} has any negative eigenvalues, this can only mean that the initial state ρ is not separable and cannot be expressed in the form of eq. (2.17) and the necessity of the criterion is shown.

For quantifying entanglement in a more precise way, a mathematical quantity called **entanglement measure** can be used. A good measure should be able to capture the essential features of entanglement. One can axiomatically state what properties such a measure $E(\rho)$ should have [8, 9]:

Normalization An entanglement measure should be a mapping from densities to real positive values between 0 and 1:

$$\rho \rightarrow E(\rho) \in \mathbb{R}^+ \quad (2.19)$$

where usually the maximally entangled state has $E = 1$.

Monotonicity under LOCC E should not increase under local operations and classical communications. This is the most important postulate for an entanglement measure and often cited as the *only* required postulate.

Vanishing on separable states $E(\rho) = 0$ if ρ is separable

Often one finds additional properties useful like *convexity* $E(\sum p_i \rho_i) \leq \sum p_i E(\rho_i)$ or (full) *additivity* $E(\rho \otimes \sigma) = E(\rho) + E(\sigma)$.

A function that satisfies the most important of these conditions is often called an *entanglement monotone*.

The **negativity** \mathcal{N} is such an entanglement monotone [9, 18] that used the PPT criterion to determine if a state is entangled or not. It is defined as

$$\mathcal{N} = \frac{\|\rho^{\Gamma_A}\|_1 - 1}{2} \quad (2.20)$$

where $\|A\|_1 = \text{tr} |A| = \text{tr} \sqrt{A^\dagger A}$ is the trace norm. The negativity however is not additive and a more suitable and widely used entanglement measure is the **logarithmic negativity** [8, 9, 19]

$$E_N(\rho) = \log_2 \|\rho^{\Gamma_A}\|_1. \quad (2.21)$$

The monotonicity of the logarithm implies, that E_N is an entanglement monotone as well. Furthermore, for the calculations it does not matter which subsystem is transposed.

Proposition 2.2. a) The partial transpose w.r.t. subsystem A is equal to the transposed partial transpose w.r.t. subsystem B : $\rho^{\Gamma_A} = (\rho^{\Gamma_B})^T$. b) The trace norms of partially transposed density operators w.r.t. any subsystem are equal: $\|\rho^{\Gamma_A}\|_1 = \|\rho^{\Gamma_B}\|_1$.

Proof. a) A general density matrix ρ can be expressed as

$$\rho = \sum_{i,j,k,l} \rho_{ij,kl} |i\rangle\langle j|_A \otimes |k\rangle\langle l|_B$$

The partial transpose with respect to subsystem B is then defined as

$$\rho^{\Gamma_B} \equiv \sum_{i,j,k,l} \rho_{ij,kl} |i\rangle\langle j|_A \otimes (|k\rangle\langle l|_B)^T = \sum_{i,j,k,l} c_{ij,kl} |i\rangle\langle j|_A \otimes |l\rangle\langle k|_B$$

The complete transpose of this is

$$(\rho^{\Gamma_B})^T = \sum_{i,j,k,l} \rho_{ij,kl} (|i\rangle\langle j|_A)^T \otimes (|l\rangle\langle k|_B)^T = \sum_{i,j,k,l} c_{ij,kl} |j\rangle\langle i|_A \otimes |k\rangle\langle l|_B \equiv \rho^{\Gamma_A}$$

b) Clear by a) and by using lemma 2.1 and the fact that the eigenvalues of a square matrix A and A^T are equal. \square

The logarithmic negativity is very easy to calculate compared to other entanglement measures. It is enough to compute the square root of the eigenvalues of $(\rho^\Gamma)^\dagger \rho^\Gamma$ or the absolute sum of the eigenvalues of ρ^Γ . For practical and numeric calculations it is often more easy and stable to take a single eigenvalue than the need to compute the sum of multiple. For all numerical calculations in this thesis, I therefore opt for an alternative way to compute the logarithmic negativity.

Lemma 2.1. *The trace norm $\|A\|_1 \equiv \text{tr} \sqrt{A^\dagger A}$ of a hermitian matrix A is equal to the sum of the absolute eigenvalues of A .*

Proof. This can be immediately seen by the spectral decomposition $\lambda(A) = \{\lambda_1, \dots\}$:

$$\text{tr} \sqrt{A^\dagger A} = \text{tr} \sqrt{A^2} = \text{tr} \left\{ U \sqrt{\text{diag}(\lambda_1, \dots)^2} U^\dagger \right\} = \sum_i \sqrt{\lambda_i^2} = \sum_i |\lambda_i|.$$

\square

Proposition 2.3. *The negativity eq. (2.20) is given as the absolute sum of all negative eigenvalues of ρ^Γ :*

$$\mathcal{N}(\rho) \equiv \frac{\|\rho^\Gamma\|_1 - 1}{2} = \left| \sum_{\lambda_i < 0} \lambda_i \right|. \quad (2.22)$$

Proof. The proof is in parts given by Vidal and Werner [18]. It is known that the density matrix is hermitian: $\rho = \rho^\dagger$. Using lemma 2.1, the trace norm of the density matrix is given as $\|\rho\|_1 = \sum \lambda_i = \text{tr} \rho = 1$. The partial transpose ρ^Γ obviously also satisfies $\text{tr} \rho^\Gamma = 1$ but might have negative eigenvalues. Since ρ^Γ is still hermitian, the trace norm is given by

$$\|\rho^\Gamma\|_1 = \sum_i |\lambda_i| = \sum_{\lambda_i \geq 0} \lambda_i + \sum_{\lambda_i < 0} |\lambda_i| = \sum_i \lambda_i + 2 \sum_{\lambda_i < 0} |\lambda_i| = 1 + 2 \sum_{\lambda_i < 0} |\lambda_i|,$$

where in the last step $\sum \lambda_i = \text{tr} \rho^\Gamma = 1$ was used. \square

Remark. The PPT criterion states, that if ρ^Γ has negative eigenvalues, the state ρ is entangled. The negativity uses this criterion for a quantification of entanglement. This proposition makes sense of the name *negativity*.

Calculating the logarithmic negativity of the evolved state eq. (2.13), it is possible to quantify how the entanglement behaves in time. A straight forward computation following the calculation methods established above yields (for detailed calculations see appendix A.2)

$$E_N(|\psi(t)\rangle\langle\psi(t)|) = \log_2(1 + |\sin \Delta\phi|). \quad (2.23)$$

It is interesting to see, that the maximum entanglement $E_N = 1$ is reached for $\Delta\phi = 2\pi k \pm \pi/2$, $k \in \mathbb{Z}$ and no entanglement ($E_N = 0$) is measurable for $\Delta\phi = k\pi$. This result aligns with the previous observations by demanding that the evolved state eq. (2.13) is separable. The complete entanglement dynamics are shown in fig. 2.2. The time

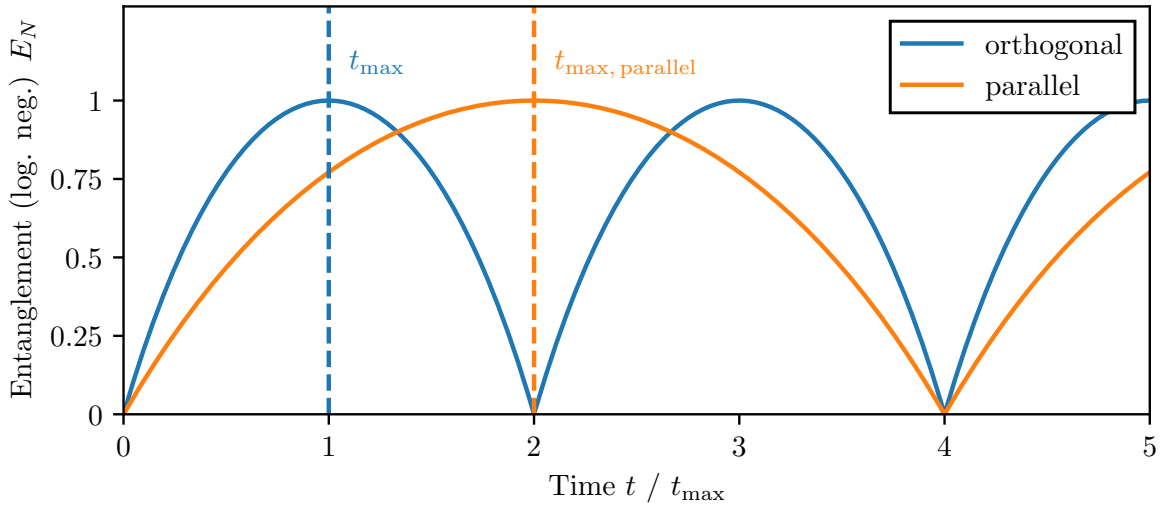


Figure 2.2: Entanglement dynamics quantified by the logarithmic negativity for two different orientations of the spatial superpositions. The parallel orientation was considered in this chapter (see eq. (2.23)), the “orthogonal” one in Ref. [10]. The time of maximum entanglement t_{\max} for the orthogonal configuration is reached after $t_{\max} = 4\pi\hbar L^3/(GM_A M_B \Delta x^2) \simeq 129$ ms.

$t_{\max, \text{parallel}}$ at which the entanglement is maximal (for the first time) can be calculated by using the definition of $\Delta\phi$ from eq. (2.15) as

$$t_{\max, \text{parallel}} = \frac{8\pi L^3 \hbar}{GM_A M_B (\Delta x)^2}. \quad (2.24)$$

In fig. 2.2 the entanglement dynamics for a different orientation considered in Ref. [10] is also shown. There, the superpositions are aligned in the same line as the direct connection between the masses (“orthogonal” to the parallel configuration before), maximizing the differences in distances between them and thus creating entanglement faster. This

expected behavior can be well seen in fig. 2.2: The time t_{\max} until the maximum entanglement is reached, is precisely by a factor of 2 faster than in the here considered parallel configuration [10]. For a practical experiment, this suggests that using the orthogonal orientation could be beneficial and would require shorter coherence times for the superpositions. To give an estimate, consider two identical silica spheres with a density of $\rho = 2648 \text{ kg/m}^3$ with a radius of $R = 10^{-5} \text{ m}$, a separation of $2L = 4R$ and a superposition size $\Delta x = 100 \text{ nm}$ (which is realistic considering theoretical sizes of up to micrometers [6]), the maximum entanglement is reached after about $t_{\max} \approx 258 \text{ ms}$ which is a quite long and challenging experimentally considering that usual in the order of nano-seconds [20].

2.3 Issues with the idealized experimental procedure

For the practical realization of an experiment on measuring gravitationally induced entanglement of masses, other forms of direct or indirect interaction between the particles must be suppressed such that the measured entanglement ultimately arises only due to their gravitational interaction. In particular, the short-range **Casimir interactions** [15] discussed in chapter 3 have to be shielded as they exert a much greater attraction force on the particles at small separations than gravity. It is still a hot topic of discussions whether Casimir interactions can even entangle macroscopic bodies at all, as it is not even clear if it is a conservative force in the first place - although most researchers believe it is [21, 22]. To estimate the minimal particle-particle separation $2L$ requiring that the gravitational interaction V_{Gravity} is stronger than the Casimir interactions V_{Casimir} by a factor $\chi > 1$, the following inequality can be stated:

$$\chi |V_{\text{Casimir}}| \leq |V_{\text{Gravity}}| \quad (2.25)$$

$$\chi \times \frac{23\hbar c}{4\pi(2L)^7} \left(\frac{\varepsilon_r - 1}{\varepsilon_r + 2} \right)^2 R^6 \leq \frac{GM^2}{2L}. \quad (2.26)$$

Using $M = 4/3\pi R^3 \rho_{\text{Silica}}$, the minimum separation distance is independent of the size of the particle and is given by

$$L \geq \sqrt[6]{\chi} \times \left(\frac{207}{4096} \frac{\hbar c}{\pi^3 G \rho_{\text{Silica}}^2} \right)^{1/6} \approx 69 \mu\text{m} \times \sqrt[6]{\chi}. \quad (2.27)$$

For the same particle as used before, the time for a single measurement, i.e. the coherence time $t_{\max} \approx 30 \text{ s} \times \sqrt{\chi}$ is very large. The field of levitated particles is promising for these experiments as it offers an isolated, noise-reduced environment while still allowing for exceptional force sensitivity as well as precise quantum control and thus long coherence times [23, 24]. Nevertheless would it be beneficial to reduce the separation distance between the particles for shorter measurement time. For this, usually a conducting **Faraday shield** between the particles is proposed [25]. Such a shield would simultaneously suppress all other forms of electromagnetic interactions such as Coulomb forced, if the particles are happened to be charged.

This thesis is focused around the problems which arise in the generation of entanglement in the presence of the Faraday shield. Generally a lot of measurements are required to reconstruct the evolved state and small variations in the initial placement of the particles can ultimately destroy the entanglement in the final averaged measurement. This effect is discussed in chapter 4. Thermal vibrations of the shield are then considered in chapter 5.

3 Casimir effect

Casimir forces can be viewed in a very similar way to the *van der Waals forces*. In fact, both phenomena describe just two different sides of the same coin. They define the so-called ***dispersion forces*** between neutral atoms or bodies. The quantum theory of van der Waals forces between two neutral atoms was developed by London in 1930 who found the attractive potential $\propto 1/r^6$ for small separations [26]. Casimir and Polder showed in 1948, that for separations larger than the resonance wavelength of the atoms, retardation effects need to be taken into account and the potential decays by a power law of $1/r^7$ [16]. Additionally, they calculated the interaction with an atom or molecule and a perfectly conducting plate, showing that macroscopic objects could experience these ***Casimir-Polder interactions*** as well. It becomes evident, that a full description of dispersion forces cannot be given by classical electrodynamics alone. Additional considerations regarding relativistic effects and quantum electrodynamics have to be made [27–29]. Casimir, following a suggestion by Bohr [30], found a simple derivation using the zero-point energy of the vacuum to calculate the attraction between two conducting plates. In quantum electrodynamics each point in the electromagnetic field can be described by an quantized harmonic oscillator with ground state energy $E_0 = \hbar\omega/2$. The total *zero-point energy* of the ground state (the vacuum) of the field is therefore given by summing over the energies E_0 for each possible mode n

$$E_{\text{vacuum}} = \frac{\hbar}{2} \sum_n \omega_n. \quad (3.1)$$

These sums are clearly divergent since there are infinitely many possible excitations. Electrostatic boundary conditions require the field to be zero at the surface of conductors restricting the possible modes between two parallel plates. Precisely the finite difference between the infinite vacuum energy with and without the macroscopic plates give rise to the ***Casimir forces***. Often, this divergence is simply dropped, motivated by the fact that energy is usually only defined up to a constant [27]. Casimir was able to use regularization techniques to deal with the infinite quantities and arrived at his famous formula [15]

$$E_{\text{Casimir}} = -\frac{\hbar c \pi^2}{720 L^3} A \quad (3.2)$$

for the attractive Casimir-potential between two plates with surface area A and separation L . The attractive force $F = -\nabla E$ between the plates can now be simply expressed as

$$F_{\text{Casimir}} = -\frac{\hbar c \pi^2}{240 L^4} A, \quad (3.3)$$

3 Casimir effect

where $c = 2.9979 \times 10^8$ m/s is the speed of light. It is remarkable, that such a simple relation arises out of the infinities of the vacuum. To this day, these Casimir forces are a major topic of modern scientific research. They are generally very difficult to calculate for geometries other than two infinitely large plates or for real materials with dielectric properties. For simple geometries, even the sign of the force is not always intuitively clear: As an example, the Casimir force for an ideal conducting spherical shell leads to an expansion of the sphere [28, 31]. Between other simple and important objects like the sphere-plane or sphere-sphere geometry, no universally valid closed formula for any separation L/R between the bodies exists. This is discussed in more detail in section 3.2.

Almost ten years after the discovery of Casimir and Polder, Lifshitz was the first to find an expression for the Casimir force between two dielectric plates with arbitrary relative permittivity $\varepsilon_{r,1(2)}$ for separations larger than the resonant wavelength⁵ [33]. The expression he found facilitates the general complexity of the Casimir interactions and is only expressible as a complicated integral [33]

$$F/A = -\frac{\hbar c}{32\pi^2 L^4} \int_0^\infty dx \int_1^\infty dp \frac{x^3}{p^2} \left\{ \left[\frac{(s_1 + p)(s_2 + p)}{(s_1 - p)(s_2 - p)} e^x - 1 \right]^{-1} + \left[\frac{(s_1 + \varepsilon_{r,1}p)(s_2 + \varepsilon_{r,2}p)}{(s_1 - \varepsilon_{r,1}p)(s_2 - \varepsilon_{r,2}p)} e^x - 1 \right]^{-1} \right\} \quad (3.4)$$

with

$$s_{1(2)} = \sqrt{\varepsilon_{r,1(2)} - 1 + p^2}.$$

In the limit of two perfectly conducting plates ($\varepsilon_{r,1} = \varepsilon_{r,2} \rightarrow \infty$), the integral can be solved analytically resulting in the same expression already obtained by Casimir

$$F_{\text{cond.}}/A = -\frac{\hbar c}{16\pi^2 L^4} \int_0^\infty dx \int_1^\infty dp \frac{x^3}{p^2(e^x - 1)} = -\frac{\hbar c \pi^2}{240 L^4}. \quad (3.5)$$

Lifshitz determined the Casimir force between a conducting metal plate and a dielectric plate (denoted DM) as well as the force between two dielectric plates with the same dielectric constant ε_r (DD) as

$$F_{\text{DM}} = -\frac{\hbar c \pi^2}{240 L^4} \frac{\varepsilon_r - 1}{\varepsilon_r + 1} \varphi(\varepsilon_r) \quad (3.6)$$

$$F_{\text{DD}} = -\frac{\hbar c \pi^2}{240 L^4} \left(\frac{\varepsilon_r - 1}{\varepsilon_r + 1} \right)^2 \varphi(\varepsilon_r) \quad (3.7)$$

where $\varphi(\varepsilon_r)$ is a numerical function obtained by solving eq. (3.4), which approaches 1 for a perfect conductor [33]. The function was numerically calculated and the result is shown in fig. 3.1. For a dielectric and metal plate, φ approaches the finite value

⁵The “resonance wavelength” for a macroscopic body in this case can be understood as e.g. the plasma frequency in the Drude model [32]. Different models for light-matter interaction result in slightly different resonant wavelength. The Lifshitz formula however holds true for the cases of separations in the micro-meter regime for all practical materials [25].

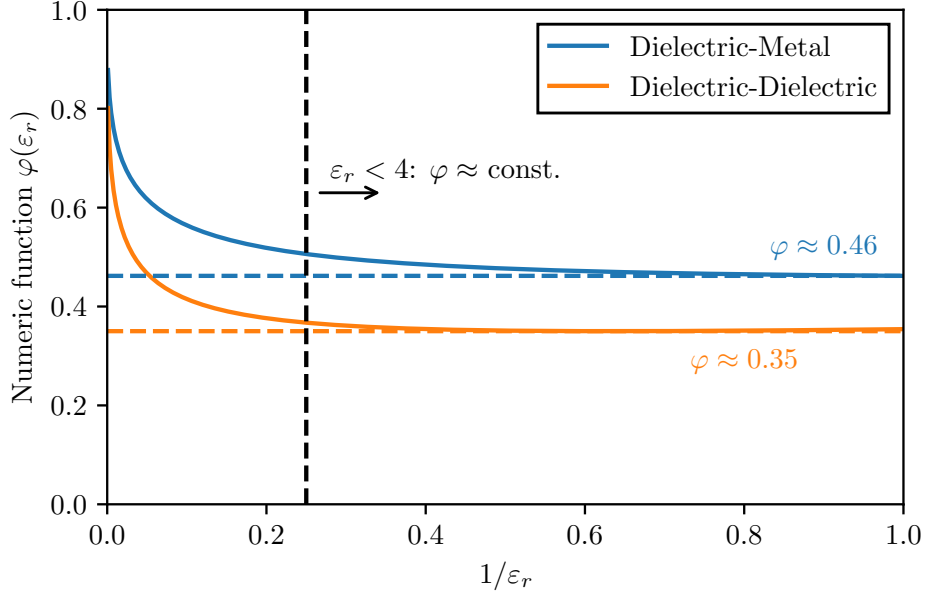


Figure 3.1: Numeric calculations of the function $\varphi(\varepsilon)$ used in the Lifshitz formula eq. (3.6) and (3.7). The function was calculated for a dielectric and a metal plates (**blue**) and two dielectric plates (**orange**). The function approaches unity for $\varepsilon_r \rightarrow \infty$ and a finite value for $\varepsilon_r \rightarrow 1$.

$\varphi(\varepsilon_r \rightarrow 1) \approx 0.46$ for small dielectric constants. This limit is practically already reached at $\varepsilon_r \approx 4$ and φ stays approximately constant for smaller ε_r .

3.1 Proximity force approximation

The Casimir-Polder force cannot be computed easily for arbitrary shapes. There even exists no analytic expression for the simple (and for this thesis relevant) plate-sphere geometry for all separations L/R . Fortunately, approximation methods exist and in particular the **proximity-force-approximation (PFA)** can be calculated very easily [34–36]. The PFA is only valid for small separations ($L/R \approx 1$) between the considered smooth bodies, where R is the size of the bodies i.e. the radius of the sphere for the sphere-plate geometry. The idea of this approximation is to divide the surfaces of the two bodies into infinitesimal small parallel plates with area dA and summing over the forces dF (or the Casimir energy dE) between them (see fig. 3.2):

$$E_{\text{PFA}} = \iint_A dA \frac{E_{\text{plate-plate}}}{A} \quad (3.8)$$

where for the Casimir energy per unit area $E_{\text{plate-plate}}/A$ either eq. (3.2) or alternatively any of the Lifshitz equations eq. (3.7) or eq. (3.6) can be used. For the following

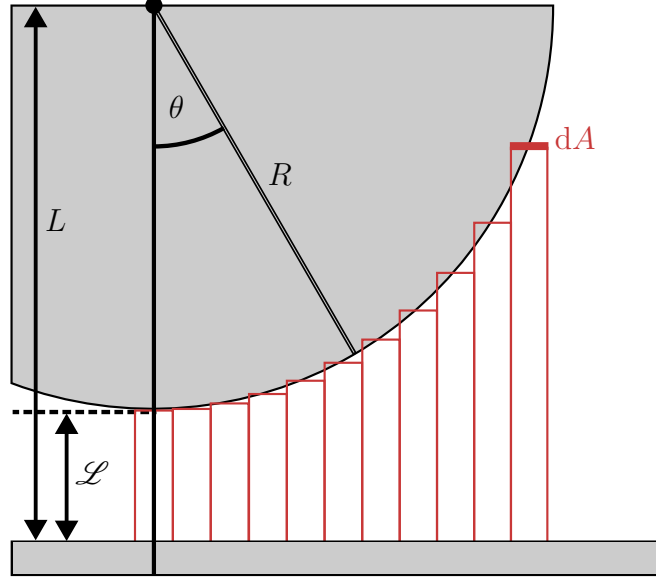


Figure 3.2: In the proximity force approximation the sphere is divided into infinitesimal plane areas dA which all exert a force dF according to eq. (3.3). All the contributions are added up together.

calculations, it is important to distinguish between the distance between the plates center and the spheres center L (like used before) and the edge-to-edge distance $\mathcal{L} = L - R$.

The problem with this approximation is, that it is ambiguous what surface the area element dA represents. For the plate-sphere geometry, dA can be either chosen either tangential to the sphere or parallel to the plate (or in theory any other fictitious surface somewhere in between) [36]. In the limit of the validity of the PFA $\mathcal{L} \ll R$ both methods usually yield the same result. For the following calculations, dA was chosen parallel to the plate and the area can be parameterized with $r \in [0, R]$ and $\varphi \in [0, 2\pi]$ resulting in a distance z between the infinitesimal area elements $L(r) = \mathcal{L} + R - \sqrt{R^2 - r^2}$ ⁶. The PFA eq. (3.8) yields for a dielectric sphere against a perfectly conducting plate

$$E_{\text{plate-sphere}} = -\frac{\hbar c \pi^2}{720} \left(\frac{\varepsilon_r - 1}{\varepsilon_r + 1} \right) \varphi(\varepsilon_r) \int_0^R dr \int_0^{2\pi} r d\varphi \frac{1}{L(r)^3} \quad (3.9)$$

$$= -\frac{\hbar c \pi^3}{360} \left(\frac{\varepsilon_r - 1}{\varepsilon_r + 1} \right) \varphi(\varepsilon_r) \frac{R^2}{2\mathcal{L}^2(R + \mathcal{L})} \quad (3.10)$$

$$\approx -\frac{\hbar c \pi^3}{720} \left(\frac{\varepsilon_r - 1}{\varepsilon_r + 1} \right) \varphi(\varepsilon_r) \frac{R}{\mathcal{L}^2} \quad (3.11)$$

⁶Taking dA tangential to the sphere, it can be parameterized with $\theta \in [0, \pi/2]$ and $\varphi \in [0, 2\pi]$ resulting in $z(\theta) = \mathcal{L} + R - R \cos \theta$. The PFA eq. (3.8) yields with $dA = R^2 \sin \theta d\theta d\varphi$ the result $\propto \frac{\pi R^2 (R + 2\mathcal{L})}{\mathcal{L}^2 (R + \mathcal{L})^2}$ which in the limit of $\mathcal{L} \ll R$ results in the same expression as eq. (3.11).

3.2 Casimir forces between a conducting plate and a dielectric sphere

An empirical derivation for a power law of the Casimir energy between a sphere and a conducting plate can be given directly using the energy between two atoms with static polarizability α_i given by Casimir and Polder [16]. They derived an expression for the Casimir-Polder potential of ⁷

$$E = -\frac{23\hbar c\alpha_1\alpha_2}{4\pi L^7}. \quad (3.12)$$

The polarizability of a sphere with radius R is derived in appendix A.3 and is given for an dielectric with ε_r as

$$\alpha_{\text{sphere}} \propto \left(\frac{\varepsilon_r - 1}{\varepsilon_r + 2} \right) R^3. \quad (3.13)$$

If one atom is now replaced by a conducting sphere ($\varepsilon_r \rightarrow \infty$) of radius $\sim L$ (much larger than the atom) with a polarizability of L^3 , it get obvious that between this big sphere and the atom, the energy is given by a power law of $1/L^4$. It is therefore natural to assume, that for a macroscopic sphere and a macroscopic plate, the Casimir energy behaves similar to a $1/L^4$ law - at least for $L \gg R$ in the **large separation limit (LSL)**. The exact calculation for this problem is very hard. In fact, no analytic solution is known. It is possible to write down an integral expression using a macroscopic approach [32]:

$$F = -\frac{\hbar c}{4\pi L^4} \int_0^\infty d\omega \alpha(\omega) [3 \sin 2\omega L - 6L\omega \cos 2\omega L - 6L^2\omega^2 \sin 2\omega L + 4L^3\omega^3 \cos 2\omega L]. \quad (3.14)$$

The expression depends on the polarizability, which is generally not constant for a dielectric. Especially for small separations between the sphere and the plate, this dependence and the non-constant polarizability make this integral nearly unsolvable. For large separations, much larger than the absorption wavelength of the dielectric or much larger than the wavelength corresponding to the plasma frequency in the Drude-Model, the polarizability can be assumed to be static [25, 32]. In this simplifying case, the integral can be solved using an exponential convergence factor and results in

$$F = -\frac{6\hbar c}{4\pi L^5} \alpha \quad (3.15)$$

and thus

$$E = -\frac{3}{8} \frac{\hbar c}{\pi L^4} \left(\frac{\varepsilon_r - 1}{\varepsilon_r + 2} \right) R^3. \quad (3.16)$$

For the large separations, the Casimir interaction between a sphere and a plate indeed behaves like expected compared with the motivation of the $1/L^4$ -law above in this section.

⁷For two macroscopic spheres, the casimir potential looks very similar to eq. (3.12). The polarizability of a sphere is given by eq. (3.13). Using this result, the Casimir energy between two identical dielectric spheres in the large separation limit is given as $-\frac{23\hbar c}{4\pi L^7} \left(\frac{\varepsilon_r - 1}{\varepsilon_r + 2} \right)^2 R^6$ [37].

A second method to calculate the Casimir energy for arbitrary compact objects and a conducting wall was developed in Ref. [37]. For the sphere-plate geometry, this results in the large separation limit (LSL) in a infinite series, where the first-order term ($\propto 1/L^4$) is precisely given by eq. (3.16) [35, 38]. The first 8 terms of this series are shown in fig. 3.3 as well as a few specific numerical points for higher terms. It becomes evident, that the

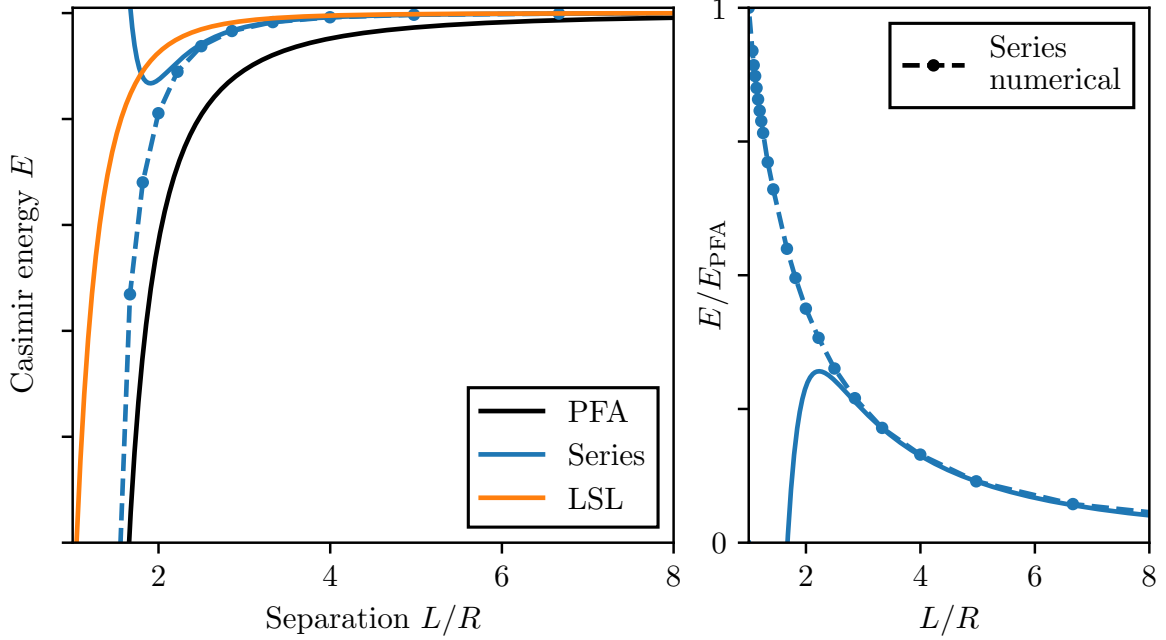


Figure 3.3: Behavior of different approximations of the casimir interaction between a conducting sphere and a perfectly conducting plate. Additionally, a comparison between the PFA and an exact numerical series expansion from Ref. [35] is shown.

series expansion converges to the LSL eq. (3.16) for large separations and to the PFA eq. (3.11) for small separations. Quantitatively the numerics show, that $E/E_{\text{PFA}} \leq 1$ and thus the PFA predicts a stronger Casimir energy for all separations.

Theorem 3.1. *The PFA model for the Casimir energy between a conducting sphere and a conducting plate is an upper bound for the actual Casimir potential for any separation L/R .*

Proof. The proof is given in the following two steps: First it is shown that **(a)** $|E_{\text{PFA}}| > |E_{\text{LSL}}|$ for arbitrary dielectric spheres, then it is shown that **(b)** $|E_{\text{PFA, cond.}}| \geq |E_{\text{PFA, diel.}}|$. Using the numerical series expansion in fig. 3.3 it is clear that this argumentation holds for all separations L/R .

(a) Directly comparing the PFA eq. (3.11) and the LSL eq. (3.16) shows

$$|E_{\text{PFA}}| > |E_{\text{LSL}}| \quad (3.17)$$

$$\frac{\hbar c \pi^3}{720} \left(\frac{\varepsilon_r - 1}{\varepsilon_r + 1} \right) \varphi(\varepsilon_r) \frac{R}{\mathcal{L}^2} > \frac{3\hbar c}{8\pi L^4} \left(\frac{\varepsilon_r - 1}{\varepsilon_r + 2} \right) R^3 \quad (3.18)$$

$$\frac{8\pi^4}{3 \cdot 720} \frac{\varepsilon_r + 2}{\varepsilon_r + 1} \varphi(\varepsilon_r) > \frac{(L - R)^2 R^2}{L^4} = \left(\frac{R}{L} \right)^2 - 2 \left(\frac{R}{L} \right)^3 + \left(\frac{R}{L} \right)^4 \quad (3.19)$$

However, comparing the maximum of the RHS at (considering $R/L \leq 1$) $1/16$ (for $R/L = 1/2$) and the minimum of the LHS, this inequality holds. The terms $(\varepsilon_r + 2)/(\varepsilon_r + 1) > 1$ and $\varphi(\varepsilon_r) \geq 0.46$ are bound. Thus the minimum of the LHS is bounded above $\approx 0.166 > 1/16$.

(b) For $\varepsilon_r \in [1, \infty)$, both $\varphi(\varepsilon) < 1$ and $(\varepsilon_r + 2)/(\varepsilon_r - 1) < 1$ are bounded, resulting trivially in $|E_{\text{PFA, cond.}}| \geq |E_{\text{PFA, diel.}}|$. \square

Remark. For later calculations, only the difference in the Casimir energy for slightly different separations L and thus effectively the gradient $\nabla E_{\text{Casimir}}$ is required. The same arguments as above can be made to see that the gradient of the PFA is an upper bound for all separations as well.

During the rest of this thesis, therefore the proximity force approximation is used as a worst-case estimation. If appropriate, both Casimir models - the PFA and the LSL - are compared.

3.3 Imperfect plate and spheres

In reality, the plate and/or the spheres are not perfectly flat and the surfaces are strewn with imperfections. This leads to small and local changes in the sphere-plate separation and thus to a marginally altered Casimir energy. Due to symmetry it is enough to only consider a imperfect plate and a perfectly smooth sphere as the Casimir interactions in the proximity force approximation (PFA) solely depend on the separation \mathcal{L} . To quantify and estimate the changes in the Casimir force due to these surface irregularities, a selection of different and relevant forms of imperfections with amplitude $\Delta\mathcal{L}$ shown in fig. 3.4 have been studied with numerical methods.

- (a) A *gaussian deformation* of the plate can be used to describe a range of possible local imperfections in the size of the sphere. For a small shield ($r_s \approx R$), thermal vibrations look very similar to these deformations, as discussed in chapter 5. A displacement with positive and negative amplitude $\pm\Delta\mathcal{L}$ in the form of a gaussian bell curve is used.
- (b) For the description of large and thus linearizable imperfections (e.g. like thermal excitations on a large shield $r_s \ll R$), a *linear deflection* is used. This deflection

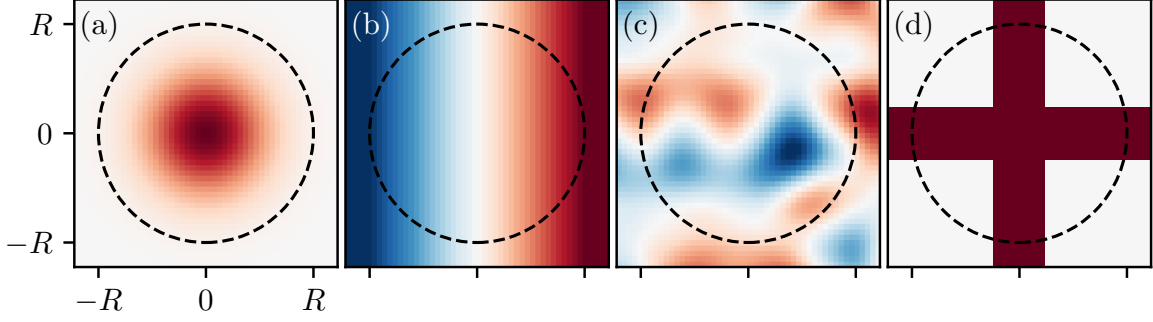


Figure 3.4: A selection of imperfect plates. (a) A simple gaussian deformation in the same size as the sphere. (b) Linearly inclining plate or a tilted flat plate. (c) Uneven and noisy but uniformly random surface realized using *Perlin noise* [39]. (d) A cross-shape in the center of the plate.

can be also understood as a tilted plate in front of the sphere where one side is much closer to the sphere than the other. For small tilting angles these variations in the Casimir potential cancel out in first order and one expects no significant change in the total attraction force.

- (c) Similarly neglectable should therefore be random noisy but uniformly distributed deformations which are here qualitatively given by the *Perlin noise* function [39]. This type of noise is commonly used in computer science and produces a uniform smooth pseudo-random noise that is often utilized to imitate surface roughness [39]. Equidistant grid-points are defined, each of which is assigned with a pseudo-random gradient. The noise function follows this gradient in the vicinity of a grid-point and the interpolation between points generates smooth transitions. Due to the uniformness, no large deviations from an ideal flat plate is expected.
- (d) A structure on the shield, like e.g. a *centered cross* might improve stability and rigidity of the shield. Thermal vibrations could be reduced by such a design but the effect and amplification of the Casimir interaction has to be investigated.

The resulting Casimir potentials between a macroscopic sphere and the imperfect surfaces were numerically calculated in the PFA and are shown in fig. 3.5. As logically expected, all variations are upper bounded by moving the ideal flat plate closer (or farther) to the sphere by a distance $\Delta\mathcal{L}$. For the gaussian distribution, the overestimation is not particularly large. An evenly tilted plate as well as a uniformly noisy plate do not change the Casimir interactions noticeably even at small separations. If the plate and sphere are far apart ($\mathcal{L} \gg R$), all local imperfections are neglectable, as their relative effect decreases and becomes less noticeable. However, the considerations made in this section are particularly important for small shields the size of the particles and close distances.

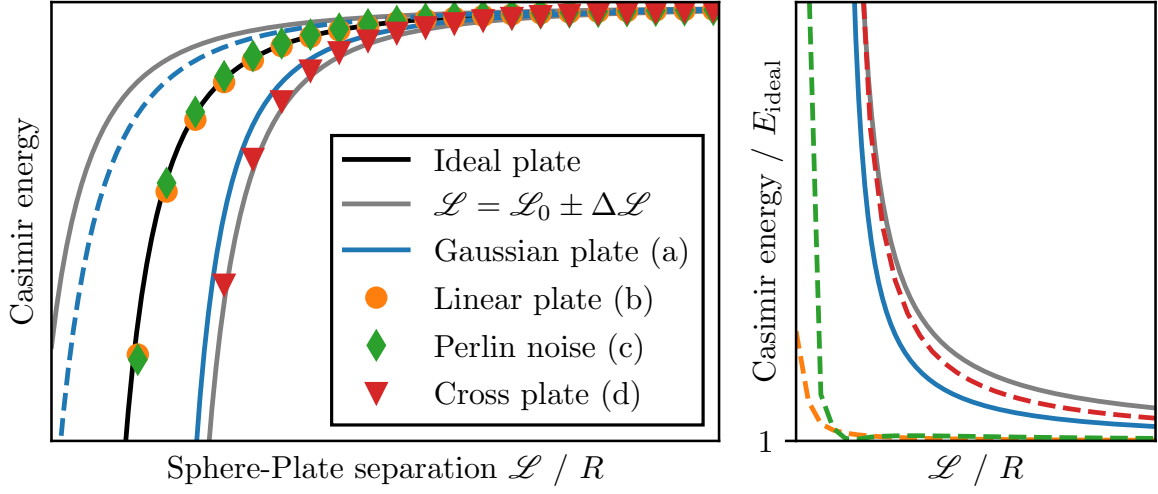


Figure 3.5: Casimir energy for the different imperfect plates shown in fig. 3.4. The dashed-blue line represents a negative gaussian displacement reducing the overall Casimir attraction. The shaded region is given by an ideal plate separated by a distance of $\mathcal{L}_0 \pm \Delta\mathcal{L}$ from the sphere where \mathcal{L}_0 is the original separation. It becomes evident that in the limit of $\mathcal{L} \rightarrow \infty$, all local imperfections are neglectable.

4 The particle in front of a static shield

The generalized setup of the system described in chapter 2 with the addition of a conducting Faraday shield is shown in fig. 4.1. As before, the particles A and B are delocalized in cat-states with superposition sizes Δx_A and Δx_B respectively. The superpositions

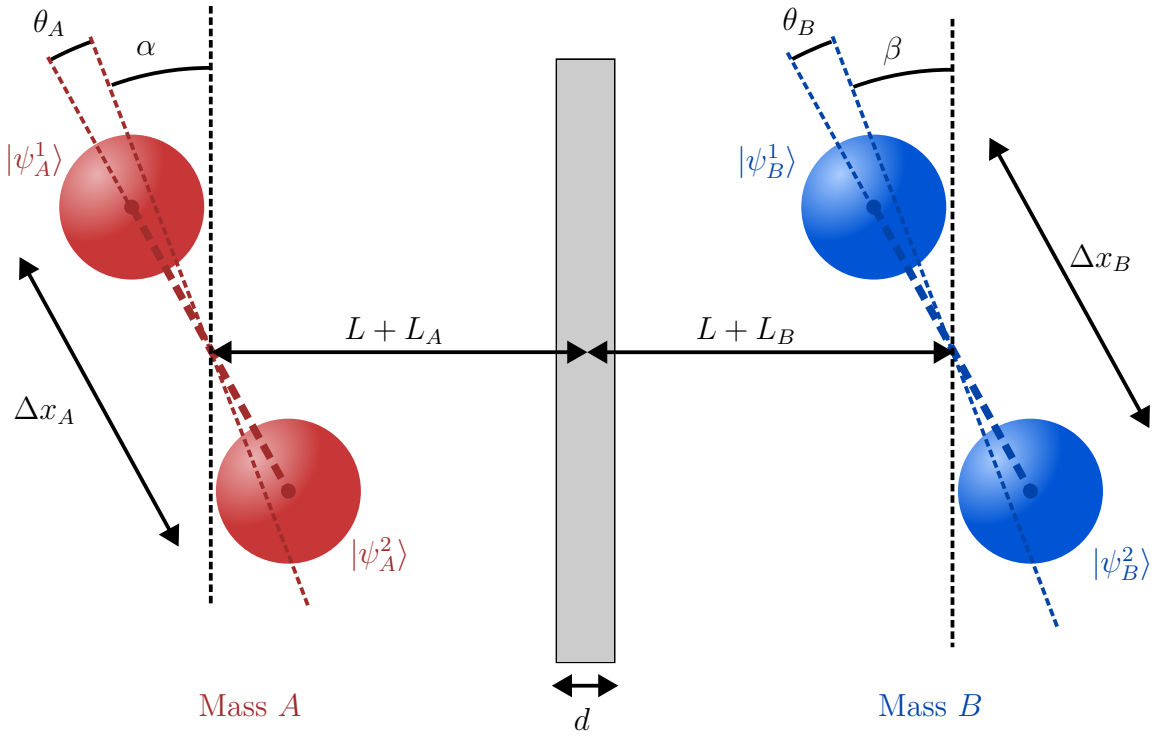


Figure 4.1: Schematic depiction of a experimental setup for the detection of gravitationally induced entanglement between two particles A and B with radius R . They are separated by a distance of $2L + L_A + L_B$ in arbitrary orientations given by the angles α and β with small variations $\theta_{A(B)}$. All variations are assumed to be normally distributed around mean zero with standard deviation $\Delta L_{A(B)}$ and $\Delta \theta_{A(B)}$. The particles are delocalized in a cat state with a separation $\Delta x_{A(B)}$ between the states $|\psi_{A(B)}^1\rangle$ and $|\psi_{A(B)}^2\rangle$. A conducting Faraday shield with thickness d is placed in the center between the particles.

are extended in arbitrary orientations $\alpha, \beta \in [0, \pi)$ a distance L away from the shield. Most notably, the configuration of $\alpha = \beta = 0$ represents the same “parallel orientation” discussed earlier in chapter 2. In the following, the case of $\alpha = \beta = \pi/2$ is referred to as the “orthogonal orientation”. If gravity is assumed to be able to mediate entanglement, the above system can generate entanglement between both particles A and B due to their mutual gravitational interaction. Placing a Faraday shield in the center between the masses should not substantially influence the gravitational entanglement generation. However, Casimir interactions between the shield and the masses are still present at small separations. It is straightforward to convince yourself that these interactions can only give rise to local phases for each cat-state, dependent only on their associated particle-shield separations $L_{A(B)}^i$ ($i = 1, 2$). Such local interactions can - assuming a static shield e.g. at zero temperature - not induce any additional entanglement between the masses.

For a complete picture, one has to consider experimental challenges and limitations in a real experiment. Measuring the states after some time to determine their entanglement requires knowledge of the states which can be obtained by e.g. full state tomography. Some proposals aim to measure a quantity that breaks the CHSH-inequality [40] (i.e. an “entanglement witness”) to proof entanglement that way [4, 6], but the generation of such a witness requires insight into the specifics of the experimental realization. In this thesis, I will focus on the most general and universally applicable case of measuring the complete density matrix of the system and checking for entanglement using a convenient entanglement measure like the “logarithmic negativity” [19] introduced in section 2.2. The density matrix of a 2 qubit system consists of 16 different entries where only 9 of them are independent⁸. For a full tomography, a lot of measurements of the system have to be made to determine the state in the required precision. During these measurements, engineering challenges of recreating the identical initial conditions, i.e. the placement of the particles in each consecutive run have to be considered. Especially stochastic variations in the initial angle $\theta_{A(B)}$ and the separation distance $L_{A(B)}$ for individual measurements are important to consider. Other fluctuations in preparing the experiment such as the measurement time were already considered previously in Ref. [41]. Even if it was somehow possible to place the particle at the *exact* same position each measurement, thermal vibrations of the shield induce small noisy variations in the shield-particle separation over a lot of runs. The masses might get entangled in each run of the measurement, however the measurements might differ slightly due to the varying initial placements of the particles resulting in a final reconstructed state that looks like a mixed state

$$\rho = \int_{-\infty}^{\infty} dX \frac{1}{\sqrt{2\pi}\Delta X} e^{-X^2/2(\Delta X)^2} |\psi_X\rangle\langle\psi_X|. \quad (4.1)$$

Here, $|\psi_X\rangle$ is the pure state of a single measurement dependent on the random variable $X = \{\theta_{A(B)}, L_{A(B)}\}$ corresponding to placement inaccuracies between multiple measure-

⁸Using the known characteristics of the density matrix like hermiticity $\rho^\dagger = \rho$ and $\text{tr } \rho = 1$, it is possible to reconstruct ρ from only 9 specific entries.

ments. These variations are assumed to be normally distributed with mean $\langle X \rangle = 0$ and standard deviation ΔX on the basis of the central limit theorem [42, p. 1195]. In some cases, as for example if the plate is not placed exactly in the center or at a tilt, the variations $\theta_{A(B)}$ and $L_{A(B)}$ are correlated as for example $L_A = -L_B$ holds. In the most general case, all placement variations are assumed to be independent and are drawn from their respective probability distribution.

Convergence for a finite number of measurements

Experimentally, it would be very interesting to know how fast the averaged density matrix $\bar{\rho}$ after a finite number of $\#$ measurements converges to the idealized asymptotic mean $\langle \rho \rangle$ given by eq. (4.5), which is calculated and analyzed in depth in the next two sections. After $\#$ measurements, the sample average is given by

$$\bar{\rho} = \frac{1}{\#} \sum_{k=1}^{\#} \rho(X_k) \quad (4.2)$$

where $\rho(X)$ depends on the random variable $X \in \{\theta_{A(B)}, L_{A(B)}\}$ and X_k is the k -th sample drawn from the normal distribution $\mathcal{N}(0, (\Delta X)^2)$ ⁹. As $\# \rightarrow \infty$, the law of large numbers and in particular the central limit theorem (CLT) ensures that $\bar{\rho} \rightarrow \langle \rho \rangle$ [42, p. 1195]. According to the CLT, the sample average $\bar{\rho}(X)$ fluctuates around $\langle \rho \rangle$ with a standard deviation given by the Berry-Esseen theorem for independent and identically distributed random variables X_k by $\sigma \sim \#^{-1/2}$ [43]. Thus, if the placements of the particles in each measurement are completely independent from each other, the rate of convergence to the ideal mean $\langle \rho \rangle$ is governed similar to the shot-noise limit by $\mathcal{O}(1/\sqrt{\#})$.

It is however very likely that measurements are mostly performed consecutively in the same trap so that the placements in successive measurements are correlated. The correlations $\text{Cov}[\rho(X_i), \rho(X_j)] = c_{|i-j|}$ between the i -th and j -th measurement should therefore decrease with increasing $|i-j|$. The variance of $\bar{\rho}$ is now dependent of these correlations in the form [42, p. 1227]

$$\text{Var}[\bar{\rho}] = \frac{1}{\#^2} \sum_{i,j=1}^{\#} \text{Cov}[\rho(X_i), \rho(X_j)] = \frac{1}{\#} \text{Var}[\rho] + \frac{2}{\#^2} \sum_{n=1}^{\#-1} (\# - n) c_n \quad (4.3)$$

where $\text{Cov}[\rho, \rho] = \text{Var}[\rho]$ was used for the variance of the mean density matrix $\langle \rho \rangle$. For correlations $c_n \sim n^{-\alpha}$ ($\alpha < 1$) the sum in eq. (4.3) scales like

$$\sum_{n=1}^{\#-1} (\# - n) n^{-\alpha} \xrightarrow{\# \rightarrow \infty} \int_1^{\#} dn (\# - n) n^{-\alpha} \sim \#^{2-\alpha} \quad (4.4)$$

which results in $\text{Var}[\bar{\rho}] \sim \#^{-\alpha}$. In the asymptotic limit the standard deviation of the sample average $\sqrt{\text{Var}[\bar{\rho}]}$ and thus the convergence rate to the mean $\langle \rho \rangle$ scales with

⁹Here it isn't strictly required that X_k are normally distributed. As long as they are i.i.d. random variables, any distribution is sufficient for the following argumentation [42, p. 1195].

$\mathcal{O}(1/\sqrt{\#}^\alpha)$. This convergence is arbitrary slow for small α (if the setup does not change a lot between individual measurements) and thus the calculations in the next sections are just a worst-case estimation of the actual experimental results. If a weaker correlation in the form of $c_n \sim e^{-\alpha n}$ is assumed, the convergence rate is again asymptotically governed by $\mathcal{O}(1/\sqrt{\#})$.

4.1 Entanglement generation

The averaged state $\langle \rho \rangle$ after multiple measurements can be calculated as

$$\langle \rho \rangle = \int_{-\infty}^{\infty} d\theta_A p(\theta_A) \int_{-\infty}^{\infty} d\theta_B p(\theta_B) \int_{-\infty}^{\infty} dL_A p(L_A) \int_{-\infty}^{\infty} dL_B p(L_B) \rho(\theta_A, \theta_B, L_A, L_B) \quad (4.5)$$

where $p(\cdot)$ is the gaussian probability distribution of the random variables $\theta_{A(B)}$ and $L_{A(B)}$ with standard deviation $\Delta\theta$ or ΔL respectively. $\rho(\theta_A, \theta_B, L_A, L_B)$ is the state of a single measurement, dependent on the initial setup parameters. The initial state ρ_0 at $t = 0$ is given similarly as before by eq. (2.7) at the beginning of chapter 2. During time evolution, additionally to the mutual gravitational interaction, Casimir forces between the particle and the Faraday shield must be taken into account. A single superposition state $|\psi_{A(B)}^{(i)}\rangle$ ($i = 1, 2$) accumulates the phase $\phi_{A(B), \text{Cas}}^{(i)}(t)$ during time evolution due to these Casimir interaction, where the phases are given by

$$\phi_{A(B), \text{Cas}}^{(i)}(t) = \frac{t}{\hbar} \begin{cases} \frac{3\hbar c}{8\pi} \left(\frac{\varepsilon_r - 1}{\varepsilon_r + 2} \right) \frac{R^3}{(L_{A(B)}^{(i)})^4} & \text{for large separations (LSL)} \\ \frac{\hbar c \pi^3}{720} \varphi(\varepsilon_r) \left(\frac{\varepsilon_r - 1}{\varepsilon_r + 1} \right) \frac{R}{(\mathcal{L}_{A(B)}^{(i)})^2} & \text{for small separations (PFA)} \end{cases} \quad (4.6)$$

Here, both analytical limits - the PFA for $L \ll R$ and the LSL for $L \gg R$ - of the Casimir force discussed in chapter 3 have been used. The tabulated function $\varphi(\varepsilon_r)$ is necessary to describe Casimir interactions between dielectric materials and reaches unity for a perfectly conducting particle [33]. The separations $L_{A(B)}^{(i)}$ and $\mathcal{L}_{A(B)}^{(i)} = L_{A(B)}^{(i)} - R$ between the particle and the shield's surface are placement dependent and in full generality given by

$$L_A^{(i)} = L + L_A - \frac{d}{2} \pm_i \frac{\Delta x_A}{2} \sin(\alpha + \theta_A) \quad (4.7)$$

$$L_B^{(i)} = L + L_B - \frac{d}{2} \mp_i \frac{\Delta x_B}{2} \sin(\beta + \theta_B) \quad (4.8)$$

where \pm_i distinct between the two cat-states of a single particle. The mutual gravitational coupling of the state $|\psi_A^{(i)}\rangle \otimes |\psi_B^{(j)}\rangle$ is given similar as in the previous calculations in chapter 2 by the accumulated phase

$$\phi_{\text{Grav}}^{(ij)}(t) = \frac{t}{\hbar} \frac{GM_A M_B}{L^{(ij)}}. \quad (4.9)$$

The separation distance $L^{(ij)}$ between the states $A^{(i)}$ and $B^{(j)}$ is given by

$$L^{(ij)} = \sqrt{\left(2L + L_A + L_B \pm \frac{\Delta x_A}{2} \sin(\alpha + \theta_A) \mp \frac{\Delta x_B}{2} \sin(\beta + \theta_B)\right)^2 + \left(\frac{\Delta x_A}{2} \cos(\alpha + \theta_A) \pm \frac{\Delta x_B}{2} \cos(\beta + \theta_B)\right)^2}. \quad (4.10)$$

Expanding the accumulated gravitational- and Casimir phases to first order in $\Delta x_{A(B)} \ll L$, $\theta_{A(B)} \ll 1$ and $L_{A(B)} \ll 1$ (which is possible since all these variations are very small, as seen later), the averaging of the evolved state $\langle \rho \rangle$ in eq. (4.5) can be performed analytically (for an exemplary calculation see appendix B.1). It turns out that with $\Delta \theta_A = \Delta \theta_B \equiv \Delta \theta$ and $\Delta L_A = \Delta L_B \equiv \Delta L$ all off-diagonal elements of the averaged state $\langle \rho \rangle$ (the so-called **coherences**) are given in the form

$$\langle \rho_{kl} \rangle = \frac{1}{4} e^{i\Delta\phi_{kl}(t)} \exp\left\{-\frac{(\xi_{kl})^2}{2}(\Delta\theta)^2 t^2\right\} \exp\left\{-\frac{(\zeta_{kl})^2}{2}(\Delta L)^2 t^2\right\} \quad (4.11)$$

where $\Delta\phi$, ξ and ζ are substitutes for rather lengthy expressions that depend on the particle-shield separation L , the orientation of the cat-state α, β , the masses of the particles $M_{A(B)}$ and their superposition size $\Delta x_{A(B)}$. It becomes evident that for large times $t \rightarrow \infty$ or for large variations in the placement $\Delta\theta, \Delta L \rightarrow \infty$ these off-diagonal elements tend to zero which leads to a continuous and monotonic loss of purity, resulting in the maximally mixed state $\text{tr} \rho^2 = 1/4$ - which obviously is not entangled. For large variations in the initial placement of the particles, one therefore expects the loss of coherence and thus of entanglement.

The resulting logarithmic negativity of the averaged state $E_N(\langle \rho \rangle)$ was computed numerically for different values of $\Delta\theta$ and ΔL and is shown in fig. 4.2. For this figure, the parallel orientation $\alpha = \beta = 0$ was used at times relative to the time of maximum entanglement t_{max} from eq. (2.24). In this special case, the entanglement is given by

$$E_N(\langle \rho \rangle) = \max \left\{ 0, \log_2 \left(e^{-\gamma} (\cosh \gamma + |\sin \Delta\phi|) \right) \right\} \quad (4.12)$$

where the definition of the decoherences γ can be found in appendix B.1 and $\Delta\phi$ in the parallel orientation is given by eq. (2.15). For fig. 4.2 the radius of the particles was set to $R = 1 \times 10^{-5}$ m with corresponding mass $M_A = M_B = 4/3 \pi R^3 \rho_{\text{Silica}} \approx 1.1 \times 10^{-11}$ kg. A particle-shield separation of $L = 2R$ and a superposition size of $\Delta x_A = \Delta x_B = 100$ nm were chosen. In the rest of the thesis, if not otherwise specified, these parameters are used as a default. For convenience, they are collectively displayed in table 4.1 for easy retrieval. They are chosen in the specific orders of magnitude, because they result in a feasible low experiment-time $t_{\text{max}} \approx 258$ ms and are in the region of what is soon¹⁰ possible [23, Timestamp: 51:00]. Other proposals suggest a similar parameter set generally differing only by a single magnitude (see e.g. the Tab. 1 in Ref. [44]). It is important

¹⁰“Soon” in this context means still a long time, but the experiment could be doable within this century.

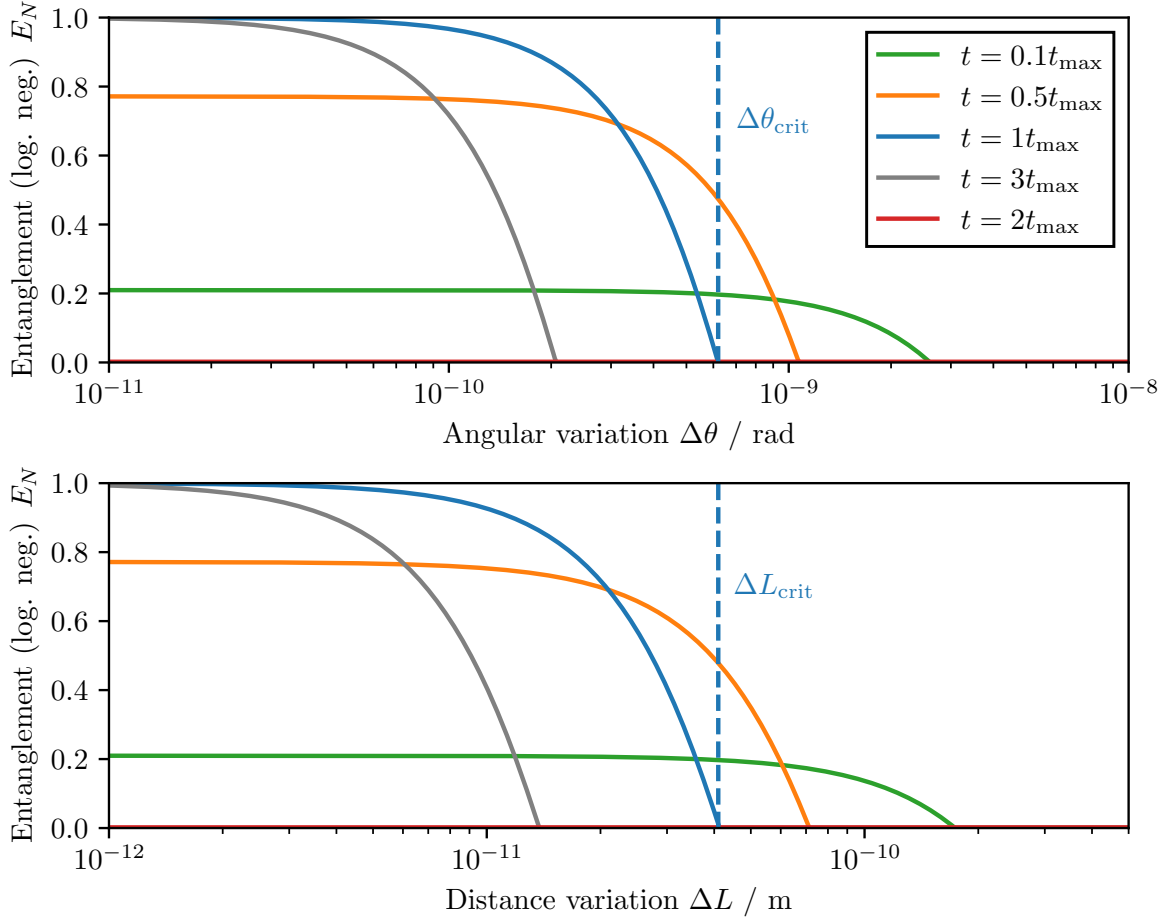


Figure 4.2: Entanglement quantified by the logarithmic negativity (eq. (2.21)) dependent on the angular variation $\Delta\theta$ and the distance variation ΔL in the parallel configuration. The entanglement is shown at different times, where $t_{\text{max}} \approx 258$ ms is the time of maximal entanglement from eq. (2.24). At the critical point $\Delta\theta_{\text{crit}}$ or ΔL_{crit} all entanglement is lost.

however to stress out, that all these parameters are orders of magnitude away of from what is experimentally reachable today. The largest mass that was studied in matter-wave interferometry is in the order of 4×10^{-23} kg [13] with an superposition size of $\Delta x \gtrsim 500$ nm. For solid state mechanical systems quantum control and in particular groundstate cooling up to masses in the order of 10^{-13} kg [20], 10^{-11} kg [45] and 10^{-8} kg [46] with very short coherence times $\lesssim 1 \mu\text{s}$ have been demonstrated. On the contrary, the smallest mass with a measurable gravitational coupling is around 92 mg [14]. The field of levitated particles combines the best of both worlds with exceptional quantum control with high force sensitivity as well as long coherence times up to the order of seconds [23] and thus many proposals aim to measure quantum entanglement due to gravity between trapped particles [3].

The entanglement of the system shown in fig. 4.2 behaves as expected: It is virtually unaffected for small placement variations and at some critical point $\Delta\theta_{\text{crit}}$ or ΔL_{crit} , the entanglement is completely lost. This point can - in special cases (by e.g. only considering either angular or distance variations) - be computed analytically using eq. (4.12) and is given by

$$\theta_{\text{crit}} = \frac{\log(1 + \sqrt{2})}{\gamma} \propto \gamma^{-1}. \quad (4.13)$$

For the used parameters and in the parallel orientation, this threshold is around $\Delta\theta_{\text{crit}} \approx 6 \times 10^{-10}$ rad and $\Delta L_{\text{crit}} \approx 1.4 \times 10^{-10}$ m, which seems quite challenging experimentally. However, it seems like that for smaller times $t < t_{\text{max}}$ larger variations can be tolerated for the cost of having less total entanglement. This is again expected. For smaller times, the gravitational force did not have enough time to fully entangle the two particles, but also the decoherences (dependent on $\gamma \propto t^2$; see eq. (4.11) and appendix B.1) did not have enough time to built up. It is therefore logical, that if one does not require to measure a fully entangled state and less entanglement $E_N < 1$ is also sufficient, it may be beneficial to measure at a time $t < t_{\text{max}}$. In theory, it would be enough to measure *any* entanglement $E_N > 0$ but one has to make sure that other mechanisms such as direct or indirect entanglement trough other couplings or noise sources have smaller entanglement rates (for a discussion see chapter 5). Measuring at a earlier point in time does not only reduce the duration of a single experimental measurement, but also increases the stability against displacement variations. This optimal time of measuring for a certain required amount of entanglement is shown in fig. 4.3. The chart additionally lets one read out the corresponding maximal angular variation after a set time. Conversely, if one is experimentally limited by a certain maximum angular variation, one can read off the corresponding best measurement time and the maximum amount of entanglement that can be obtained. It also can be seen that at times $2kt_{\text{max}}$, $k \in \mathbb{N}$ there is no entanglement. This corresponds to the findings from the ideal scenario in chapter 2.

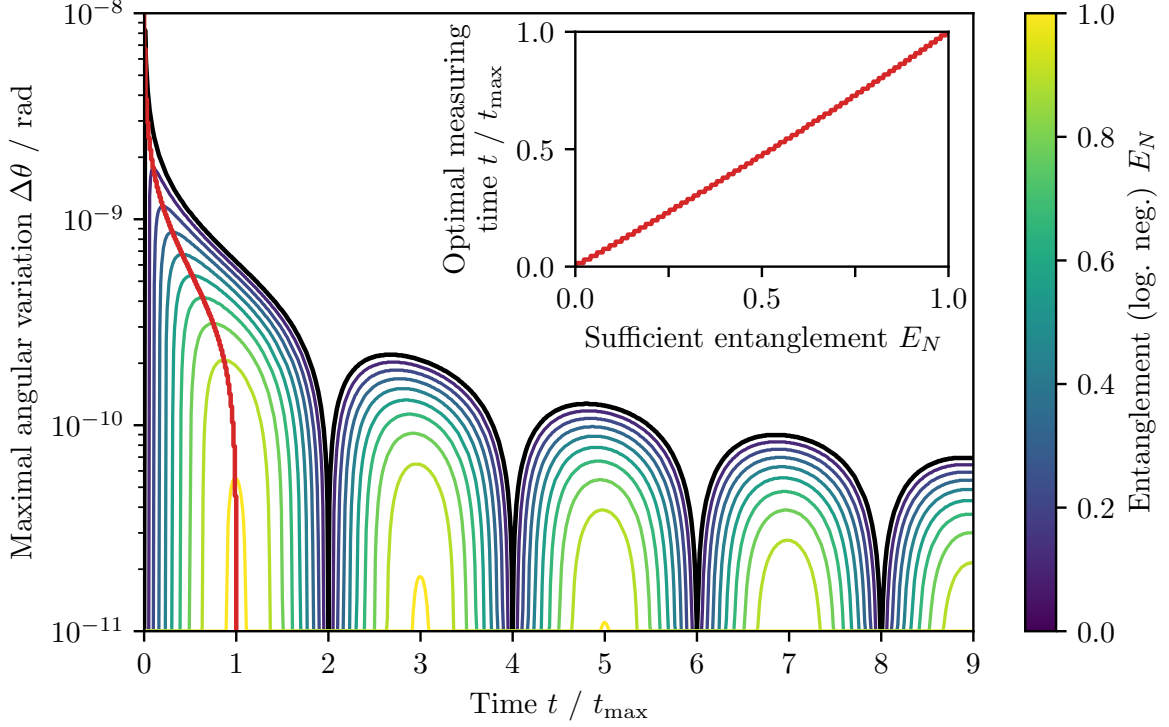


Figure 4.3: Maximal angular variation for given times after which a specific amount of entanglement E_N is still measurable. The setup parameters are taken from table 4.1. The outer most black line corresponds to the time dependence of $\Delta\theta_{\text{crit}}$. A fully entangled state with $E_N = 1$ is only measurable at precisely $t = t_{\text{max}}$ with a maximally possible angular variation of around 10^{-11} rad. The red curve on the top left shows the optimal measuring time for a specific amount of entanglement. Correspondingly the red curve in the main figure shows the corresponding maximal angular variation for which this goal is reachable. At times $2kt_{\text{max}}$, $k \in \mathbb{N}$ no entanglement can be measured.

4.2 The optimal setup

With the general framework in hand, the next logical question to ask is, whether the stability against placement-variations can be improved. The rule of thumb for these optimizations is the following: Increase the gravitational interaction by either heavier and larger particles or by reducing the separation distance L without substantial sacrifices of experimental realization. As an example, the stability increases intuitively by increasing the separation distance L . However, this does also increase the time t_{\max} until the maximum amount of entanglement can be measured which would increase the total time $\sim \#t_{\max}$ of the experiment with $\#$ individual measurements. It is not immediately obvious, how the stability and the maximum possible variations $\Delta\theta_{\text{crit}}$ and ΔL_{crit} behave for the change in parameters. In the following section, precisely the changing of this stability is discussed for altering the orientation α, β , the particle-shield separation L , the mass $M_A = M_B \equiv M$ and the superposition size $\Delta x_A = \Delta x_B \equiv \Delta x$.

Table 4.1: Default parameters for the setup in fig. 4.1 used in the next sections. Maximum entanglement is reached after a time $t_{\max} = 259$ mn for these parameters. They were chosen in accordance with multiple proposals [23, 44]. Both particles are assumed to be identical with the same mass and superposition size. The thickness d and radius r_s of the shield is estimated in section 5.1.

Orientation	Particle size		L	Δx	Shield size ^b	
	Radius R	Mass M ^a			d	r_s
Parallel ($\alpha = \beta = 0$)	$10 \mu\text{m}$ $= 10^{-5} \text{ m}$	$\approx 10^{-11} \text{ kg}$ $= 5 \times 10^{-4} m_p$	$2R = 20 \mu\text{m}$	100 nm	100 nm	1 cm

^a Here $m_p = \sqrt{\hbar/G} \approx 2.17 \times 10^{-8} \text{ kg}$ is the Planck mass. ^b The required size of the shield is later estimated in section 5.1.

4.2.1 Orientation

One of the arguably easiest parameter to change experimentally is the orientation of the superpositions, which is quantified by α and β in fig. 4.1. As already seen in fig. 2.2, the entanglement dynamics are dependent on the orientation. In the parallel orientation, the states take twice as long as in the orthogonal orientation to become maximally entangled. In general, it is advantageous to aim for the highest entanglement rate and thus the smallest $t_{\max}(\alpha, \beta)$, as this requires a shorter coherence time and thus reduces the total time of the experiment. The previous results from chapter 2 can be further generalized for an arbitrary orientation α, β . The logarithmic negativity is given by

$$E_N = \log_2 (1 + |\sin \Delta\phi|) \quad (4.14)$$

where $\Delta\phi$ is now dependent on the orientation and is defined as (for $\Delta x \ll L$)

$$\Delta\phi = \frac{GM_A M_B t \Delta x_A \Delta x_B}{8\hbar L^3} \left(\sin \alpha \sin \beta - \frac{1}{2} \cos \alpha \cos \beta \right). \quad (4.15)$$

The maximum entanglement $E_N = 1$ is reached for $\Delta\phi = \pm\pi/2$ and thus after a time

$$t_{\max}(\alpha, \beta) = \frac{4\pi\hbar L^3}{GM_A M_B \Delta x_A \Delta x_B} \left| \sin \alpha \sin \beta - \frac{1}{2} \cos \alpha \cos \beta \right|^{-1}. \quad (4.16)$$

For some specific symmetric cases, the resulting times for different orientations are shown in fig. 4.4. The global minima of $t_{\max}(\alpha, \beta)$ is attained in the orthogonal orientation. This

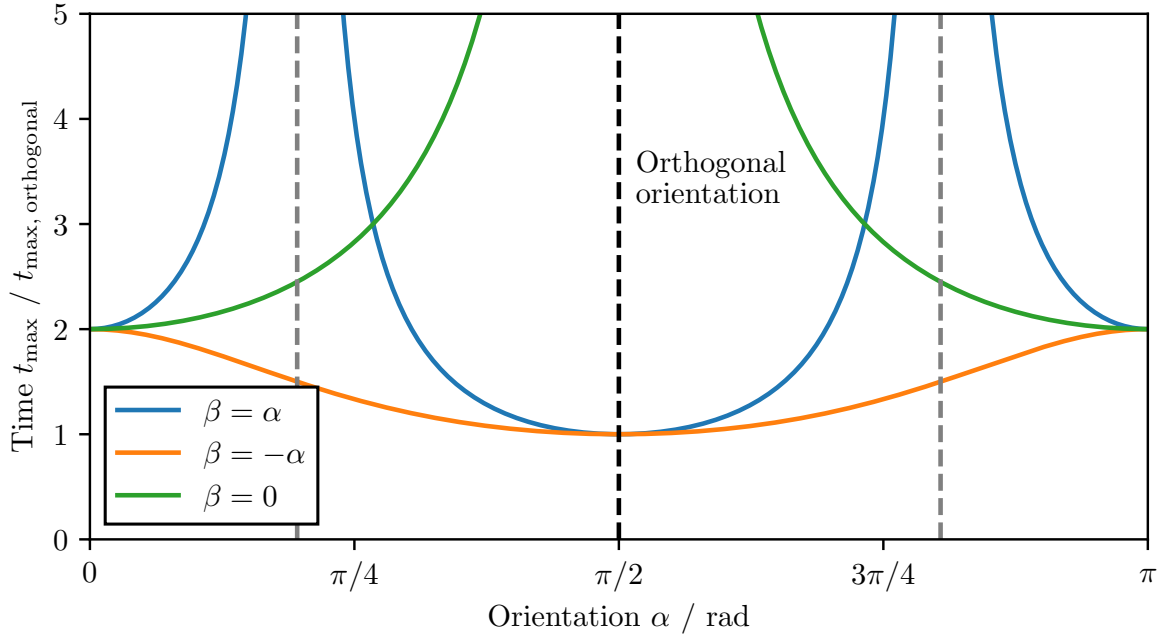


Figure 4.4: Time t_{\max} after which maximum entanglement ($E_N = 1$) is reached for different orientations. Only the most interesting and highly symmetric cases $\alpha = \pm\beta$ and $\beta = 0$ are shown. The singularity $t_{\max} \rightarrow \infty$ for $\beta = 0$ and $\alpha = \pi/2$ is expected. The two other singularities at $\alpha = \beta = 2 \arctan(\sqrt{3} \pm \sqrt{2})$ are explainable by the “harmonic mean” in fig. 4.5.

is not surprising considering that this orientation maximizes the *differences in separation distances* between all superposition states. Much more interesting and surprising are the unanticipated singularities in fig. 4.4 which appear for

$$\sin \alpha \sin \beta = \frac{1}{2} \cos \alpha \cos \beta. \quad (4.17)$$

For $\beta = 0$ the singularity at $\alpha = \pi/2$ is not surprising. In this configuration, the distances $|\psi_A^1\rangle \leftrightarrow |\psi_B^{1,2}\rangle$ and $|\psi_A^2\rangle \leftrightarrow |\psi_B^{1,2}\rangle$ are identical and thus these states accumulate the same

phases, resulting in a factorable global phase. In the case of $\alpha = \beta$, the two singularities are precisely given in the orientation

$$\alpha = \beta = 2 \arctan(\sqrt{3} \pm \sqrt{2}) \approx 90^\circ \pm 54.74^\circ. \quad (4.18)$$

There does not exist a straight-forward geometric interpretation why no entanglement is generated exactly in this configuration, however all 4 separation distances between the states form the “harmonic mean” visualized in fig. 4.5. Here, in the limit $\Delta x \ll L$

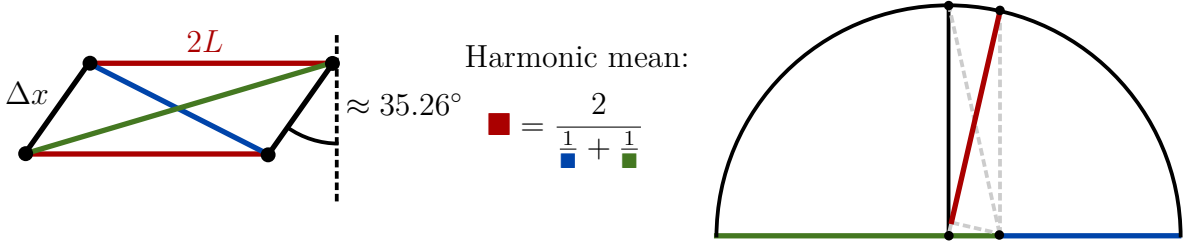


Figure 4.5: **left:** The system in the orientation $\alpha = \beta = 2 \arctan(\sqrt{3} - \sqrt{2})$. For $\Delta x \ll L$, all separation distances exactly form the *harmonic mean*. Here, the phases due to the mutual gravitational interaction precisely cancel out resulting in no entanglement. **right:** Geometric visualization of the harmonic mean.

every local phase precisely cancels out resulting in a loss of entanglement. To avoid all these singularities, it is advisable to always take $\alpha = -\beta$, where all orientations result in roughly similar entanglement times t_{\max} , at most only differing by a factor of 2.

It should come as no surprise that the different orientations exhibit different stabilities. Logically, one would expect the orthogonal configuration to be much more sensitive to angular variations than the parallel one. In contrary, the parallel configuration should be much more stable against variations in the distance, since no phase difference (“dephasing”) is induced between the two superposition states $|\psi_{A(B)}^1\rangle$ and $|\psi_{A(B)}^2\rangle$ of the particle A (B).

The effect of different orientations on the stability against angular variations and the behavior of the critical angular variation $\Delta\theta_{\text{crit}}$ is shown in fig. 4.6. As expected, the orthogonal configuration is the most stable against these kind of variations. This is, because the dephasing ultimately depends on the distance between the state and the shield $L \pm \Delta x/2 \cos \theta \approx L \pm \Delta x/2(1 - \theta^2/2)$, which is a only second order effect of the angular variations θ . This explains the apparent “infinitely” good stability in the figure, as the analytical solution only uses first order approximations in θ . Exact numerical results however cap the stability at $\Delta\theta_{\text{crit,orthogonal}} \approx 7.3 \times 10^{-5}$ rad.

Respectively, the stability against distance variations ΔL_{crit} for different orientations is shown in fig. 4.7. Again aligning with expectations, the parallel configuration is (in theory) exhibits an infinite stability. One however could argue, that a for this to hold, the uncertainties in the angular placement have to be zero. As could be seen in fig. 4.6,

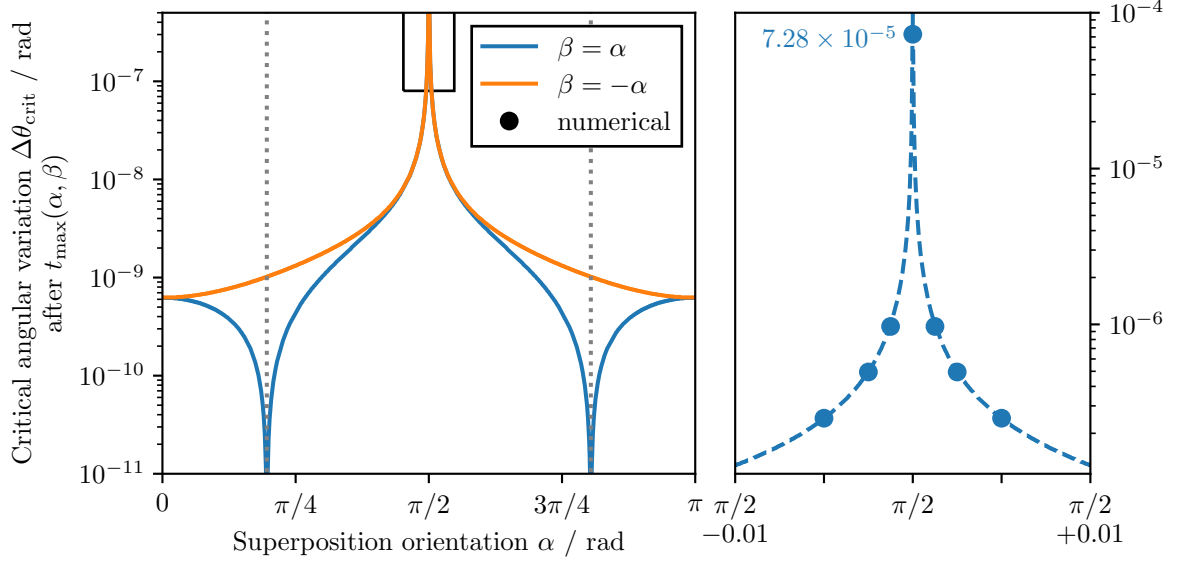


Figure 4.6: Critical angular variation $\Delta\theta_{\text{crit}}$ for different orientations after the time $t_{\text{max}}(\alpha, \beta)$ for which maximum entanglement is reached. The **orthogonal orientation** magnified on the right is very stable against angular variations and only numerical methods show a finite stability value. The singularities in the left figure for $\alpha = \beta$ arise from the fact, that these orientations need infinite time to entangle as already seen in fig. 4.4.

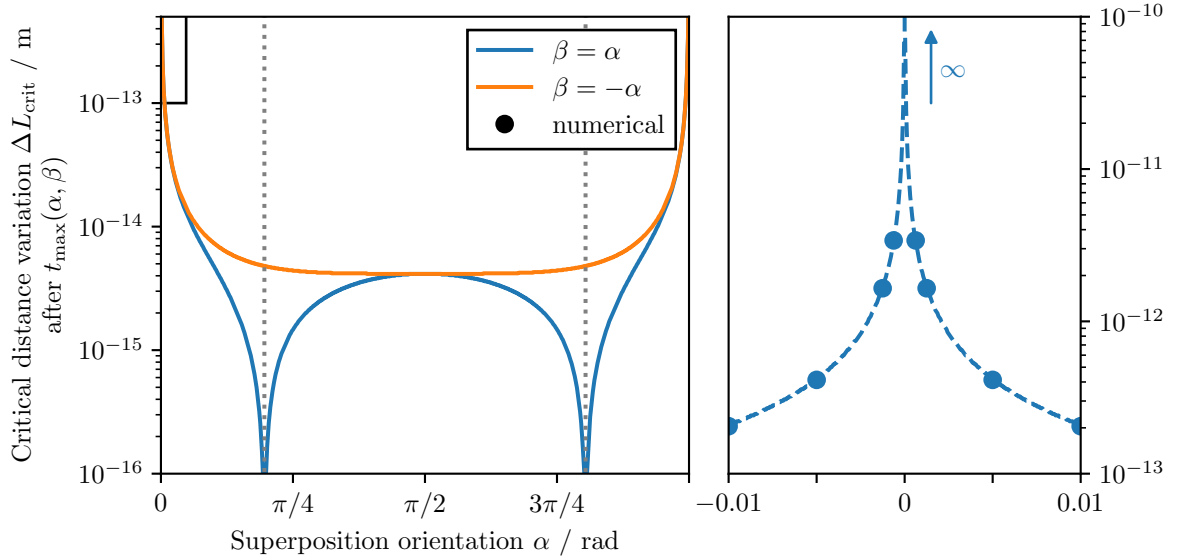


Figure 4.7: Critical distance variation ΔL_{crit} for different orientations after a time $t_{\text{max}}(\alpha, \beta)$. Here, the **parallel orientation** (magnified on the left) is infinitely stable against placement variations.

these variations are at most around $\sim 5 \times 10^{-5}$ rad and thus a realistic upper bound for the minimum required distance variations is given by $\Delta L_{\text{crit,parallel}} = \Delta L_{\text{crit}}(\alpha \approx 5 \times 10^{-5} \text{ rad}) \simeq 4 \times 10^{-11} \text{ m}$. It is important to keep in mind, that these stability values can be improved substantially by e.g. increasing the separation distance L , the particle size R or the superposition size Δx .

Considering these results, the parallel orientation seems to be the only realistic experimental option, even if it requires slightly larger coherence times t_{max} . Keeping particle-shield separation variations below 0.01 pm - even smaller than size of a single atom - is practically impossible, especially under the additional consideration of the thermal vibrations of the shield and the particles, which are in the same order of magnitude as seen later in chapter 5. With this data on hand, it is possible to generate the stability diagram in fig. 4.8, showing the optimal orientation in which the most entanglement can be measured. For most combinations of ΔL and $\Delta \theta$, entanglement is exclusively given in either the parallel or orthogonal orientation.

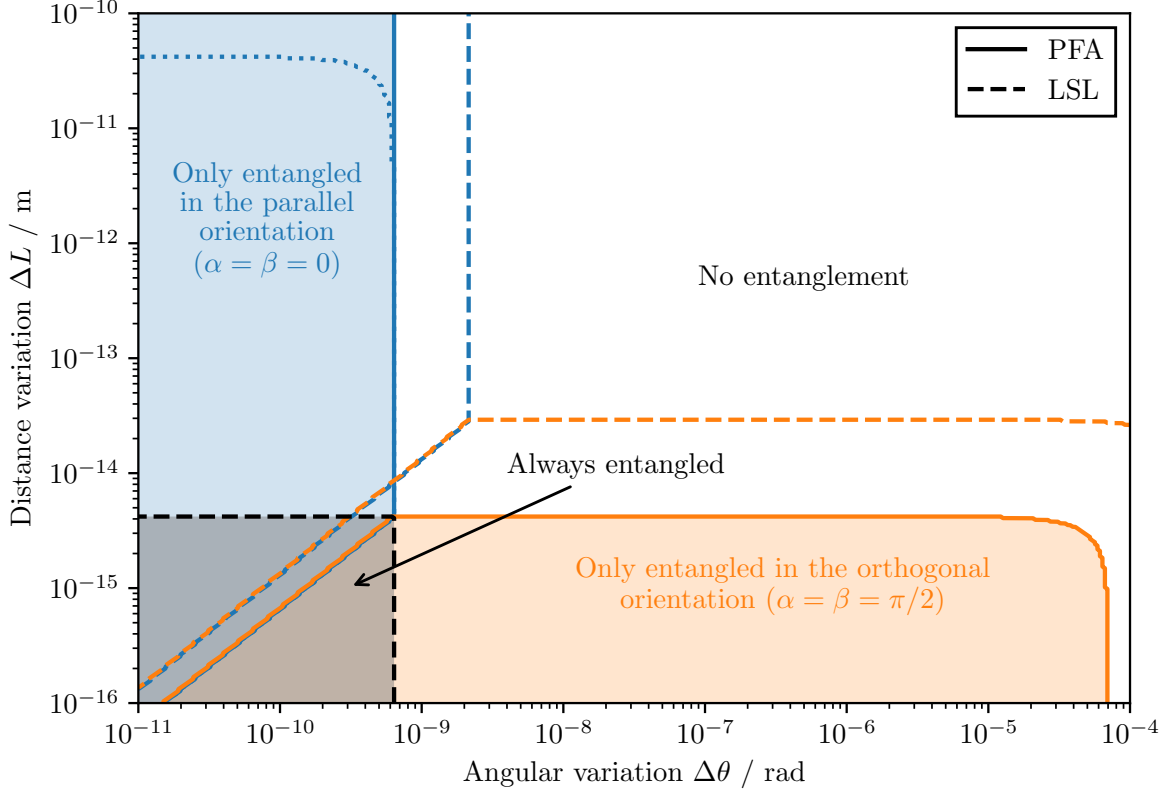


Figure 4.8: Optimal orientation for the experimental setup dependent on the variations in angle $\Delta\theta$ and distance ΔL for a initial separation distance of $L = 2R = 2 \times 10^{-5}$ m at time t_{\max} . The different predictions for the proximity-force-approximation (PFA) and the large-separation-limit (LSL) are shown. At a distance of $L = 20 \mu\text{m}$ the actual casimir interaction is somewhere in the middle between both approximations. In the region where entanglement is given regardless of the orientation (the bottom left), the orientation with *more* entanglement is still colored. The dotted line corresponds to the realistic upper bound discussed in the text.

4.2.2 Separation, mass and superposition size

It is possible to improve the required stability in placement and consequently the entanglement generation by changing the other parameters shown in fig. 4.1 besides the orientation. It is especially easy to modify the separation distance L during the experiment as one is only limited in the trap stability close to the shield discussed in section 4.3. The other parameters like the particle mass M and thus the radius R , the particle material and the superposition size Δx are considerably more difficult to change. One is limited by the experimental implementation of the spatial superpositions. Considering that up to date, the largest spatial superposition of a “macroscopic object” is in the order of $\Delta x \sim 500$ nm for masses of 4×10^{-23} kg [13], large changes in the delocalization size Δx or the particles mass might be virtually impossible. However, out of a theoretical standpoint, the effects of all these parameters and the improvements reachable in stability are interesting and considered in the following section.

Beginning with the effect of a larger particle-shield separation L , the improvements on angular stability are shown in fig. 4.9. A similar figure can be created for the stability of

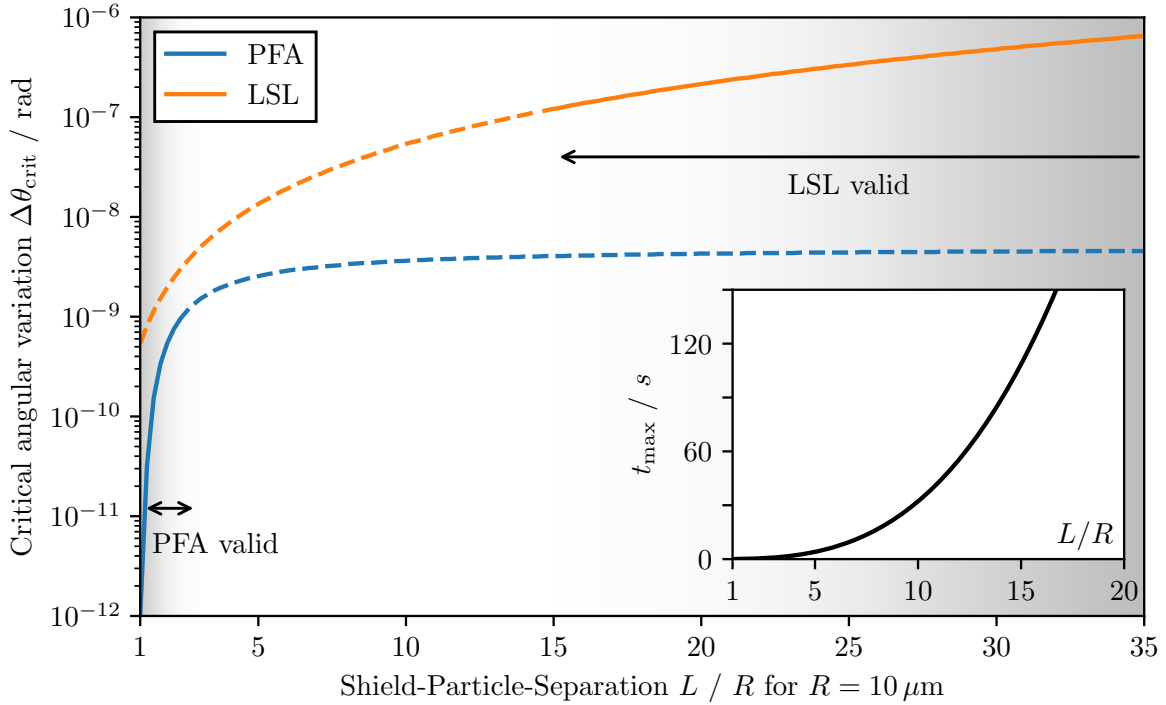


Figure 4.9: Stability against angular variations for increasing separation distances L in units of $R = 10 \mu\text{m}$ after a time $t_{\text{max}}(L)$. The dependence on the radius can be seen in fig. 4.10. Two models for the casimir-interaction are shown: The proximity-force-approximation (PFA) and the large-separation-limit (LSL). The regions outside the models validity are indicated with dashed lines. In the bottom right the time $t_{\text{max}}(L) \propto L^3$ is shown.

distance-variations ΔL , but as already discussed previously, the setup is very (infinitely) stable against small distance variations in the parallel configuration. It is intuitively clear that a larger separation improves the stability, as the relative effect of the variations $\sim \Delta x \sin \theta \ll L$ decreases and the Casimir potential tends towards zero. However, a larger separation also increases the time $t_{\max} \propto L^3$ until the maximum entanglement is built up. The combination of both effects leads to the result shown in fig. 4.9. Due to the strong distance dependence on the casimir model, both limits for either small separations $L \sim R$ (PFA) or large separations $L \gg R$ (LSL) have been compared. The “real” casimir potential lies somewhere between the two models. In general, it can be said, that a large separation is desirable, as long as the required coherence times are still reachable. Looking at the final averaged density matrix $\langle \rho \rangle$, it is possible to deduce the dependence of $\Delta\theta_{\text{crit}}$ on the separation L . The off-diagonal decoherence terms calculated in appendix B.1 and given by eq. (B.8) scale similar to

$$\langle \rho_{\text{off-diagonal}} \rangle \sim \exp \left\{ - \left(\frac{2\xi_{\text{Casimir}}\Delta x}{(L - R - d/2)^3} \pm \frac{\zeta_{\text{Gravity}}\Delta x}{4L^2} \right)^2 (\Delta\theta)^2 t^2 \right\} \quad (4.19)$$

where the second term corresponding to gravitational interactions is much smaller than the first term and thus can be neglected for small L . At the point $\Delta\theta_{\text{crit}}$ all entanglement is lost leading to $\langle \rho_{ij} \rangle \rightarrow 0$. Using the analytical results from eq. (4.13) it is possible to get the dependence of $\Delta\theta_{\text{crit}}$ on L as

$$\Delta\theta_{\text{crit}} \sim \frac{1}{t_{\max}} (L - R - d/2)^3 \sim \frac{(L - R - d/2)^3}{L^3}, \quad (4.20)$$

which aligns very nicely with the blue curve for the PFA in fig. 4.9 ($R^2 = 0.99$ as it is only a approximation). Similar arguments show that for large separations in the LSL the critical angular variation scales with $\Delta\theta_{\text{crit}} \sim L^2$.

The mass of the particles is determined by their radius R as well as their material. Most likely, the trapped and levitated particles are made of silica (SiO_2) with a density of $\rho_{\text{Silica}} = 2648 \text{ kg/m}^3$, as this material has been used widely in experiments on levitated nanoparticles [47, 48]. Due to its transparency, silica is very easy to trap in strong optical traps, but even quantum control in magnetic traps has been demonstrated with silica [48]. For this thesis, I will assume that all trapped particles are made of silica. Otherwise denser or heavier materials like e.g. stable osmium and lead isotopes would be worth considering. Trapping them in a paramagnetic trap could be theoretically possible and interesting as sufficient masses could already be reached with far fewer atoms and smaller particles, further improving coherence times and quantum control. The effect on angular stability of a larger and thus heavier particle is shown in fig. 4.10. It is important to note, that the time t_{\max} scales with M^{-2} and thus effectively with R^{-6} , making the effect of a slightly larger sphere very noticeable. One does need to find the ideal size of the sphere depending on what is possible experimentally: The mass must be large enough for gravity to have a measurable effect but simultaneously small enough for sufficient quantum control in the laboratory. Estimations suggest the usage

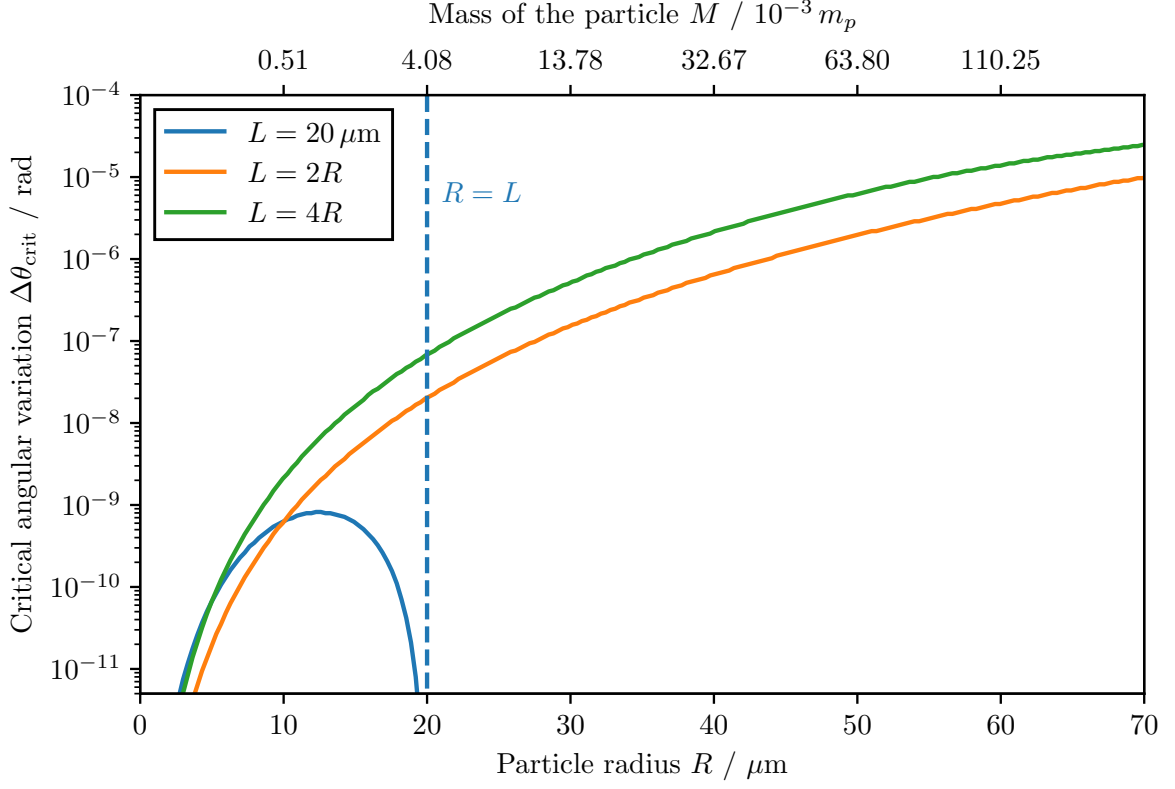


Figure 4.10: Critical angular variation $\Delta\theta_{\text{crit}}$ for different sized particles after a time $t_{\text{max}}(M)$. The mass of the corresponding particle in units of the Planck mass $m_p = \sqrt{\hbar c/G} \approx 2.176 \times 10^{-8} \text{ kg}$ is given on the top axis. For particles as large as the separation $R = L$, the surface-to-surface separation is almost zero, resulting in large casimir forces and thus no entanglement.

of masses around the order of $10^{-11} \text{ kg} \approx 10^{-3} m_p$ as being possible [23, Timestamp: 51:00]. The scaling of $\Delta\theta_{\text{crit}}$ with a changing size R of the particles can be determined similar to before. It turns out, that for a constant separation L , the critical angular variation scales with

$$\Delta\theta_{\text{crit}} \sim \frac{(L - R - d/2)^3}{\phi_{\text{Casimir}}} \frac{1}{t_{\text{max}}} \sim \frac{(L - R - d/2)^3 R^6}{R} \quad (4.21)$$

whereas for $L \propto R$, the time $t_{\text{max}} \propto L^3/R^6$ varies additionally resulting in

$$\Delta\theta_{\text{crit}} \sim (R - d/2)^3 R^2. \quad (4.22)$$

The final parameter that theoretically be freely modified, is the size of the superposition Δx . A larger superposition size would increase the entanglement generation due to gravity because the differences in the distances between all superposition states would increase. Such effects ultimately lead to a faster build-up of entanglement scaling with $t_{\text{max}} \propto (\Delta x)^{-2}$. In matter wave experiments, superposition sizes of massive objects up to $\Delta x \approx 500 \text{ nm}$ were already achieved [13]. These sizes are much smaller than the size of the particle itself at $10 \mu\text{m}$. The effect of the superposition size on stability is shown in fig. 4.11. For large superposition sizes, the time until maximal entanglement is reached, decreases drastically. In the shorter time, the dephasing due to the casimir effect between the shield and the states is less substantial, increasing the stability against variations in the placement. A larger superposition size on the other hand results in a greater effect of angular variations $\sim \Delta x \sin(\theta)$. Both of these effects result in a effective scaling of $\sim \Delta x$, which explains the linear curve¹¹.

4.3 Trapping the particle

Another consequence of shielding that requires consideration is the influence and the possible instability of the particle trap. Levitated particles are trapped and cooled in an ultra-high vacuum by either a magnetic, optical or electrical radiofrequency Paul-trap [24]. These traps differ in the trapping mechanism, but if the particle is cooled close to the ground state, all trapping potentials can be considered “harmonic” with trapping frequency $\omega_{\text{trap}} = 2\pi \times f$. The strength of the trapping potential $V \propto f^2$ differs for the different trapping types. Typical values range from $1 \text{ Hz} - 1 \text{ kHz}$ for magnetic traps [24, 48] up to $10 \text{ kHz} - 300 \text{ kHz}$ for optical traps [24]. The different types of traps also offer different advantages and disadvantages: Optical traps are relatively noisy due to the constant interaction between the particle and the light. Magnetic traps for large particles are less noisy, but only low trapping frequencies are possible [24]. For electric traps, the particle must be charged, which causes a lot of different problems, as seen in section 5.1.

¹¹Here it is shown in a double-logarithmic plot. The relation between Δx and $\Delta\theta_{\text{crit}}$ is nevertheless linear, which can be seen with similar arguments as used previously.

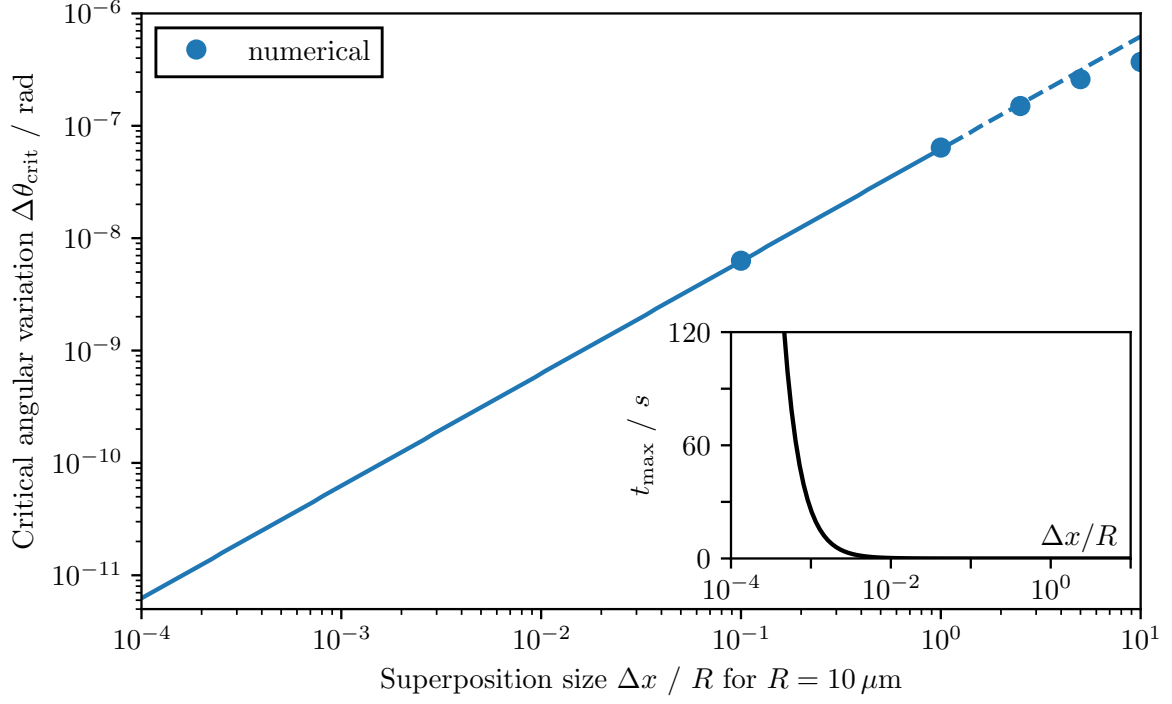


Figure 4.11: Effect of the superposition size Δx on the critical angular stability $\Delta\theta_{\text{crit}}$ after a time $t_{\text{max}}(\Delta x)$. For $\Delta x \gtrsim R$, numerical results are used. In the lower left, the time till maximum entanglement $t_{\text{max}} \propto (\Delta x)^{-2}$ is shown. For $\Delta x \ll R$, the resulting relation between Δx and $\Delta\theta_{\text{crit}}$ is linear.

Strictly speaking, to generate cat-state superpositions a non-harmonic potential like e.g. a “double well potential” is required. In the parallel orientation, the double wells are also oriented parallel to the shield resulting in a quasi-harmonic potential from the side-view as seen in fig. 4.12.

If the particle in the harmonic trapping potential is placed close to the shield, the Casimir interaction $\sim \mathcal{L}^{-2}$ can disturb the trapping and eventually even suck the particle onto the shield. The total potential $V_{\text{tot}} = V_{\text{trap}} + V_{\text{Casimir}}$ is shown in fig. 4.12 for a stable and unstable configuration. Due to the influence of the attractive Casimir force, the

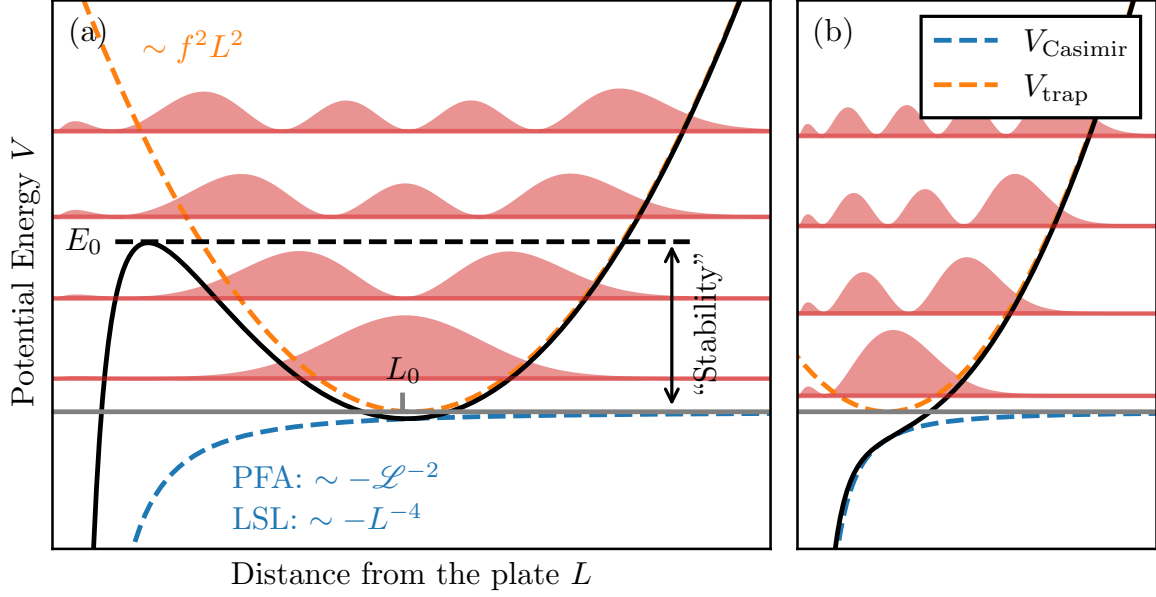


Figure 4.12: Visualization of the potential as an overlay of the harmonic trapping potential $V_{\text{trap}} = m(2\pi f)^2 L^2/2$ and the casimir potential V_{Casimir} . f is the trapping frequency and L_0 the position of the trap. In red, eigenstates of the potential are visualized offset by the eigen-energies. **(a)** Almost harmonic bounded potential which can hold the particle, if its energy is less than E_0 . **(b)** Potential with no bounded states. Here, trapping is not possible.

equilibrium position of the trap shifts slightly closer to the shield by $\Delta\xi$. This shift

$$\Delta\xi = \frac{|\nabla V_{\text{Casimir}}|}{m(2\pi f)^2} = \frac{2\hbar c\pi^3}{720} \left(\frac{\varepsilon_r - 1}{\varepsilon_r + 1} \right) \varphi(\varepsilon_r) \frac{R}{\mathcal{L}^3} \frac{1}{m(2\pi f)^2} \quad (4.23)$$

is negligibly small as it is in the order of $\Delta\xi \approx 10^{-13}$ m for $f = 1$ kHz and $L = 2R = 20 \mu\text{m}$.

To determine the stability of a trapped particle with mass $M \propto R^3$ in a trap with frequency f placed at a distance $L_0 > R$ in front of the shield, the number of bound energy-eigenstates in the potential V_{tot} is considered. From fig. 4.12 it becomes clear,

that as long as the particles thermal energy is well below E_0 , the trap is stable and the particle is bound. Here, E_0 is defined as the local maximum of the potential

$$E_0 = \max_{L \in (R, L_0)} (V_{\text{trap}} + V_{\text{Casimir}}) \quad (4.24)$$

where L_0 is the position where the particle is trapped. If there does not exist a local maximum, i.e.

$$\frac{\partial}{\partial L} (V_{\text{trap}} + V_{\text{Casimir}}) > 0 \quad (4.25)$$

for all $L \in (R, L_0)$, the resulting trap cannot be stable. These regions of no stability are shown as a white area in the stability diagram fig. 4.13. In the general case, the stability can be measured by computing the number of bound eigenstates $n(E_0)$ with energies less than E_0 and comparing them with the number of thermally excited states \bar{n} . At a temperature T on average

$$\bar{n} = \frac{1}{e^{\beta \hbar \omega} - 1} \quad (4.26)$$

states are occupied, where $\beta = 1/k_B T$ and $\omega = 2\pi f$. This is true, as long as the potential is assumed to be harmonic, which is, as seen shortly, a very good approximation. To find the number of possible bound energy-eigenstates in the potential, the **WKB-approximation** [49] is used. In this approximation, the energy of the n -th eigenstate of a smooth and appropriately slow varying potential $V(x)$ can be calculated using [49, p. 163]

$$\int_{x_1}^{x_2} dx \sqrt{2m(E - V(x))} = \left(n + \frac{1}{2}\right) \pi \hbar, \quad (4.27)$$

where $V(x_1) = V(x_2) = E$ are two turning points corresponding to energy E . Conversely, it is possible to use this approximation to numerically estimate the total number of bound states in the potential $V = V_{\text{trap}} + V_{\text{Casimir}}$ using

$$n(E_0) \approx \frac{1}{\hbar \pi} \int_{x_1}^{x_2} dx \sqrt{2m(E_0 - V(x))}, \quad (4.28)$$

which is closely given (highest deviation around 40%; averaged relative error $\sim 0.9\%$) by the harmonic approximation $n(E_0) \sim E_0/\hbar\omega$. The resulting number of bound states is shown in fig. 4.13 as well as the stability boundaries at specific temperatures where $\bar{n} = n(E_0)$. In these calculations, tunneling effects between through the potential boundary at E_0 are neglected which should not influence the results much considering the large number of bound eigenstates. It turns out, that regardless the type of the trap, a successful trapping even at room temperature should be possible as long as the particle is placed appropriately far away from the trap. The ability to trap and levitate the masses is therefore not significantly impaired by the presence of the Faraday shield.

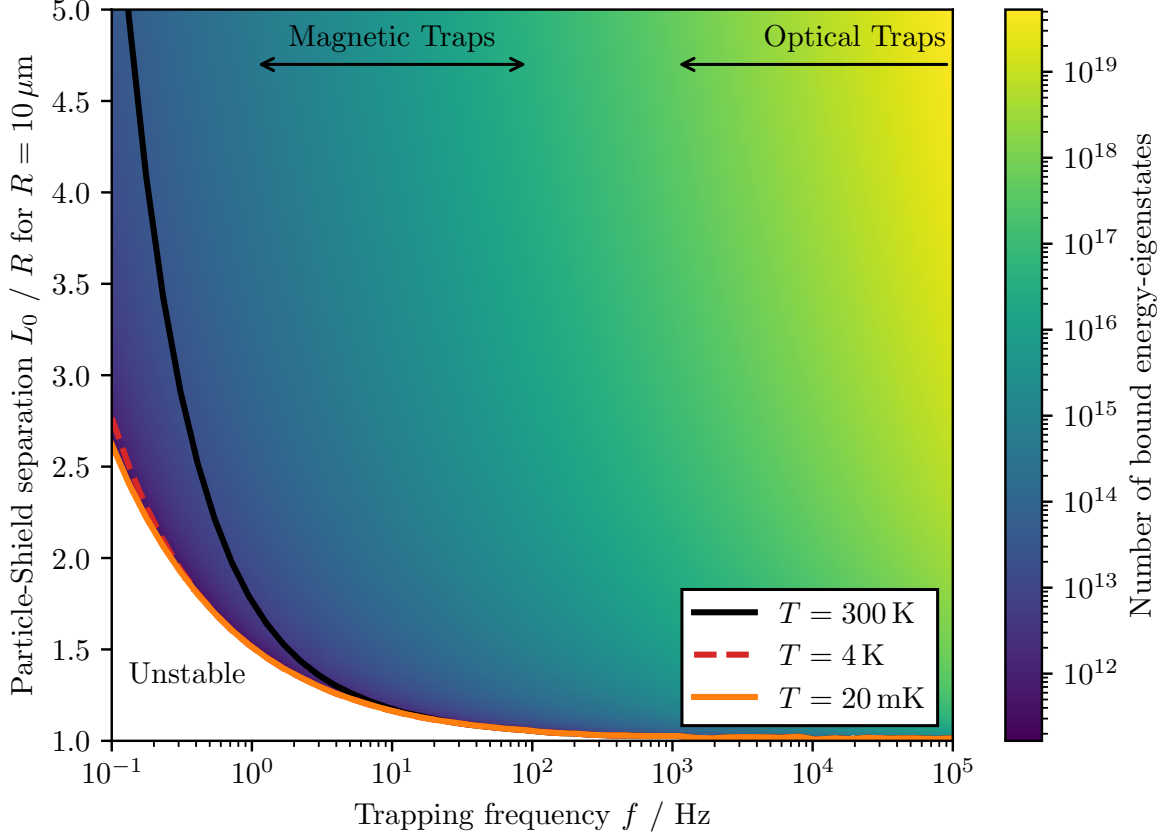


Figure 4.13: Stability diagram for different trapping frequencies $f = \omega/2\pi$ and particle-shield separations L_0 . The number of bound energy-eigenstates for each combination of f and L_0 are calculated using the WKB-approximation. The number of thermally occupied states \bar{n} at different Temperatures is overlaid. As an example, for $f = 1$ Hz, $\bar{n}(T = 300 \text{ K}) \approx 10^{13}$ states are thermally occupied. All regions below these boundaries are unstable. A increase in the radius R and thus the mass M improves the regions of stability massively.

4.4 Discussions

Looking at the preceding results, it is clear that the planned experiment represents a significant engineering challenge. The decoherence due to the Casimir interactions between the particles and the Faraday shield requires an accuracy in the placement of the particles in the order of $\Delta L \simeq 10^{-10}$ m and $\Delta\theta \simeq 10^{-9}$ rad. Achieving these accuracies appears to be very challenging and it will be necessary to adjust the originally proposed parameters in fig. 4.1. The separation distance L as well as the orientation are particularly easy to change. As discussed earlier, the parallel orientation might be the only viable option, as this position is almost infinitely stable against variations in the distance. The orthogonal orientation would require placement accuracies in the order of single atoms (see in fig. 4.7). The separation L can be freely chosen and a larger separation reduces the effect of placement variations as seen in fig. 4.9 but substantially increases the required coherence time $t_{\max} \propto L^3$. It could also be argued that at a distance of $L \geq 100 \mu\text{m} = 10R$ (compare to section 2.3), the Faraday shield would no longer be required because the Casimir forces between the particles are ~ 10 times weaker than the gravitational interactions due to their rapid decrease at large distances. However, the loss of entanglement due to angular and distance variations in placement is not solely due to Casimir forces between the particle and the shield, so that a complete removal of the shield does not fully eliminate the required placement accuracy. The slightly varying gravitational interaction alone can induce enough decoherence on its own to destroy entanglement. The critical variations for a gravitational interaction alone in the parallel configuration after t_{\max} are given by $\Delta\theta_{\text{crit, ideal}} = 1.1 \times 10^{-3}$ rad and $\Delta L_{\text{crit, ideal}} = 7 \times 10^{-4}$ m, which should not pose an engineering problem.

Changing the other parameters such as the particles size or superposition size might not be possible. Substantially changing both would increase the difficulty in groundstate cooling and quantum control unforeseeable. For all these considerations, the trapping does not play a role as this should be possible with a suitable magnetic or optical trap for almost any possible configuration of the setup parameters (compare to the results from section 4.3).

One of the objectives of this thesis is, to determine whether it is possible to bring the particles closer together through the presence of the Faraday shield in order to increase gravitational entanglement and reduce the required coherence times. To achieve this, the previous results from this chapter can be used to find the optimal parameters of the experimental setup. The goal of the optimization process can be expressed as the following:

One wants to get *as much entanglement as possible* in the *shortest time possible* with the *largest possible variations* in the placement while still considering the limitations in the particles mass as well as in the superposition size.

In full generality, it is not possible to find a local optimum for choosing the parameters. This is because (if the mass M and the superposition size Δx is fixed) the coherence time - which should be minimized - scales with $t \propto L^3$ by eq. (4.16) and the critical

angular variation - which should be as large as possible - scale with $\Delta\theta_{\text{crit}} \propto (L - R)^3/L^3$ for small separations (eq. (4.20)) or $\Delta\theta_{\text{crit}} \propto L^2$ for $L \gg R$. Both of these optimization criteria cannot be fulfilled simultaneously as long as no constraints are given. Given however a coherence time t_{target} and/or the minimum possible placement accuracy, it is possible to determine the required sphere-plate separation L as well as the amount of entanglement, one can maximally expect using the following steps:

1. Lets assume that the size of the particle R and consequently the mass $M = 4/3\pi R^3 \rho_{\text{Silica}}$ as well as the superposition size Δx are fixed. An increase in either of them would have a positive effect of the optimization goal stated above, as the time t_{max} decreases and the stability against placement variations increases simultaneously.
2. The following ratio given by eq. (4.16) in the parallel orientation and by Ref. [23]

$$\frac{M^2(\Delta x)^2}{L^3} t_{\text{max}} = \frac{8\pi\hbar}{G} = \text{const.} \quad (4.29)$$

is fixed. For orthogonal configurations, this constant would reduce by a factor of $1/2$.

3. In general it is possible to measure at a earlier time $t_{\text{target}} = \tau t_{\text{max}}$ (i.e. the coherence time) with $\tau \leq 1$, where less total entanglement has been build up but in general a grater stability against placement variations can be achieved (see fig. 4.3). Putting all assumptions together, the ratio

$$\frac{t_{\text{target}}}{\tau L^3} = \frac{8\pi\hbar}{G} \frac{1}{M^2(\Delta x)^2} = \text{const.} \quad (4.30)$$

is constant.

4. In the parallel orientation, the distance variations don't matter as the system is infinitely stable against variations in the particle-shield separation. The critical angular variation however scales like $\Delta\theta_{\text{crit}} \sim (L - R)^3/L^3$ for small distances and like $\Delta\theta_{\text{crit}} \sim L^2$ shown in fig. 4.9. it is therefore possible to determine the minimum separation $L_{\text{min}} > R$ for a given placement accuracy.
5. Using the required separation, one can calculate $\tau \in (0, 1]$ using eq. (4.30) and look up the maximal possible entanglement in the top right of fig. 4.3 after an evolution time τt_{max} .

As an example, the radius is fixed as $R = 10 \mu\text{m}$ and the superposition size is $\Delta x = 100 \text{ nm}$. Let's say that such a particle can be placed with an accuracy of $\Delta\theta = 10^{-7} \text{ rad}$ and a coherence time of 1 s is reachable. Using the steps outlined above, the required minimum particle-shield separation is around $L \approx 15R$ and the maximal amount of measurable entanglement is given by $E_N \approx 9.2 \times 10^{-3}$. For more entanglement, either a heavier particle, a larger superposition size, a higher placement accuracy or larger coherence times are required. It is therefore actually possible, to bring the particles closer together than without the Faraday shield and still measure entanglement. One is only limited by the placement accuracy and repeatability.

5 The consequences of a thermal shield

The primary goal of the Faraday shield is to enable closer particle separations than would be possible without it, thereby enhancing gravitational interaction and reducing the required coherence times. This limit of $L \lesssim 100 \mu\text{m}$ has been discussed in section 2.3. Until now, the shield's dynamics and properties have been neglected. However, at non-zero temperatures, thermal vibrations of the shield could significantly affect entanglement generation. In this chapter, first an estimates of the required shield size is given followed by examining the impact of thermal vibrations for both large and small shields on entanglement generation. In the experiment, the trapped particles are cooled to their motional ground state to enable effective quantum control and the generation of spatial superpositions. Liquid helium at $T \approx 4 \text{ K}$ is commonly used for cooling but cryogenic dilution refrigerators can cool small setups down to temperatures as low as $T \approx 20 \text{ mK}$ [50]. These temperatures serve as reference points for the relevant calculations.

5.1 Thickness and size of the shield

The thickness d and the radius r_s of the spherical shield can be estimated by considering the properties of a real conductive material with high electrical conductivity σ . Even a superconducting shield could be considered for an almost perfect shielding of electromagnetic fields. For a shield, the transmission T of electromagnetic waves is given by [51]

$$T = \left| \frac{\mathbf{E}_{\text{after}}}{\mathbf{E}_{\text{before}}} \right| = \frac{2}{Z_0 \sigma d} \quad (5.1)$$

where $Z_0 = 377 \Omega$ is the impedance of free space (assuming the shield is placed in a vacuum or in air). The electric conductivity σ is highly dependent on the temperature [52, p. 284-286], decreasing approximately as $1/T^5$ at low temperatures¹². Copper offers a strong electric conductivity of $\sigma = 59.6 \times 10^6 \text{ S/m}$ but this value increases significantly at cryogenic temperatures, with measured data showing $\sigma(T = 10) \approx 1.5 \times 10^{10} \text{ S/m}$ [53].

¹²This behavior is valid for temperatures below the Debye temperature ($\Theta_D = 343 \text{ K}$ for copper). At the low temperatures used in the experiment, this model accurately describes the conductivity of metals [53].

To determine the shield's thickness, the primary criterion is that gravitational interactions should dominate the entanglement generation. Other mutual interactions between the particles, such as Coulomb or Casimir forces, must be sufficiently suppressed by the shield. The **entanglement rate** Γ quantifies the build-up of entanglement over time

$$\Gamma = \left. \frac{d}{dt} E_N(\rho) \right|_{t=0} \quad (5.2)$$

where E_N is an appropriate entanglement measure - in this case the logarithmic negativity [19] introduced in section 2.2. For gravitational interactions, the entanglement rate in the parallel orientation is given by using eq. (2.23) as

$$\Gamma_{\text{Gravity}} = \frac{GM_A M_B \Delta x_A \Delta x_B}{16\hbar L^3 \log 2} = \frac{G\pi^2 R^6 \rho_{\text{Silica}}^2 (\Delta x)^2}{9\hbar L^3 \log 2}. \quad (5.3)$$

where in the last step $M_A = M_B = 4/3\pi R^3 \rho_{\text{Silica}}$ and $\Delta x_A = \Delta x_B \equiv \Delta x$ was used. The entanglement rate for non-gravitational interactions, such as Coulomb or Casimir forces, must be significantly smaller than the gravitational entanglement rate, ideally by a factor $\chi > 1$. This ensures that the measured entanglement is primarily due to gravitational interactions. In the following sections, estimations about the thickness and size of the shield are made, to effectively screen Coulomb and Casimir forces.

5.1.1 Shielding Coulomb-Interactions

The primary role of the Faraday shield is to block electromagnetic interactions between particles. Experimentally, it may be beneficial for the particles to carry a small amount of charge enabling the use of electrostatic traps with high trapping strength and large controllability [24]. The Coulomb interaction potential between the particles is given by

$$V = \frac{1}{4\pi\epsilon_0} \frac{q_A q_B}{2L} \quad (5.4)$$

where $\epsilon_0 = 8.8542 \times 10^{-12} \text{ A}^2 \text{ s}^4 \text{ m}^{-3} \text{ kg}^{-1}$ is the permittivity of free space and $|q_{A(B)}| = e = 1.6022 \times 10^{-19} \text{ C}$ the charge of particle A and B respectively. This interaction mimics the form of the gravitational potential and can similarly induce entanglement with a entanglement rate identical as in eq. (5.3)

$$\Gamma_{\text{Coulomb}} = \frac{T |q_A q_B| (\Delta x)^2}{64\pi\epsilon_0 \hbar L^3 \log 2}. \quad (5.5)$$

The shield suppresses the coupling by a factor of T . Requiring $\Gamma_{\text{Gravity}} > \chi \Gamma_{\text{Coulomb}}$, the minimum thickness of the shield can be calculated as

$$T \frac{|q_A q_B|}{64\pi\epsilon_0} \times \chi < \frac{G\pi^2 R^6 \rho_{\text{Silica}}^2}{9} \quad (5.6)$$

$$\iff d > \frac{9}{32} \frac{1}{Z_0 \sigma} \frac{1}{\pi^3 \epsilon_0 G \rho_{\text{Silica}}^2} \frac{e^2}{R^6} \times \chi. \quad (5.7)$$

The thickness strongly depends on the particles size R , as large particles with large mass will favors gravitational entanglement generation. Assuming the particles are silica nano-spheres with parameters given in table 4.1, a minimum shield-thickness of $d \approx 10 \text{ nm} \times \chi$ at 4 K and of $d \approx 2.5 \mu\text{m} \times \chi$ at room temperature is required. At low temperatures, a realistic shield thickness could therefore be $d = 100 \text{ nm}$, balancing engineering practicality and electromagnetic suppression. Exact estimations however depend on the realization of the experiment as well as the precision in which the evolved state is measurable.

Electrostatic fields can still propagate around the finite-sized Faraday shield and potentially still induce entanglement. It is however possible to estimate the required shield radius r_s to block a specific amount η of the electric field (see appendix A.4):

$$\frac{r_s}{L} = \sqrt{\frac{1 - (1 - \eta)^2}{(1 - \eta)^2}} \quad (5.8)$$

The results are visualized in fig. 5.1. The shield's transmission T should therefore be

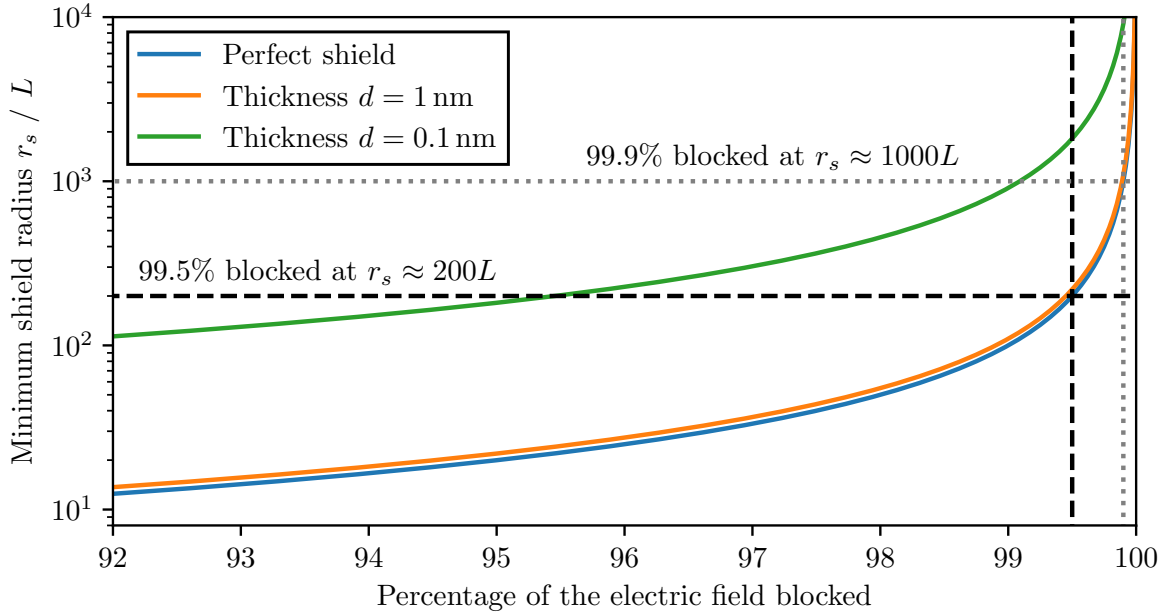


Figure 5.1: Shield radius as a function of the shielding effectiveness η for an ideal shield. Additionally, a real shield with varying thicknesses d is considered at $T = 300 \text{ K}$. To achieve shielding of $99.5 - 99.9\%$ ($\eta = 0.995 - 0.999$), a radius of $r_s = 200 - 1000L$ is needed.

modified to $\tilde{T} = T\eta + (1 - \eta)$, where the shield effectiveness η depends on r_s as given by eq. (5.8). Eq. (5.6) is modified, requiring a minimum effectiveness η_{\min} for sufficient shielding:

$$\eta_{\min} \approx 1 - \frac{64\pi^3 \epsilon_0 G R^6 \rho_{\text{Silica}}^2}{9e^2}. \quad (5.9)$$

Using again the parameters from table 4.1, a minimum effectiveness of $\eta_{\min} \gtrsim 0.99997$ and thus a radius of $r_s \gtrsim 28000L \approx 60$ cm is required. This shield is too large for all practical purposes and it might be beneficial to choose heavier masses ($\tilde{M} \sim 4M$) to reduce the shield size to the orders of ~ 1 cm. Due to practicality, a shield of $r_s = 1$ cm is used in the following calculations. Using uncharged particles eliminates Coulomb interactions, and therefore reducing the shield's size to only shield Casimir interactions.

5.1.2 Shielding Casimir-Interactions

Similarly to Coulomb interactions, it is possible to estimate the required thickness for a shield to sufficiently block Casimir interactions. The Casimir potential between the spheres with radius R separated by $2L$ is given by [37]

$$V = -\frac{23\hbar c}{4\pi \cdot 128L^7} \left(\frac{\varepsilon_r - 1}{\varepsilon_r + 2} \right)^2 R^6. \quad (5.10)$$

The corresponding entanglement rate is calculated similar to before by expanding the potential in small Δx and computing the logarithmic negativity:

$$\Gamma_{\text{Casimir}} = T^2 \frac{161}{4096} \frac{cR^6(\Delta x)^2}{\pi L^9 \log 2} \left(\frac{\varepsilon_r - 1}{\varepsilon_r + 2} \right)^2. \quad (5.11)$$

The dependence on T^2 is only a systematic guess but should be sufficient for a basic estimation as Casimir and van der Waals forces are second order effects in the dipole-dipole interaction [27]. Requiring gravitational entanglement to dominate, $\Gamma_{\text{Gravity}} > \chi \Gamma_{\text{Casimir}}$, leads to

$$T^2 \frac{161cR^6}{4096\pi L^6} \left(\frac{\varepsilon_r - 1}{\varepsilon_r + 2} \right)^2 \times \chi < \frac{G\pi^2 \rho_{\text{Silica}}^2 R^6}{9\hbar} \quad (5.12)$$

$$\iff d > \sqrt{\frac{1449}{4096} \frac{c\hbar}{G\pi^3}} \frac{2}{Z_0 \sigma \rho L^3} \frac{\varepsilon_r - 1}{\varepsilon_r + 2} \times \sqrt{\chi}. \quad (5.13)$$

For large separations, the shield thickness can go arbitrarily low, as Casimir forces vanish. At separations $L \gtrsim 100 \mu\text{m}$, the shield might not be required at all (compare section 2.3). Assuming two identical silica nano-spheres with parameters given by table 4.1, the required minimum thickness is between $4 \times 10^{-11} \text{ m} \times \sqrt{\chi}$ at 4 K and $10 \text{ nm} \times \sqrt{\chi}$ at room temperature. This is much thinner than what is required for shielding Coulomb interactions. The factor ε_r modifies the thickness by up to a factor of 1 and is therefore negligible in these calculations.

However, very thin shields lose mechanical rigidity, leading to enhanced vibrational excitations and potential instabilities. Vibrational frequency and thus the vibrational energy depends linearly on the shield's thickness, making thinner shields prone to large thermal vibrations. A detailed analysis of these effects is provided in the subsequent section.

5.1.3 Gravitational effects of the shield

The gravitational interaction between the masses and the shield is generally neglected because it has no significant impact on the entanglement generation between the particles. The only potential effect is indirect entanglement mediated by the thermal oscillations of the shield, as both masses couple gravitationally to it. However, as shown in section 5.3, this second-order effect is very weak and does not pose a problem, since it still represents gravitationally mediated entanglement - which is the focus of the experiment anyway. The gravitational force between a sphere with mass M and a infinitesimal mass segment $dm = r d\rho_{\text{Cu}} dr d\varphi$ of the shield made of copper with density $\rho_{\text{Cu}} = 8960 \text{ kg/m}^3$ at a distance r from the shield's center is given by

$$d\mathbf{F} = \frac{GMdm}{\ell} \hat{\ell} \Rightarrow dF_z = \frac{GM r \rho_{\text{Cu}} d}{\ell^2} dr d\varphi \cos \theta, \quad (5.14)$$

where $\ell^2 = r^2 + L^2$ denotes the distance between the sphere and the mass segment and $\theta = \arccos L/\ell$ is the angle between them. The total attractive force between the mass and the shield with radius r_s is therefore

$$F_z = GM \rho_{\text{Cu}} d L \int_0^{r_s} dr \int_0^{2\pi} d\varphi \frac{r}{(r^2 + L^2)^{3/2}} = 2\pi GM \rho_{\text{Cu}} d \left(1 - \frac{L}{\sqrt{L^2 + r_s^2}} \right). \quad (5.15)$$

For large shields $r_s \gg L$ this is independent of the particle-shield separation L . For a shield with thickness $d = 100 \text{ nm}$ and the usual silica particle, the attraction force is around $F_{\text{particle-shield}} \approx 4.1 \times 10^{-24} \text{ N}$ which is comparable with the attraction gravitational attraction force between the two particles themselves at $F_{\text{particle-particle}} \approx 5.0 \times 10^{-24} \text{ N}$ but is much weaker than the Casimir attraction between the particle and the shield with $F_{\text{Casimir}} \approx 1.4 \times 10^{-17} \text{ N}$. Therefore, the gravitational effect of the shield can be neglected in all practical calculations.

5.2 Thermal shield vibrations

A spherical plate of radius r_s clamped at its edge, can vibrate in distinct modes characterized by indices (k, l) , where $k \in [1, \infty)$ and $l \in [0, \infty)$. The exact vibrational frequencies ω_{kl} and mode shapes u_{kl} are described by Bessel functions. In fact, one of the first occurrences of these functions is linked to Euler's study of vibrating perfectly flexible and infinitely thin membranes [54]. For a plate of a real material with density ρ and thickness d , vibrations are described the differential equation [55, p. 490]

$$D \nabla^2 \nabla^2 u = -\rho d \ddot{u} \quad (5.16)$$

where D , a flexural rigidity constant, is dependent on material properties of the plate like Youngs module E and the Poisson ratio ν as

$$D = \frac{d^3 E}{12(1 - \nu^2)}. \quad (5.17)$$

The general solution of this differential equation is expressed terms of Bessel functions as (derived in Ref. [55, p. 490-495])

$$u_{kl}(r, \theta, t) = \left[J_l(\beta_k r) - \frac{J_l(\beta_k r_s)}{I_l(\beta_k r_s)} I_l(\beta_k r) \right] \cos(l\theta + \phi_1) \sin(\omega_{kl} t + \phi_2) \quad (5.18)$$

with

$$\beta_k = \frac{\tilde{r}_k}{r_s} \quad \text{and} \quad \omega_{kl} = \frac{\tilde{r}_k^2}{r_s^2} \sqrt{\frac{D}{\rho d}} = \tilde{r}_k^2 \frac{d}{r_s^2} \sqrt{\frac{E}{12\rho(1-\nu^2)}}. \quad (5.19)$$

Here, \tilde{r}_k is the k -th root of the equation

$$J_l(\tilde{r}_k) I_{l+1}(\tilde{r}_k) + I_l(\tilde{r}_k) J_{l+1}(\tilde{r}_k) = 0. \quad (5.20)$$

The phases ϕ_1 and ϕ_2 are determined by initial conditions and represent rotational and temporal offsets. The shape of the first 12 modes (k, l) are shown in fig. 5.2. In general, any possible vibration of the plates can be decomposed into a sum of these modes u_{kl} . The amplitude \hat{z} depends on temperature T and is treated as a quantum harmonic oscillator with frequency ω_{kl} . The expectation value of the amplitude $\langle z \hat{z} \rangle$ is obviously zero and the variance $(\Delta \hat{z})^2 = \langle \hat{z}^2 \rangle - \langle \hat{z} \rangle^2$ at temperature T is given by (derivation in appendix A.5)

$$(\Delta \hat{z}_{kl})_T^2 = \frac{\hbar}{2\tilde{m}\omega_{kl}} \coth\left(\frac{\hbar\omega_{kl}}{2k_B T}\right) \approx \frac{k_B T}{\tilde{m}\omega_{kl}^2} \quad (5.21)$$

where $\hbar\omega \ll k_B T$ was used in the last step and $k_B = 1.3806 \times 10^{-23}$ J/K is the Boltzmann constant. The *effective mass* \tilde{m} of the mode, considering the mode's shape, can intuitively be estimated by the average amplitude of the mode

$$\tilde{m} = m \frac{1}{\pi r_s^2} \int_0^{r_s} dr \int_0^{2\pi} r d\theta u_{kl}(r, \theta, t) \quad (5.22)$$

with $m = \rho\pi r_s^2 d$ being the total mass of the plate. The amplitude scales therefore as $\Delta z_{kl} \propto \omega^{-1}$ at high temperatures or for low frequencies.

The effect of infinite modes

For a shield with radius $r_s = 1$ cm $\gg R$ (referred to as the “large shield”) and thickness $d = 100$ nm made out of Copper with $E = 110$ GPa and $\nu = 1/3$, the vibrational frequencies for the first few modes are between 11.0 s $^{-1}$ for $(1, 0)$ up to 1018 s $^{-1}$ for $(7, 6)$. These low frequencies result in vibrational energies $\hbar\omega$ that are much smaller than the thermal energy $k_B T$ at any reasonable temperature. Consequently many vibrational modes are highly populated and even for temperatures of 10^{-6} K, the first 600 modes are equally populated with probabilities close to $1/Z$, where Z is the partition function

$$Z = \sum_{m \in \{(k,l)\}} e^{-\beta \hbar \omega_m}. \quad (5.23)$$

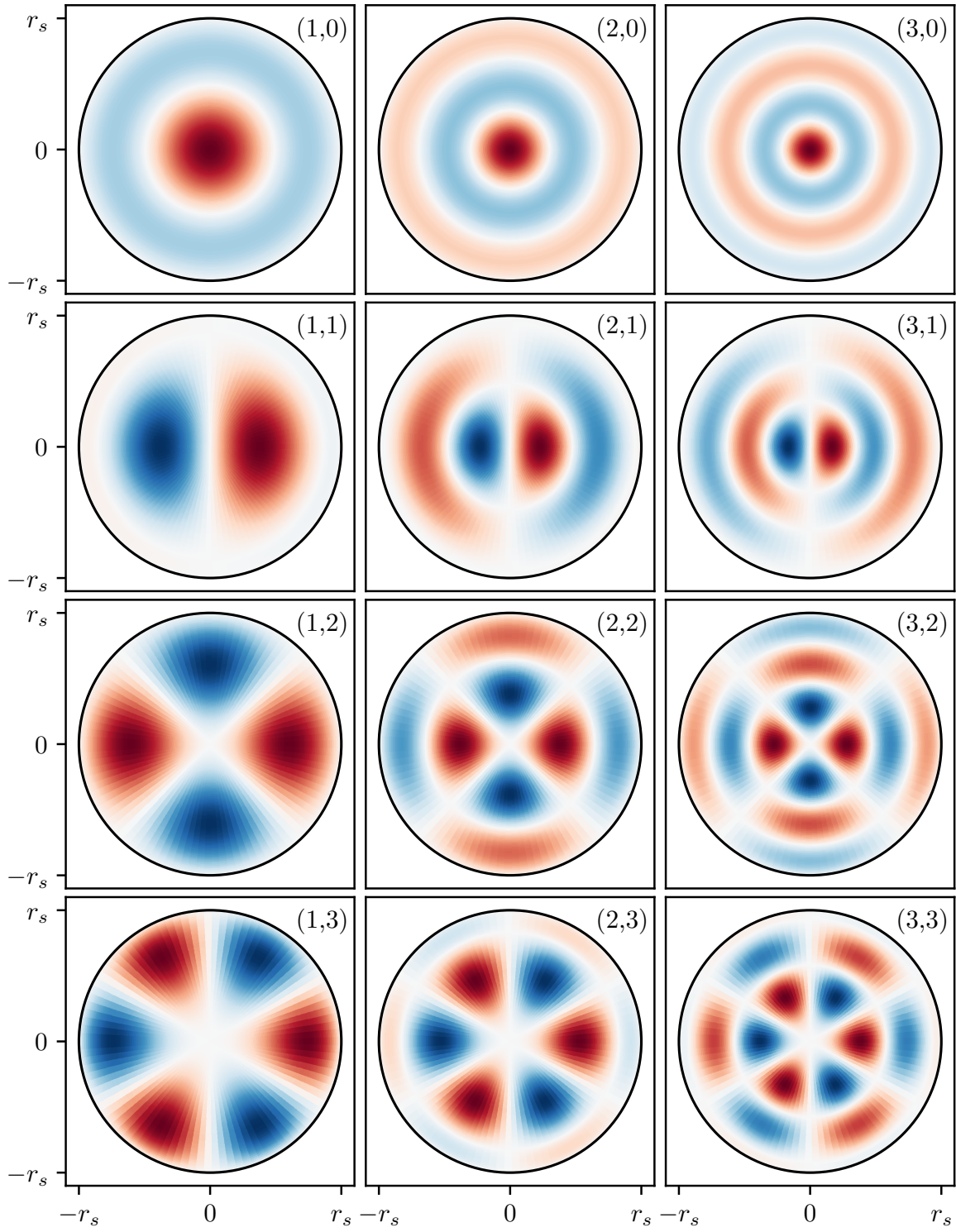


Figure 5.2: Shape of the first 12 modes (k, l) ($k \geq 1$ and $l \geq 0$) of a vibrating spherical plate fixed at the edge with $r_s/d = 1000$.

It is possible to determine the asymptotic increase of frequencies ω_{kl} for high modes $k \rightarrow \infty$. Using the expansion of the Bessel functions for large arguments [56, eq. 10.17.3]

$$J_l(x) \sim \cos\left(x - \frac{l\pi}{2} - \frac{\pi}{4}\right) \quad \text{for } x \rightarrow \infty \quad (5.24)$$

and of the modified Bessel functions for $x \rightarrow \infty$ [56, eq. 10.40.1]

$$I_l(x) \sim \frac{e^x}{\sqrt{2\pi x}} \quad \text{for } x \rightarrow \infty \quad (5.25)$$

the asymptotic expansion of eq. (5.20) can be expressed as

$$\sim \frac{e^x}{\sqrt{2\pi x}} \left[\cos\left(x - \frac{l\pi}{2} - \frac{\pi}{4}\right) + \cos\left(x - \frac{l\pi}{2} - \frac{3\pi}{4}\right) \right] = 0. \quad (5.26)$$

Considering the scaling of J_l for large orders $l \rightarrow \infty$ [56, eq. 10.19.1], the distribution of the zeros \tilde{r}_k becomes periodic for large k and l resulting in an asymptotic scaling of the frequencies ω_{kl} in the order of $\mathcal{O}(k^2 + l^2)$.

Since the amplitude scales inversely with frequency $\Delta z_{kl} \propto 1/\omega_{kl}$, higher modes exhibit a quadratic decrease in amplitude. Additionally, the shape function u_{kl} of higher modes has more bulges, limiting the amplitude further as the available shield-material is distributed over smaller segments of the plate. These effects combine to ensure that higher-order modes have minimal contributions, allowing numerical calculations to focus on the first few modes. Nevertheless, the influence of infinitely many modes can still be approximated asymptotically using the scaling behavior of ω_{kl} .

It is also interesting to consider the scaling of the amplitudes Δz for shields with varying sizes r_s . According to eq. (5.19), the frequency ω increases quadratically as the shield radius r_s decreases. Simultaneously, the effective mass \tilde{m} in eq. (5.22) scales also quadratically with the shield's size, consequently resulting in linear dependence of $\Delta z \sim r_s$ for large temperatures and/or low modes.

5.3 Entanglement in front of a thermal shield

The generation of entanglement between two particles depends heavily on variations in the placement of the particles and the shield, as seen in chapter 4. Shield vibrations can effectively be understood to alter the separation and angle of the cat-state relative to shield, as depicted in fig. 5.3. This approximation is only valid for shields significantly larger than the particle radius ($r_s \gg R$) and for low vibrational frequencies ($1/\omega \approx t_{\max}$), effectively capturing the impact of the first vibrational modes for small l and k . Especially the effect of the first mode (1,0) can be put into the same framework from chapter 4. The interpretation is further supported by findings in section 3.3, showing that the Casimir interaction between a sphere and a tilted plane closely resembles that

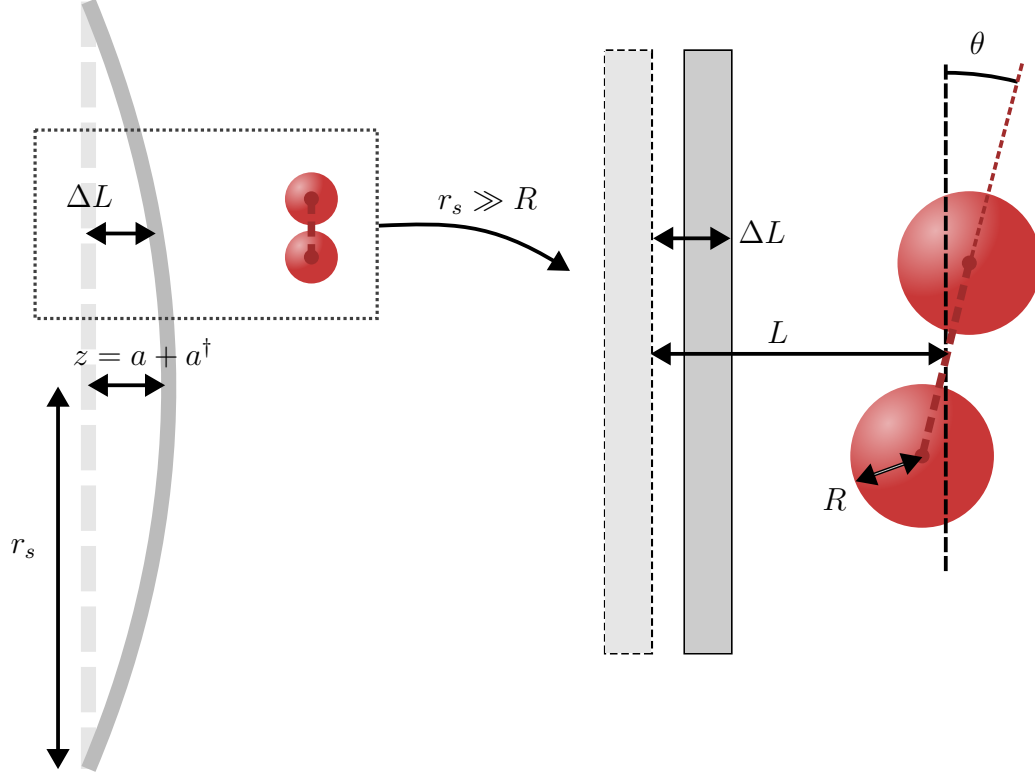


Figure 5.3: For a large ($r_s \gg R$) and locally linearizable shield, thermal vibrations with amplitude z can be interpreted as a static shield where particle A (shown in the figure) is positioned at $L + \Delta L$ with angle θ and particle B at $L - \Delta L$ with angle $-\theta$. Both variations depend solely on the vibrational amplitude. At low vibrational frequencies ($1/\omega \approx t_{\text{max}}$), the amplitude remains nearly static during an experimental run, with thermal fluctuations distributed around $\langle z \rangle = 0$ and variance Δz given by eq. (5.21).

between a sphere and a flat plane. Contrary to the problem considered in chapter 4, here only the thermal amplitude z_{kl} is an independent random variable distributed around $\langle z_{kl} \rangle = 0$ with a standard deviation Δz_{kl} given by eq. (5.21). Variations in the particle-shield separation (ΔL) and angle (θ) are correlated to the vibration amplitude z . For a large and linearizable shield, this can be understood as

$$\theta = \arctan(z |\nabla u|) \approx z |\nabla u| \quad \text{and} \quad \Delta L = z |u| \quad (5.27)$$

where ∇u is the gradient of the vibrational mode's shape. Performing similar calculations to those in chapter 4, the averaged density matrix $\langle \rho \rangle$, dependent on Δz_{kl} , can be derived (see appendix B.2). The resulting entanglement, quantified by logarithmic negativity as a function of temperature T and particle-shield separation L , is given by eq. (B.21) and illustrated in fig. 5.4. At typical experimental temperatures, entanglement in the

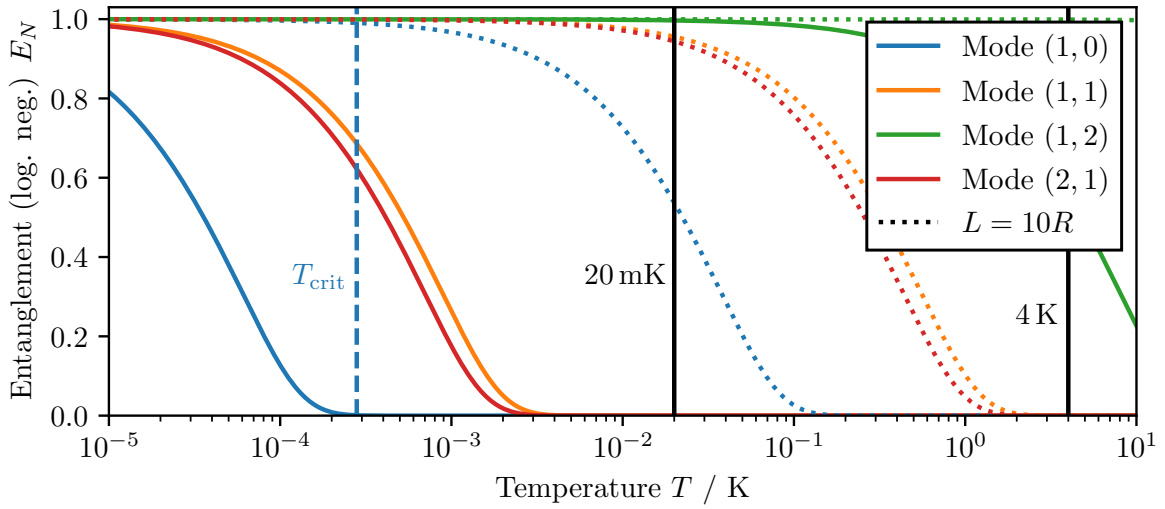


Figure 5.4: Entanglement between the particles (parallel orientation) near a thermal shield at different temperatures T for selected vibrational modes. At a critical temperature $T_{\text{crit},kl}$, entanglement is lost if mode (k, l) is present. This critical point shifts with greater particle-shield separations, following $T_{\text{crit}} \propto L^4$.

presence of the mode $(1, 0)$ is observable only at large particle-shield separations. In fact, the critical temperature T_{crit} scales with the separation L in the large-separation-limit (LSL) as:

$$T_{\text{crit}} \sim (\Delta z_{\text{crit}})^2 \sim \left(\frac{L^5}{t_{\text{max}}} \right)^2 \sim L^4. \quad (5.28)$$

The large separations required are consistent with previous findings, considering that the thermal amplitudes $\Delta z_{1,0} \approx 9 \times 10^{-11}$ m at 20 mK are comparable with the critical values the variation in the shield-particle separation ΔL_{crit} in chapter 4. Interestingly, these results are unaffected by the shield radius r_s , as long as $r_s \gg R$ and the vibrational mode can be locally linearized. This invariance arises because the gradient

$|\nabla u| \propto 1/r_s$ and $z \propto r_s$ perfectly cancel, leaving θ independent of r_s . When the cat state orientation is parallel to the shield, dependence on ΔL is negligible, leaving the entanglement independent of r_s . However, as seen in fig. 5.4, the mode number (k, l) significantly impacts entanglement generation. Higher modes correspond to higher vibrational frequencies and smaller amplitudes Δz , with T_{crit} asymptotically scaling as $\mathcal{O}(k^2 + l^2)$. This behavior is presented in fig. 5.5, where two positions of the particles in front of the plate is considered. If the particle is positioned exactly at the center of

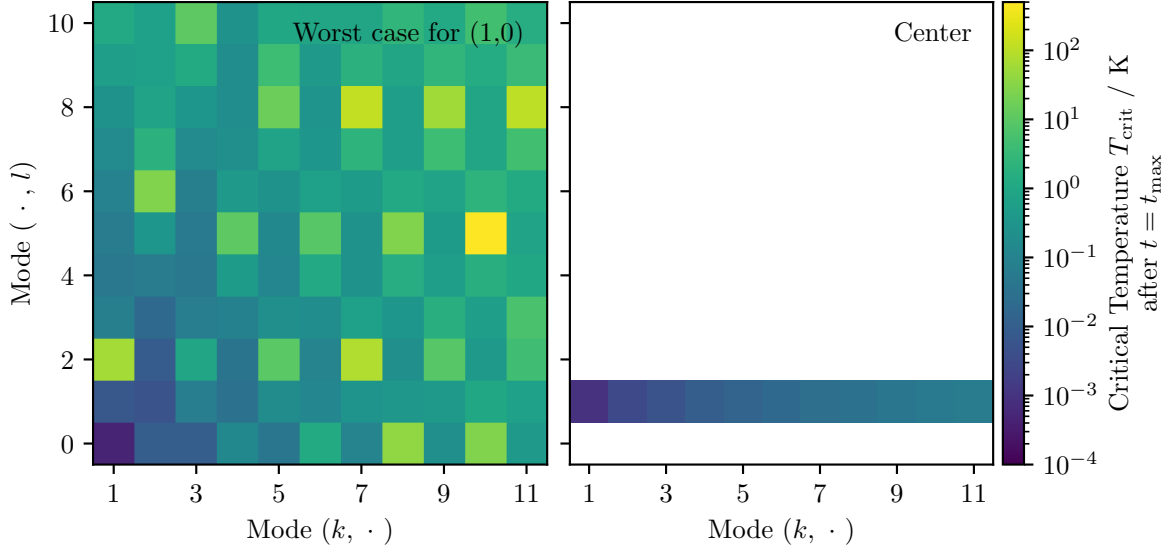


Figure 5.5: Critical temperature T_{crit} , at which no entanglement is measurable anymore for different modes at a separation of $L = 2R = 2\mu\text{m}$. The shape of the vibrational modes is considered. The particle is either placed at the position of the highest gradient of mode $(1, 0)$ (**left**) or in the center of the shield (**right**).

the shield, only specific mode shapes with $l = 2k + 1$, $k \in \mathbb{Z}$ can induce decoherence. For $l \neq 1$, this effect becomes however numerically negligible. If the particle is placed in the worst-case position for the first mode $(1, 0)$, which corresponds to the point of maximum gradient and thus the largest decoherence (approximately at $r \approx 0.0527r_s$), all modes are relevant. It becomes clear that only the first few modes significantly affect entanglement, as higher modes do not disrupt entanglement even at temperatures much higher than those required for entanglement loss.

This method on calculating the decoherence induced due to the thermal shield is only accurate in the specific cases of a large and slow vibrating shield

5.3.1 Analytic dynamics

The effect of the thermal shield on entanglement generation between the two delocalized particles can be calculated analytically. The Hamiltonian governing the interactions between the two particles with each other and with the thermal shield is given by

$$\begin{aligned}
 \hat{H} = & \sum_{\substack{m \in \{(k,l)\} \\ k \geq 1, l \geq 0}} \left\{ \hbar \omega_m \left(\hat{a}_m^\dagger \hat{a}_m + \frac{1}{2} \right) \right. \\
 & + g_{A,m,\text{Cas}}^{(1)} (\hat{a}_m + \hat{a}_m^\dagger) \left(|\psi_A^{(1)}\rangle\langle\psi_A^{(1)}| \otimes \mathbb{1} \right) + g_{A,m,\text{Cas}}^{(2)} (\hat{a}_m + \hat{a}_m^\dagger) \left(|\psi_A^{(2)}\rangle\langle\psi_A^{(2)}| \otimes \mathbb{1} \right) \\
 & + g_{B,m,\text{Cas}}^{(1)} (\hat{a}_m + \hat{a}_m^\dagger) \left(\mathbb{1} \otimes |\psi_B^{(1)}\rangle\langle\psi_B^{(1)}| \right) + g_{B,m,\text{Cas}}^{(2)} (\hat{a}_m + \hat{a}_m^\dagger) \left(\mathbb{1} \otimes |\psi_B^{(2)}\rangle\langle\psi_B^{(2)}| \right) \Big\} \\
 & + g_{\text{Grav}}^{(1,1)} |\psi_A^{(1)}\psi_B^{(1)}\rangle\langle\psi_A^{(1)}\psi_B^{(1)}| + g_{\text{Grav}}^{(1,2)} |\psi_A^{(1)}\psi_B^{(2)}\rangle\langle\psi_A^{(1)}\psi_B^{(2)}| \\
 & + g_{\text{Grav}}^{(2,1)} |\psi_A^{(2)}\psi_B^{(1)}\rangle\langle\psi_A^{(2)}\psi_B^{(1)}| + g_{\text{Grav}}^{(2,2)} |\psi_A^{(2)}\psi_B^{(2)}\rangle\langle\psi_A^{(2)}\psi_B^{(2)}|
 \end{aligned} \tag{5.29}$$

where the gravitational coupling

$$g_{\text{Grav}}^{(ij)} = \frac{GM^2}{L^{(ij)}} \tag{5.30}$$

between the states $|\psi_A^{(i)}\rangle$ and $|\psi_B^{(j)}\rangle$ ($i, j = 1, 2$) is determined by their separation $L^{(ij)}$ from eq. (4.10). The shield's thermal vibrations have no influence on this coupling, hence the solely gravitational interaction is the same as already discussed in chapter 4. Gravitational effects arising from the mass of the shield are omitted in these calculations because they are weaker by a factor of 10^7 compared to the Casimir interactions, as detailed in section 5.1.3.

The interaction between the state $|\psi_{A(B)}^{(i)}\rangle$ and the shield is described by

$$\frac{\hbar c \pi^3}{720} \left(\frac{\varepsilon_r - 1}{\varepsilon_r + 1} \right) \varphi(\varepsilon_r) \frac{R}{(\mathcal{L} + \hat{z}_m u_m(r_{A(B)}^{(i)}))^2} \tag{5.31}$$

which is dependent on the mode m and the mode shape $\hat{z}_m u_m$ at the position $r_{A(B)}^{(i)}$ where the cat-state is positioned in front of, where $\hat{z} = \sqrt{\hbar/2\tilde{m}\omega_m}(\hat{a}_m + \hat{a}_m^\dagger)$ is the amplitude of the vibration. Expanding the term in first order in \hat{z} and ignoring the zeroth-order term which is constant and thus equal to a global phase at the end of the calculations, the Casimir coupling in the Hamiltonian eq. (5.29) is given by

$$g_{A(B),m,\text{Cas}}^{(i)} = g_{\text{PFA}} \frac{2u_m(r_{A(B)}^{(i)})}{\mathcal{L}^3} \sqrt{\frac{\hbar}{2\tilde{m}\omega_m}} \quad \text{with} \quad g_{\text{PFA}} = \frac{\hbar c \pi^3 R}{720} \left(\frac{\varepsilon_r - 1}{\varepsilon_r + 1} \right) \varphi(\varepsilon_r). \tag{5.32}$$

The combined system of the two particles $\rho_{\text{sys.}} \in \mathcal{H}_{\text{sys.}}$ and the thermal modes $\rho_{\text{th}} = \bigotimes_m \rho_{\text{th},m} \in \mathcal{H}_{\text{th}}$ evolves under those interactions from the initial state $\rho_0 = \rho_{\text{th}} \otimes \rho_{\text{sys.}}$.

5 The consequences of a thermal shield

The initial state of the two particles $\rho_{\text{sys.}}$ is given by eq. (2.7) and $\rho_{\text{th},m}$ is the thermal state of vibrational mode m , which can be represented either in the number basis $\{|n\rangle\}$ or in the coherent state basis $\{|\alpha\rangle\}$ as [57]

$$\rho_{\text{th},m} = \frac{1}{Z} \sum_{n=1}^{\infty} e^{-\beta\hbar\omega_m(n+1/2)} |n\rangle\langle n| = \int d\alpha^2 \frac{1}{\pi\bar{n}} e^{-\frac{|\alpha|^2}{\bar{n}}} |\alpha\rangle\langle\alpha|. \quad (5.33)$$

Here, $Z = \text{tr} e^{-\beta\hbar\omega_m(\hat{n}+1/2)} = e^{-\beta\hbar\omega_m/2}/(1 - e^{-\beta\hbar\omega_m})$ is the partition function and $\bar{n} = 1/(e^{\beta\hbar\omega_m} - 1)$ is the average thermal occupation number of mode m at temperature T .

After time t , tracing out the thermal shield yields the evolved two-particle system

$$\rho_{\text{sys.}}(t) = \text{tr}_{\text{th}} \left(\hat{U}(t) \rho_0 \hat{U}^\dagger(t) \right). \quad (5.34)$$

The time evolution is computed in appendix B.3 and is given by

$$\rho_{\text{system}}(t) = \frac{1}{4} \begin{pmatrix} 1 & e^{i\phi_{11,12}} e^{-\gamma_{11,12}} & e^{i\phi_{11,21}} e^{-\gamma_{11,21}} & e^{i\phi_{11,22}} e^{-\gamma_{11,22}} \\ & 1 & e^{i\phi_{12,21}} e^{-\gamma_{12,21}} & e^{i\phi_{12,22}} e^{-\gamma_{12,22}} \\ & & 1 & e^{i\phi_{21,22}} e^{-\gamma_{21,22}} \\ & & & 1 \end{pmatrix} \quad (5.35)$$

with the decoherence terms

$$\gamma_{ii',jj'} = \sum_m \frac{4}{\hbar^2 \omega_m^2} \left| (g_{\text{A},m,\text{Cas}}^{(i)} + g_{\text{B},m,\text{Cas}}^{(i')}) - (g_{\text{A},m,\text{Cas}}^{(j)} + g_{\text{B},m,\text{Cas}}^{(j')}) \right|^2 \sin^2 \left(\frac{\omega_m t}{2} \right) \left[\bar{n} + \frac{1}{2} \right] \quad (5.36)$$

and the phases (where the gravitational part is already given by eq. (2.13))

$$\begin{aligned} \phi_{ii',jj'} = \sum_m \frac{1}{\hbar} \left(g_{\text{Grav}}^{(ii')} - g_{\text{Grav}}^{(jj')} \right) t \\ + \frac{\sin(\omega_m t) + \omega_m t}{\hbar^2 \omega_m^2} \left[(g_{\text{A},m,\text{Cas}}^{(i)} + g_{\text{B},m,\text{Cas}}^{(i')})^2 - (g_{\text{A},m,\text{Cas}}^{(j)} + g_{\text{B},m,\text{Cas}}^{(j')})^2 \right]. \end{aligned} \quad (5.37)$$

At $T = 0$, decoherence terms persist, but their effect is significant only for strong Casimir interactions (e.g., small separations $L \sim R$) The decoherence scales as $\gamma \propto \omega_m^{-4}$ from which the asymptotic dependence on the modes $\mathcal{O}(k^{-8} + l^{-8})$ follows. It is therefore possible to estimate the combined effect of the first N modes as

$$\sim \frac{1}{\zeta(8)} \sum_{n=1}^N \frac{1}{n^8} \quad (5.38)$$

where ζ is the Riemann zeta function, which converges very fast to 1, even for small N . At specific times $t = 2\pi k/\omega_m$, $k \in \mathbb{N}$ the decoherence from mode m vanishes, leading to entanglement values close to the ideal case, aligning with the findings in Ref. [58]. This periodic behavior is confirmed in fig. 5.6, showing a measurable amount of entanglement only close to these specific times. The full width at half maximum (FWHM) of these

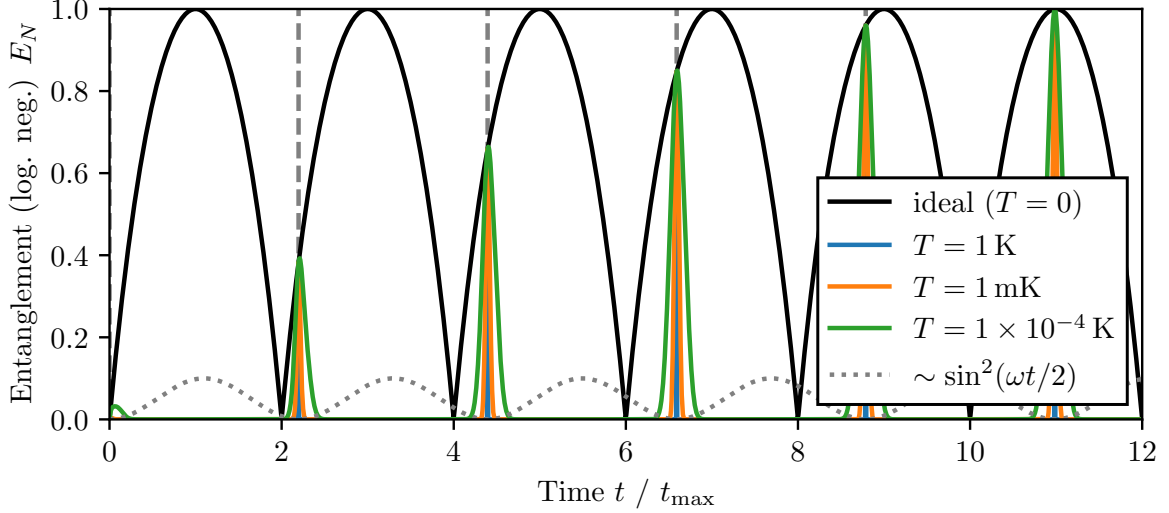


Figure 5.6: Entanglement dynamics in front of a thermal shield in mode $(1, 0)$ at different temperatures. Only at specific times $2\pi k/\omega_{1,0} \approx k \times 576 \text{ ms}$, $k \in \mathbb{N}$, entanglement is observable. This aligns with the findings in Ref. [58]. The particle and shield parameters are taken from table 4.1.

observed peaks is approximated by

$$\text{FWHM} \approx \frac{4}{\omega} \sqrt{\frac{\log 2}{\gamma}} \propto \frac{1}{\sqrt{n}}. \quad (5.39)$$

For high temperatures, entanglement is only measurable in a very short window around time $2\pi/\omega_m$.

The resulting decoherence of multiple modes is given by the sum of all individual modes, decaying rapidly with the mode number as seen in eq. (5.38). Ideal entanglement as without the shield is never achieved due to the quasi-periodicity of the system; the frequency ratios $\omega_i/\omega_j \notin \mathbb{Q}$ for $i \neq j$ ¹³ prevent exact repetition of the resulting sinusoidal summation. The entanglement dynamics of the first combined 50 vibrational modes numerically are shown in fig. 5.7. This figure highlights the dominant contribution of the first mode $(1, 0)$, with realistically measurable entanglement primarily occurring at $t = 2\pi/\omega_{1,0}$. Even for temperatures as low as 20 mK, entanglement remains minimal due to rapid decoherence - at least for small separations. Increasing the particle-shield separation reduces Casimir coupling $g_{\text{Cas}} \propto \mathcal{L}^{-3}$ and hence delaying decoherence but simultaneously slowing gravitational entanglement generation down ($t_{\text{max}} \propto L^3$). The combined effect is therefore qualitatively given by $\gamma \propto g_{\text{Cas}}^2 \sin^2(t) \propto L^{-6} \sin^2(L^3) \xrightarrow{L \gg R} 0$. The dependence of the entanglement on the particle-shield separation at two specific points in time is shown in fig. 5.8.

¹³While not rigorously proven, this conclusion is supported by the transcendental nature of the zeros of the Bessel functions [59] and the non-integer frequency ratio $\omega_{1,0}/\omega_{1,1} \notin \mathbb{Z}$, which on its own should already ensure quasi-periodic behavior.

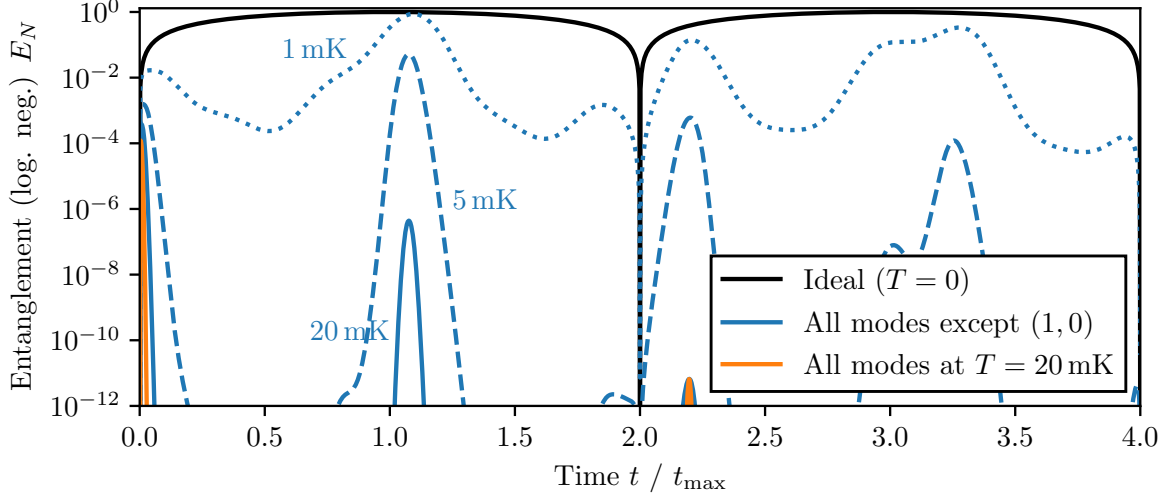


Figure 5.7: Entanglement dynamics in front of a thermal shield. **Orange:** The first 50 modes have been used in the numeric calculation. The effect of all remaining modes is around $1.7 \times 10^{-11} \%$. **Blue:** Results excluding the $(1, 0)$ mode at varying temperatures ranging from 1 mK up to 20 mK. The parameters for the particle and the shield are taken from table 4.1.

By measuring after time $t_{\max} \approx 259 \text{ ms}$, in the ideal scenario without the shield, a maximally entangled state with $E_N = 1$ is observed. Although $2\pi/\omega_{1,0} = \text{const.}$ is constant, t_{\max} increases with L , creating specific separations (e.g. for $L \approx 2.6R$) where the two times align, enhancing observability. For even larger L , decoherence effects eq. (5.36) diminish, making entanglement measurable even at higher temperatures.

By measuring at the time $2\pi/\omega_{1,0} \approx 576 \text{ ms}$ where the decoherence of the first mode (with the largest effect on total decoherence) almost vanishes, entanglement can be observed by increasing the particle-shield separation. However, measuring at a constant time independent of L limits the maximum of possibly reachable entanglement as the gravitational entanglement rate slows down and increasing t_{\max} .

The radius of the shield also has a large impact on entanglement generation. Smaller shields with larger mode frequencies result in a decreased and faster oscillating decoherence term $\gamma \propto \sin^2(\omega)1/\omega_m^2$. The time between the points, where the decoherence effect of the first mode almost vanishes (i.e. every $\Delta t = 2\pi/\omega_{1,0} \propto r_s^2$), decreases for smaller shields and thus making entanglement measurable more frequently at almost any point in time. Numeric calculations show, that even for shields as large as $r_s = 5 \text{ mm}$, entanglement of around $E_N \lesssim 1$ can be measured at $T = 20 \text{ mK}$ and even at close separations (see fig. C.1).

Examining the phases $\phi_{ii',jj'}$ in eq. (5.37) reveals that, similar to the gravitational force, the Casimir interaction between the particle and the shield can induce entanglement between the particles. This occurs as both particles couple to the shield via Casimir in-

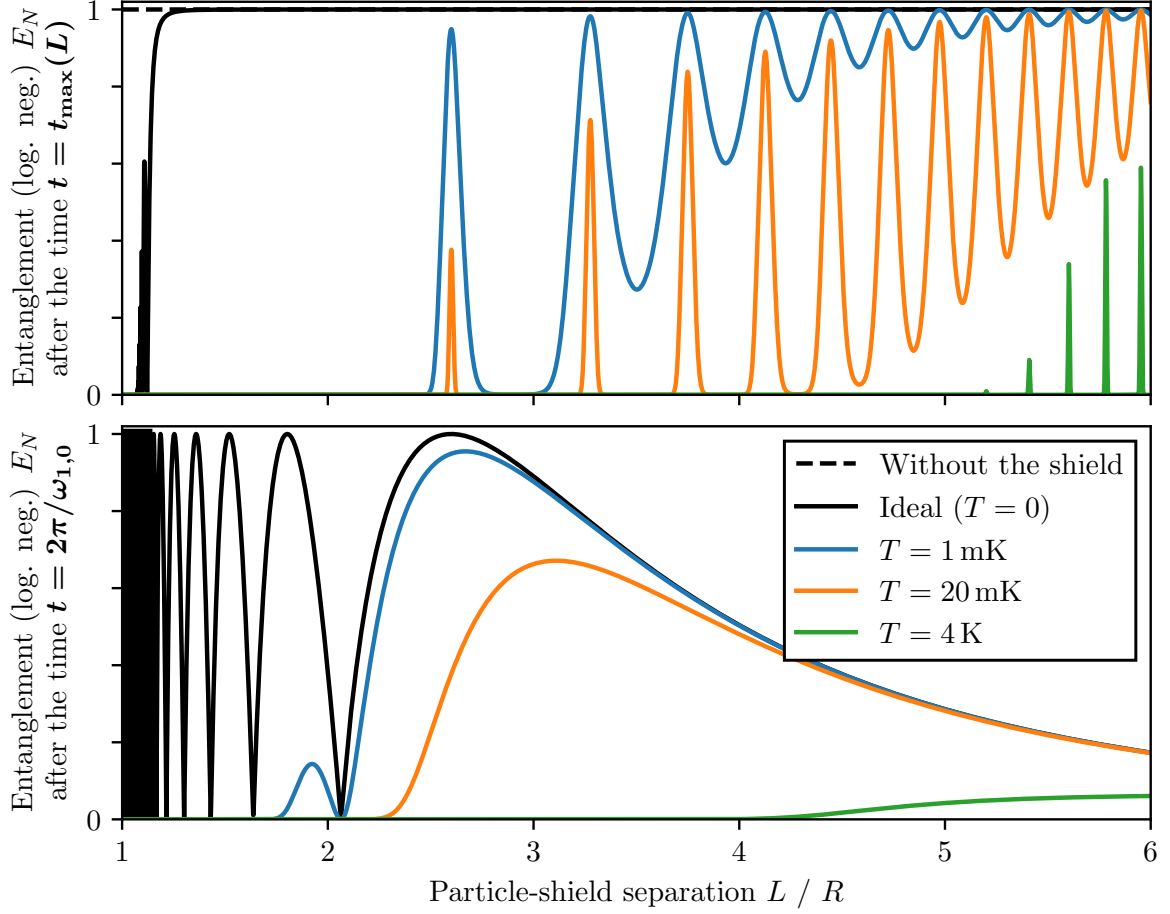


Figure 5.8: Entanglement at various particle-shield separations $L > R$ at time $t_{\max}(L)$ (eq. (4.16)) (**top**) and $t_2\pi/\omega_{1,0} \approx 576$ ms (**bottom**). Calculations use parameters from table 4.1 and are performed at different temperatures.

interactions, enabling indirect interaction between them. However, the resulting amount of entanglement is very small, as evident from the dependence on $1/\hbar^2$ in eq. (5.37). While negligible at larger separations, Casimir-induced indirect entanglement could become significant at very small distances where the Casimir forces are much stronger than the gravitational interaction. This is particularly relevant if the entanglement generated via Casimir interactions approaches that due to gravity. The relative strength can be estimated by comparing the term corresponding to the gravitational interaction with the Casimir terms in eq. (5.37):

$$g_{\text{Grav}} t \gtrsim \frac{\sin(\omega_m t) + \omega_m t}{\hbar \omega_m^2} g_{\text{Cas}}^2 \quad (5.40)$$

$$\Rightarrow \frac{GM^2}{2L} \gtrsim g_{\text{PFA}} \frac{1}{\mathcal{L}^3} \sqrt{\frac{\hbar}{2\tilde{m}\omega_m}} \quad (5.41)$$

where $\langle \sin(\omega t) \rangle = 0$ was averaged. Using the parameters for the particles and the shield from table 4.1, the lower bound for the separation is given by $L > 1.29 \times 10^{-5} \text{ m} \approx 1.3R$. For separations $L \gtrsim 2.7R$, gravitational entanglement becomes 100 times stronger than that due to Casimir interactions. These separations are most likely fulfilled either way considering the results from the previous chapters. Thus, indirect entanglement from Casimir forces can be neglected for larger separations.

5.3.2 Small shields

A small shield only can block the direct Casimir interactions between the particles A and B , hence it can only be used if no other forms of electromagnetic interactions between the particles such as Coulomb coupling are present. For very small shields in the size of the particles $r_s \sim R + \Delta x/2$, the above considerations are not fully applicable, as they assume the linearization of the vibrational mode at the particle scale. The vibrations of the shield and the resulting vibrational modes substantially alter the Casimir potential, which is no longer determined solely by the interaction between a perfectly flat shield and a spherical particle. For a small shield, deformations can no longer be approximated locally as a flat, tilted plate; instead, the precise shape of the vibrational mode must be accounted for. As discussed in section 3.3, deformations, such as those resembling the first vibrational mode, significantly impact the resulting Casimir potential which is, in the proximity-force approximation, upper bounded by an interaction equivalent to that between a sphere and a plate with separation $\mathcal{L} \pm \Delta z$.

In the temporal domain, vibrational frequencies scale quadratically with the shield size, $\omega \propto 1/r_s^2$, which results in the measuring process being multiple times longer than a single vibrational period. Consequently, Casimir interactions are effectively averaged, leading to an effectively planar and flat shield. This agrees with the findings in the previous section and the results shown in fig. C.1, where smaller shields exhibit drastically reduced decoherence effects.

Similar reasoning applies to higher vibrational modes in arbitrarily large shields. These modes, characterized by high frequencies and a roughly uniform distribution of deformations, effectively average out the Casimir interactions in the temporal domain as well as because of the findings in section 3.3, preserving entanglement.

5.4 Discussions of the effects of the thermal shield

In this chapter, two different strategies to calculate the effect of a thermal shield at temperature T on the entanglement generation have been considered.

The naive approach described in section 5.3 assumes the shield to be locally flat and static over the measurement time. Vibrational amplitudes z_{kl} are treated statically and normally distributed over multiple measurements with each mode inducing random phase shifts, similar to the placement variations considered in chapter 4. This approach greatly overestimates the dynamics by assuming maximal effects from all vibrational modes occur simultaneously. In reality however, different modes might cancel themselves partially out reducing the overall total deformation. Furthermore this approximation is only valid for large and thus linearizable shields ($r_s \gg R$) and low vibrating frequencies $\omega_{kl} \approx t_{\max}$.

The second method calculates analytically the particles entanglement by solving the Hamiltonian dynamics for small amplitude $\Delta z \ll L$. This method provides a more accurate depiction of the time-dependent system and reveals that entanglement can partially recover even for small separations and large shields at specific times, notably at $2\pi/\omega_{1,0}$.

The effects of the thermal shield can be mitigated by reducing the decoherence effects via the following methods:

Lowering the shield's temperature Reducing the temperature of the setup and the shield decreases vibrational amplitudes and the associated decoherence. Temperatures around 4 K are desirable as they are experimentally accessible using liquid helium cooling. Temperatures as low as 20 mK are theoretically reachable by $^3\text{He}/^4\text{He}$ dilution refrigerators [50, 60]. All cooling mechanisms however induce additional vibrational noise due to their mechanical components and additional studies about the effect of such noise has to be considered.

Increasing the particle-shield separation Larger separations reduce the relative effect of the vibrations as $\Delta z/L \rightarrow 0$. In the naive approach section 5.3, separations of at least $L \gtrsim 10R$ are required making the shield almost unnecessary, as for similar separations, the Casimir interactions between both particles are smaller than the gravitational interaction (see discussion in section 2.3). The presence of the shield could even potentially worsen the entanglement generation. In the more detailed and analytical method in section 5.3.1, separations of around $5R$ are possible, but requiring measurement at very precise points in time.

Reducing the shield's radius Decreasing r_s does increase the vibrational frequencies quadratically ($\omega_{kl} \propto 1/r_s^2$) and simultaneously decreases the amplitudes $\Delta z_{kl} \sim r_s$. The results in the naive approach are independent of the shield's radius. However, for small shields with large frequencies, this method is applicable. The analytical approach on the other hand shows a strong dependence on the shield's radius r_s where halving the radius nearly restores entanglement for small separations (see fig. C.1). A reduction in r_s is however only possible for uncharged, neutral particles that do not interact via a direct Coulomb interaction, necessitating magnetic or optical trapping methods.

By combining these approaches, the thermal shield's impact can be mitigated, creating better conditions for entanglement generation. Measurements might be possible only at specific and precise points in time, particularly at $2\pi/\omega_{kl}$ with fluctuations limited to approximately $\Delta t \sim 1/\sqrt{\bar{n}} \approx \sqrt{\omega_{1,0}/T}$. Achieving accurate measurements at arbitrary times would require either lower temperatures or larger particle-shield separations, as suggested by the results of the naive method in section 5.3.

For very small shields, which are only considerable for uncharged particles that can solely couple through mutual Casimir interactions, the Casimir forces cannot be simplified to a sphere interacting with a perfectly flat plate. Instead, mode shapes must be taken into account, slightly modifying the interaction. Although challenging to estimate, the rapid frequency increase to $2\pi/\omega \ll t_{\max}$ during the measurement period suggests that shield vibrations would average out over time. Thus, uncharged particles and therefore small shields are greatly preferable.

Improvements on the rigidity of the shield can also be considered. Reinforcing the shield, for instance with a cross structure of thicker material, could reduce vibration frequencies of the shield by effectively reducing the size and increasing the overall thickness. Alternative shield designs, such as a star shape, might also be beneficial by potentially offering more uniformly distributed and higher-frequency vibrations. For rectangular plates, frequency increases are marginal, scaling by $\omega_{kl} = (k^2 + l^2)/(2r_s)^2 \sqrt{D\pi^4/\rho d}$ [55, p. 471-474] and thus improving entanglement generation only at most up to a constant.

6 Discussion and outlook

Testing the quantum nature of gravity is notoriously difficult due to its relative weakness compared to the other fundamental forces. The concept of gravitationally induced entanglement as evidence for the non-classicality of gravity was first proposed by Feynman at the 1957 Chapel Hill Conference. Since then, several experimental proposals have emerged [3, 6], all aiming on measuring entanglement between macroscopic delocalized masses after direct gravitational coupling. A common approach to prevent electromagnetic interactions such as Coulomb or Casimir forces, involves placing a conductive Faraday shield between the particles [25].

In this work, it was shown by calculating the relative dynamical phase build-up, that Casimir interactions between two macroscopic Schrödinger-cat states and a conducting Faraday shield can destroy all measurable entanglement if small stochastic variations in the initial setup or thermal motion of the shield are present. Placement accuracies in the initialization of the cat-states should stay below a threshold, depending on the achievable magnitudes in superposition size and particle masses, usually well below $\Delta\theta \lesssim 10^{-8}$ rad and $\Delta L \lesssim 10^{-9}$ m. To mitigate the decoherence effects of the thermal shield, measurements at very precise points in time are required, where the particular effects of the first vibrational mode minimize.

The calculated bounds for the placement parameters and the measurement accuracy appears to be very difficult or even practically impossible to implement experimentally in near future. In general, the entanglement generation can be improved by increasing either the particles superposition size, its mass or by choosing larger particle-shield separations, which reduces the relative effect of the variations in the placement as well as decoherence effects of the thermal shield. The primary goal of the Faraday shield is to allow for tighter particle separations as the gravitational coupling is no longer dominated by the inter-particle Casimir forces. This is however only partially possible under specific circumstances, as established in this work, as certain setups would perform better without the shield. In section 4.4 a schema for choosing the optimal parameters is presented, given known experimental constraints in the preparation of the delocalized Schrödinger-cat states and in the placement accuracy. By choosing the shield as small as possible and temperatures as low as physically reachable, thermal decoherence weakens, improving entanglement generation. Uncharged particles - requiring a much smaller shield in the size of the silica-nanospheres - are therefore preferable over charged particles.

For a more precise characterization of the experimental challenges, squeezed gaussian states [61, p. 33-64] should be considered in addition to Schrödinger-cat-like states.

Most experimental realizations of spatial superpositions of massive objects, especially in the world of high mass levitated particles, are going to be ideally close to squeezed gaussian states [23, Timestamp: 23:00] as they can be naturally prepared by ground state cooling in a harmonic trap [62]. However, the findings in Ref. [10] suggest that the results derived from cat-states should remain largely applicable.

Other forms of decoherence, such as undamped vibrations of the setup - potentially due to complex cooling mechanisms like dilution refrigerators - and black-body radiation of the particles can also be considered. It is possible to estimate the decoherence due to thermal radiation [63, p. 127-136] between the cat-states as well as with the thermal environment at temperature T as [64]

$$\Gamma_{\text{decoherence}} \propto 1 - \exp\left\{-\frac{(\Delta x)^2}{\lambda_{\text{th}}^2}\right\} \sim (\Delta x)^2 \quad (6.1)$$

where $\lambda_{\text{th}} = \pi^{2/3}\hbar c/k_B T$ is the thermal wavelength with values of $\lambda_{\text{th}} \approx 1$ mm at 4 K. For $\Delta x \ll \lambda_{\text{th}}$, the decoherence scales quadratically in Δx , resulting in a similar increase as the gravitational entanglement rate Γ_{Gravity} from eq. (5.3). For very large superposition sizes, decoherence stays constant resulting in a domination of gravitational entanglement generation. Similarly to variations in the initial particle placement for each run, variations in other parameters, such as the measurement time (i.e. the time of gravitational interaction between the states) can be considered. A brief investigation of this effect was presented in Ref. [41], showing results consistent with those obtained in this thesis.

Another avenue worth looking into with potentially large experimental improvements lies in the enhancement of the results by knowing the exact initial placement of each separate run - or at least a skewed probability distribution of the parameters. The decoherence effects in the average measurement can then be corrected for during the data analysis step. This would allow for greater tolerance of variations in the initial setup.

The findings in this thesis have broader implications beyond gravitationally induced entanglement, as a new method for the precise measurement of Casimir forces can be developed utilizing spatial delocalizations. The idea of using levitated particles for observing Casimir interactions is a current research topic [65]. By positioning a single Schrödinger-cat superposition state close to a large thermally vibrating plate, dephasing effects similar to the ones discussed in section 5.3.1 are expected due to the slightly different interactions of each superposition component with the plate. Measuring this dephasing offers a way to determine the Casimir coupling strength between arbitrarily shaped objects and a flat plane with high precision. Moreover, this approach could be extended to measure Casimir-Polder interactions between atoms or molecules and a plane. Current technologies, as demonstrated in matter-wave experiments [13], could be sufficient even today. Experimental setups designated for gravitational entanglement sensing can be adapted for these measurements, providing a new and precise tool for testing modern theories of Casimir interactions.

In essence, this thesis offers an overview and an estimation of previously overlooked

experimental issues with proposed experiments on quantum gravity. By addressing these problems, this work partially paves the way for the possible experimental realization of measuring gravitationally induced entanglement, which ultimately advances the quest for a grand unifying theory of quantum gravity.

Bibliography

- [1] N. Maskelyne, “A proposal for measuring the attraction of some hill in this kingdom by astronomical observations”, *Philosophical Transactions of the Royal Society of London* **65**, 495–499 (1775) 10.1098/rstl.1775.0049.
- [2] R. D. Davies, “A Commemoration of Maskelyne at Schiehallion”, *Quarterly Journal of the Royal Astronomical Society* **26**, 289–294 (1985).
- [3] T. Krisnanda, G. Y. Tham, M. Paternostro, and T. Paterek, “Observable quantum entanglement due to gravity”, *npj Quantum Information* **6**, 10.1038/s41534-020-0243-y (2019) 10.1038/s41534-020-0243-y, arXiv:1906.08808.
- [4] H. Chevalier, A. J. Paige, and M. S. Kim, “Witnessing the nonclassical nature of gravity in the presence of unknown interactions”, *Physical Review A* **102**, 022428 (2020) 10.1103/physreva.102.022428, arXiv:2005.13922.
- [5] J. S. Pedernales, G. W. Morley, and M. B. Plenio, “Motional Dynamical Decoupling for Matter-Wave Interferometry”, *Phys. Rev. Lett.* **125**, 023602 (2019) 10.1103/physrevlett.125.023602, arXiv:1906.00835.
- [6] S. Bose, A. Mazumdar, G. W. Morley, H. Ulbricht, M. Toroš, M. Paternostro, A. Geraci, P. Barker, M. S. Kim, and G. Milburn, “A Spin Entanglement Witness for Quantum Gravity”, *Phys. Rev. Lett.* **119**, 240401 (2017) 10.1103/physrevlett.119.240401, arXiv:1707.06050.
- [7] L. Lami, J. S. Pedernales, and M. B. Plenio, “Testing the quantum nature of gravity without entanglement”, *Phys. Rev. X* **14**, 021022 (2023) 10.1103/physrevx.14.021022, arXiv:2302.03075.
- [8] R. Horodecki, P. Horodecki, M. Horodecki, and K. Horodecki, “Quantum entanglement”, *Rev. Mod. Phys.* **81**, 865–942 (2007) 10.1103/revmodphys.81.865, arXiv:quant-ph/0702225.
- [9] M. B. Plenio and S. Virmani, “An introduction to entanglement measures”, *Quantum Information & Computation* **7**, 1–51 (2005), arXiv:quant-ph/0504163.
- [10] J. S. Pedernales and M. B. Plenio, “On the origin of force sensitivity in tests of quantum gravity with delocalised mechanical systems”, *Contemporary Physics* **64**, 147–163 (2023) 10.1080/00107514.2023.2286074, arXiv:2311.04745.
- [11] D. Carney, P. C. E. Stamp, and J. M. Taylor, “Tabletop experiments for quantum gravity: a user’s manual”, *Classical and Quantum Gravity* **36**, 034001 (2018) 10.1088/1361-6382/aaf9ca, arXiv:1807.11494.

- [12] M. Christodoulou, A. Di Biagio, M. Aspelmeyer, Č. Brukner, C. Rovelli, and R. Howl, “Locally mediated entanglement in linearised quantum gravity”, *Physical Review Letters* **130**, 100202 (2022) 10.1103/physrevlett.130.100202, arXiv:2202.03368.
- [13] Y. Y. Fein, P. Geyer, P. Zwick, F. Kiałka, S. Pedalino, M. Mayor, S. Gerlich, and M. Arndt, “Quantum superposition of molecules beyond 25 kDa”, *Nature Physics* **15**, 1242–1245 (2019) 10.1038/s41567-019-0663-9.
- [14] T. Westphal, H. Hepach, J. Pfaff, and M. Aspelmeyer, “Measurement of Gravitational Coupling between Millimeter-Sized Masses”, *Nature* **591**, 225–228 (2021) 10.1038/s41586-021-03250-7, arXiv:2009.09546.
- [15] H. B. G. Casimir, “On the attraction between two perfectly conducting plates”, *Proc. Kon. Ned. Akad. Wet.* **51**, 793 (1948).
- [16] H. B. G. Casimir and D. Polder, “The Influence of Retardation on the London-van der Waals Forces”, *Physical Review* **73**, 360–372 (1948) 10.1103/physrev.73.360.
- [17] L. Gurvits, “Classical deterministic complexity of Edmonds’ problem and Quantum Entanglement”, in *Proceedings of the thirty-fifth annual acm symposium on theory of computing*, Vol. 4, STOC03 (June 2003), pages 10–19, 10.1145/780542.780545, arXiv:quant-ph/0303055.
- [18] G. Vidal and R. F. Werner, “A computable measure of entanglement”, *Phys. Rev. A* **65**, 032314 (2001) 10.1103/physreva.65.032314, arXiv:quant-ph/0102117.
- [19] M. Plenio, “Logarithmic negativity: a full entanglement monotone that is not convex.”, *Physical Review Letters* **95**, 090503 (2005) 10.1103/PhysRevLett.95.090503, arXiv:quant-ph/0505071.
- [20] A. D. O’Connell, M. Hofheinz, M. Ansmann, R. C. Bialczak, M. Lenander, E. Lucero, M. Neeley, D. Sank, H. Wang, M. Weides, J. Wenner, J. M. Martinis, and A. N. Cleland, “Quantum ground state and single-phonon control of a mechanical resonator”, *Nature* **464**, 697–703 (2010) 10.1038/nature08967.
- [21] R. L. DeBiase, “Are Casimir Forces Conservative?”, *Physics Procedia* **38**, 18–33 (2012) 10.1016/j.phpro.2012.08.008.
- [22] B. Yi, U. Sinha, D. Home, A. Mazumdar, and S. Bose, “Massive spatial qubits: Testing macroscopic nonclassicality and Casimir entanglement”, *Physical Review Research* **5**, 033202 (2023) 10.1103/physrevresearch.5.033202, arXiv:2106.11906.
- [23] M. Aspelmeyer, *Quantum sources of gravity: the next frontier of macroscopic quantum physics*, <https://www.youtube.com/watch?v=0AVDrVY-rTw>, Timestamp: 51:00, May 2024.

- [24] C. Gonzalez-Ballester, M. Aspelmeyer, L. Novotny, R. Quidant, and O. Romero-Isart, “Levitodynamics: levitation and control of microscopic objects in vacuum”, *Science* **374**, 10.1126/science.abg3027 (2021) 10.1126/science.abg3027, arXiv:2111.05215.
- [25] T. W. van de Kamp, R. J. Marshman, S. Bose, and A. Mazumdar, “Quantum Gravity Witness via Entanglement of Masses: Casimir Screening”, *Phys. Rev. A* **102**, 062807 (2020) 10.1103/physreva.102.062807, arXiv:2006.06931.
- [26] F. London, “Zur Theorie und Systematik der Molekularkräfte”, *Zeitschrift für Physik* **63**, 245–279 (1930) 10.1007/bf01421741.
- [27] M. Bordag, U. Mohideen, and V. M. Mostepanenko, “New developments in the Casimir effect”, *Physics Reports* **353**, 1–205 (2001) 10.1016/s0370-1573(01)00015-1, arXiv:quant-ph/0106045 [quant-ph].
- [28] G. L. Klimchitskaya, U. Mohideen, and V. M. Mostepanenko, “The Casimir force between real materials: Experiment and theory”, *Reviews of Modern Physics* **81**, 1827–1885 (2009) 10.1103/revmodphys.81.1827, arXiv:0902.4022.
- [29] S. K. Lamoreaux, “The Casimir force: background, experiments, and applications”, *Reports on Progress in Physics* **68**, 201–236 (2004) 10.1088/0034-4885/68/1/r04.
- [30] M. Bordag, “Proceedings of the Fourth Workshop on Quantum Field Theory under the Influence of External Conditions”, in *The Casimir Effect 50 Years Later* (June 1999), pages 1–410, 10.1142/9789814527576.
- [31] T. H. Boyer, “Quantum Electromagnetic Zero-Point Energy of a Conducting Spherical Shell and the Casimir Model for a Charged Particle”, *Physical Review* **174**, 1764–1776 (1968) 10.1103/physrev.174.1764.
- [32] L. H. Ford, “Casimir Force between a Dielectric Sphere and a Wall: A Model for Amplification of Vacuum Fluctuations”, *Phys. Rev. A* **58**, 4279–4286 (1998) 10.1103/physreva.58.4279, arXiv:quant-ph/9804055.
- [33] E. M. Lifshitz, “The theory of molecular attractive forces between solids”, *Sov. Phys. JETP* **2**, 73–83 (1956) 10.1016/b978-0-08-036364-6.50031-4.
- [34] M. Hartmann, “Casimir effect in the plane-sphere geometry: Beyond the proximity force approximation”, PhD thesis (Universität Augsburg, July 2018).
- [35] T. Emig, “Fluctuation induced quantum interactions between compact objects and a plane mirror”, *Journal of Statistical Mechanics: Theory and Experiment* **2008**, P04007 (2007) 10.1088/1742-5468/2008/04/p04007, arXiv:0712.2199.
- [36] A. Bulgac, P. Magierski, and A. Wirzba, “Scalar Casimir effect between Dirichlet spheres or a plate and a sphere”, *Physical Review D* **73**, 025007 (2006) 10.1103/physrevd.73.025007.
- [37] T. Emig, N. Graham, R. L. Jaffe, and M. Kardar, “Casimir forces between arbitrary compact objects”, *Phys. Rev. Lett.* **99**, 170403 (2007) 10.1103/physrevlett.99.170403, arXiv:0707.1862.

- [38] I. G. Pirozhenko and M. Bordag, “On the Casimir repulsion in sphere-plate geometry”, *Physical Review D* **87**, 085031 (2013) 10.1103/physrevd.87.085031, arXiv:1302.5290.
- [39] K. Perlin, “An image synthesizer”, *SIGGRAPH Comput. Graph.* **19**, 287–296 (1985) 10.1145/325165.325247.
- [40] J. F. Clauser, M. A. Horne, A. Shimony, and R. A. Holt, “Proposed Experiment to Test Local Hidden-Variable Theories”, *Physical Review Letters* **23**, 880–884 (1969) 10.1103/physrevlett.23.880.
- [41] H. C. Nguyen and F. Bernards, “Entanglement dynamics of two mesoscopic objects with gravitational interaction”, *The European Physical Journal D* **74**, 10.1140/epjd/e2020-10077-8 (2020) 10.1140/epjd/e2020-10077-8, arXiv:1906.11184.
- [42] K. F. Riley, *Mathematical methods for physics and engineering*, edited by M. P. Hobson and S. J. Bence, Third edition, Hier auch später erschienene, unveränderte Nachdrucke (Cambridge University Press, Cambridge, 2018), 1333 pages.
- [43] A. C. Berry, “The accuracy of the Gaussian approximation to the sum of independent variates”, *Transactions of the American Mathematical Society* **49**, 122–136 (1941) 10.1090/s0002-9947-1941-0003498-3.
- [44] S. Rijavec, M. Carlesso, A. Bassi, V. Vedral, and C. Marletto, “Decoherence effects in non-classicality tests of gravity”, *New Journal of Physics* **23**, 043040 (2020) 10.1088/1367-2630/abf3eb, arXiv:2012.06230.
- [45] K. C. Lee, M. R. Sprague, B. J. Sussman, J. Nunn, N. K. Langford, X.-M. Jin, T. Champion, P. Michelberger, K. F. Reim, D. England, D. Jaksch, and I. A. Walmsley, “Entangling Macroscopic Diamonds at Room Temperature”, *Science* **334**, 1253–1256 (2011) 10.1126/science.1211914.
- [46] M. Bild, M. Fadel, Y. Yang, U. von Lüpke, P. Martin, A. Bruno, and Y. Chu, “Schrödinger cat states of a 16-microgram mechanical oscillator”, *Science* **380**, 274–278 (2022) 10.1126/science.adf7553, arXiv:2211.00449.
- [47] D. Grass, J. Fesel, S. G. Hofer, N. Kiesel, and M. Aspelmeyer, “Optical trapping and control of nanoparticles inside evacuated hollow core photonic crystal fibers”, *Applied Physics Letters* **108**, 10.1063/1.4953025 (2016) 10.1063/1.4953025, arXiv:1603.09393.
- [48] B. R. Slezak, C. W. Lewandowski, J.-F. Hsu, and B. D’Urso, “Cooling the motion of a silica microsphere in a magneto-gravitational trap in ultra-high vacuum”, *New Journal of Physics* **20**, 063028 (2018) 10.1088/1367-2630/aacac1, arXiv:1802.03424 [quant-ph].
- [49] W. P. Schleich, “Waves à la WKB”, in *Quantum Optics in Phase Space* (John Wiley & Sons, Ltd, Berlin, Feb. 2001) Chap. 5, pages 153–169.
- [50] H. Zu, W. Dai, and A. T. A. M. de Waele, “Development of dilution refrigerators - A review”, *Cryogenics* **121**, 103390 (2022) 10.1016/j.cryogenics.2021.103390.

- [51] G. A. E. Vandenbosch, “The basic concepts determining electromagnetic shielding”, *American Journal of Physics* **90**, 672–681 (2022) 10.1119/5.0087295.
- [52] R. Gross and A. Marx, *Festkörperphysik*, 3., akt. Aufl, De Gruyter Studium (De Gruyter, Berlin, 2018), 11066 pages.
- [53] R. Berman, D. K. C. Macdonald, and F. E. Simon, “The thermal and electrical conductivity of copper at low temperatures”, *Proceedings of the Royal Society of London. Series A. Mathematical and Physical Sciences* **211**, 122–128 (1952) 10.1098/rspa.1952.0029.
- [54] J. Dutka, “On the Early History of Bessel Functions”, *Archive for History of Exact Sciences* **49**, 105–134 (1995).
- [55] S. S. Rao, *Vibration of Continuous Systems*, 2nd Edition (Wiley, Jan. 2019), 10.1002/9781119424284.
- [56] F. W. J. Olver, A. B. Olde Daalhuis, D. W. Lozier, B. I. Schneider, R. F. Boisvert, C. W. Clark, B. R. Miller, B. V. Saunders, H. S. Cohl, M. A. McClain, and eds., *NIST Digital Library of Mathematical Functions*, <https://dlmf.nist.gov/>, Release 1.2.2 of 2024-09-15, 2024.
- [57] M. O. E. Steiner, J. S. Pedernales, and M. B. Plenio, “Pentacene-Doped Naphthalene for Levitated Optomechanics”, 10.48550/ARXIV.2405.13869 (2024) 10.48550/ARXIV.2405.13869, arXiv:2405.13869 [quant-ph].
- [58] J. S. Pedernales, K. Streltsov, and M. B. Plenio, “Enhancing Gravitational Interaction between Quantum Systems by a Massive Mediator”, *Physical Review Letters* **128**, 110401 (2021) 10.1103/physrevlett.128.110401, arXiv:2104.14524.
- [59] L. Lorch and M. E. Muldoon, “Transcendentality of zeros of higher derivatives of functions involving Bessel functions”, *International Journal of Mathematics and Mathematical Sciences* **18**, 551–560 (1995) 10.1155/s0161171295000706.
- [60] P. Das, R. B. de Ouboter, and K. W. Taconis, “A Realization of a London-Clarke-Mendoza Type Refrigerator”, in *Ninth international conference on low-temperature physics* (1965), pages 1253–1255, 10.1007/978-1-4899-6443-4_133.
- [61] A. Serafini, *Quantum Continuous Variables: A Primer of Theoretical Methods*, 1st ed. (CRC Press, July 2017), 10.1201/9781315118727.
- [62] T. Weiss, M. Roda-Llordes, E. Torrontegui, M. Aspelmeyer, and O. Romero-Isart, “Large Quantum Delocalization of a Levitated Nanoparticle Using Optimal Control: Applications for Force Sensing and Entangling via Weak Forces”, *Physical Review Letters* **127**, 023601 (2020) 10.1103/physrevlett.127.023601, arXiv:2012.12260.
- [63] M. Schlosshauer, *Decoherence and the Quantum-To-Classical Transition*, 1st edition (Springer, Berlin, Heidelberg, July 2007), 10.1007/978-3-540-35775-9.

- [64] O. Romero-Isart, “Quantum superposition of massive objects and collapse models”, *Physical Review A* **84**, 052121 (2011) 10.1103/physreva.84.052121, arXiv:1110.4495.
- [65] Z. Xu, P. Ju, K. Shen, Y. Jin, Z. Jacob, and T. Li, “Observation of non-contact Casimir friction”, 10.48550/ARXIV.2403.06051 (2024) 10.48550/ARXIV.2403.06051, arXiv:2403.06051.
- [66] M. A. Nielsen and I. L. Chuang, *Quantum computation and quantum information*, 10th anniversary ed. (Cambridge University Press, Cambridge, 2010), 1676 pages.
- [67] D. J. Griffiths, *Elektrodynamik, Eine Einführung*, edited by U. Schollwöck, 4th edition (Pearson, Hallbergmoos, 2018), 1711 pages.
- [68] S. Blanes, F. Casas, J. A. Oteo, and J. Ros, “The Magnus expansion and some of its applications”, *Physics Reports* **470**, 151–238 (2008) 10.1016/j.physrep.2008.11.001, arXiv:0810.5488 [math-ph].

A Ancillary calculations

A.1 Evolution under a gravitational Hamiltonian

In this section the time evolution of a system under Hamiltonian eq. (2.3) is calculated a) using the gravitational interaction \hat{H}_G as a perturbation b) using an exact time evolution of coherent states.

A.1.1 Using time dependent perturbation theory

A general biparty Fock state $|\psi_0\rangle = |kl\rangle$ with $k, l \in \mathbb{N}_0$ can be evolved in time under a Hamiltonian eq. (2.3) treating the gravitational interaction $H_G = -\hbar g(\hat{a}_1\hat{a}_2^\dagger + \hat{a}_1^\dagger\hat{a}_2)$ as a perturbation. The resulting state $|\psi(t)\rangle$ after some time t is in the most general form given as

$$|\psi(t)\rangle = \sum_{i,j \geq 0} c_{i,j}(t) |i, j\rangle \quad (\text{A.1})$$

where the coefficients $c_{i,j}(t)$ are given by first order perturbation theory as

$$c_{i,j}(t) = c_{i,j}(t=0) - \frac{i}{\hbar} \int_0^t dt' \langle ij | \hat{H}_G | kl \rangle e^{-i(E_{kl} - E_{ij})t'/\hbar}. \quad (\text{A.2})$$

The exponent is given by the energy of the appropriate Fock states $E_{kl} - E_{ij} = \hbar\omega(k + l - (i + j))$ and the matrix element in the integrand can be calculated to

$$\langle ij | \hat{H}_G | kl \rangle = \begin{cases} -\hbar g & \text{if } i = k \pm 1 \text{ and } j = l \mp 1 \\ 0 & \text{otherwise} \end{cases}. \quad (\text{A.3})$$

The coefficients for $t = 0$ are trivially given from the initial state as

$$c_{i,j}(t=0) = \begin{cases} 1 & \text{for } i, j = k, l \\ 0 & \text{otherwise} \end{cases}. \quad (\text{A.4})$$

For the non-zero states the energies in the exponent equate to zero and the evolved state is given by (up to a normalization)

$$|\psi(t)\rangle = |kl\rangle - igt |k-1, l+1\rangle - igt |k+1, l-1\rangle + \mathcal{O}(g^2). \quad (\text{A.5})$$

The result eq. (2.5) is represented by eq. (A.5) for the case of $k = 1$ and $l = 0$.

A.1.2 Using an exact time evolution

The Hamiltonian eq. (2.3) can be rewritten using symmetric and antisymmetric normal modes

$$\hat{a}_{\pm} = \frac{1}{\sqrt{2}}(\hat{a}_1 \pm \hat{a}_2) \quad (\text{A.6})$$

in the form of

$$\hat{H} = \hbar\omega_+ \hat{a}_+^\dagger \hat{a}_+ + \hbar\omega_- \hat{a}_-^\dagger \hat{a}_-, \quad \omega_{\pm} = \omega \pm (-g) \quad (\text{A.7})$$

The initial state consisting of two coherent oscillator states is in the new modes given by

$$|\psi(t)\rangle = |\alpha\rangle_1 |\beta\rangle_2 = \left| \frac{1}{\sqrt{2}}(\alpha + \beta) \right\rangle_+ \left| \frac{1}{\sqrt{2}}(\alpha - \beta) \right\rangle_- \quad (\text{A.8})$$

A general coherent state $|\gamma\rangle$ evolves in time under an Hamiltonian $\hat{H} = \hbar\omega \hat{a}^\dagger \hat{a}$ like $|\gamma(t)\rangle = |e^{-i\omega t}\gamma\rangle$ which can be used to evolve the state in eq. (A.8):

$$|\psi(t)\rangle = \left| \frac{1}{\sqrt{2}}e^{-i\omega_+ t}(\alpha + \beta) \right\rangle_+ \left| \frac{1}{\sqrt{2}}e^{-i\omega_- t}(\alpha - \beta) \right\rangle_- \quad (\text{A.9})$$

$$= |e^{-i\omega t}(\alpha \cos gt - \beta \sin gt)\rangle_1 |e^{-i\omega t}(-\alpha \sin gt + \beta \cos gt)\rangle_2, \quad (\text{A.10})$$

where in the last line the back-transformation from the \pm -modes (A.8) was used.

A.2 Exemplary calculation of E_N

In this section, the logarithmic negativity E_N eq. (2.21) is exemplary calculated for the state eq. (2.13). The density matrix of this system is given by

$$\rho(t) = |\psi(t)\rangle\langle\psi(t)| = \frac{1}{4} \begin{pmatrix} 1 & e^{i\Delta\phi} & e^{i\Delta\phi} & 1 \\ e^{-i\Delta\phi} & 1 & 1 & e^{-i\Delta\phi} \\ e^{-i\Delta\phi} & 1 & 1 & e^{-i\Delta\phi} \\ 1 & e^{i\Delta\phi} & e^{i\Delta\phi} & 1 \end{pmatrix}. \quad (\text{A.11})$$

Consequently, the partially transposed density ρ^{Γ_B} is given by

$$\rho^{\Gamma_B}(t) = \frac{1}{4} \begin{pmatrix} 1 & e^{-i\Delta\phi} & e^{i\Delta\phi} & 1 \\ e^{i\Delta\phi} & 1 & 1 & e^{-i\Delta\phi} \\ e^{-i\Delta\phi} & 1 & 1 & e^{i\Delta\phi} \\ 1 & e^{i\Delta\phi} & e^{-i\Delta\phi} & 1 \end{pmatrix}. \quad (\text{A.12})$$

The eigenvalues were calculated using *Mathematica* and equate to

$$\left\{ \sin^2\left(\frac{\Delta\phi}{2}\right), \cos^2\left(\frac{\Delta\phi}{2}\right), \frac{\sin \Delta\phi}{2}, -\frac{\sin \Delta\phi}{2} \right\}$$

According to lemma 2.1, $\|\rho^{\Gamma_B}\|_1$ is given by the sum of the absolute eigenvalues, which is equal to $1 + |\sin \Delta\phi|$. The negativity as the absolute sum of all negative eigenvalues (demonstrated in proposition 2.3) equates to $\mathcal{N} = |\sin \Delta\phi|/2$. Both methods result in a logarithmic negativity of $E_N = \log_2(1 + |\sin \Delta\phi|)$.

A.3 Polarizability of a dielectric sphere

The polarizability α is defined via

$$\mathbf{E}_\infty \alpha = \mathbf{p}, \quad (\text{A.13})$$

where \mathbf{p} is the induced dipole moment and \mathbf{E}_∞ is the external electric field that induces the dipole moment. For a linear and uniform dielectric, it is given as $\mathbf{p} = \mathcal{V}\varepsilon_0(\varepsilon_r - 1)\mathbf{E}_\text{in}$ [67, p. 220-226]. Here, \mathcal{V} is the volume of the object and \mathbf{E}_in is the electric field inside the dielectric. The electrostatic boundary conditions for the problem are given by

$$V_\text{in}|_{r=R} = V_\text{out}|_{r=R} \quad \text{and} \quad \varepsilon_r \varepsilon_0 \frac{\partial V_\text{in}}{\partial r} \Big|_{r=R} = \varepsilon_0 \frac{\partial V_\text{out}}{\partial r} \Big|_{r=R} \quad (\text{A.14})$$

and the electric potential outside of the sphere at $r \rightarrow \infty$ should be equal to the external dipole-inducing field $V_\text{out}|_{r \rightarrow \infty} = -\mathbf{E}_\infty \cdot \mathbf{r} = -E_\infty r \cos \theta$. The electric potential inside and outside the sphere can be calculated using the spherical decomposition of the general electric potential $V \propto 1/|\mathbf{r} - \mathbf{r}'|$ into Legendre Polynomials P_l [67, p. 188-190]:

$$V_\text{in}(r, \theta) = -E_\infty r \cos \theta + \sum_{l=0}^{\infty} A_l r^l P_l(\cos \theta), \quad (\text{A.15})$$

$$V_\text{out}(r, \theta) = -E_\infty r \cos \theta + \sum_{l=0}^{\infty} \frac{B_l}{r^{l+1}} P_l(\cos \theta). \quad (\text{A.16})$$

Applying both boundary conditions, it follows that [67, p. 249-251]

$$\begin{cases} A_l = B_l = 0 \\ A_1 = -\frac{3}{\varepsilon_r + 2} E_\infty, \quad B_1 = \frac{\varepsilon_r - 1}{\varepsilon_r + 2} R^3 E_\infty \end{cases} \quad \text{for } l \neq 1, \quad (\text{A.17})$$

and the resulting homogenous electric field $\mathbf{E}_\text{in} = -\nabla V_\text{in}$ inside the sphere is given as

$$\mathbf{E}_\text{in} = \frac{3}{\varepsilon_r + 2} \mathbf{E}_\infty. \quad (\text{A.18})$$

The field is shown on the right in ?? .The polarizability α of the sphere can be now be determined to

$$\alpha_\text{sphere} = 4\pi\varepsilon_0 R^3 \left(\frac{\varepsilon_r - 1}{\varepsilon_r + 2} \right). \quad (\text{A.19})$$

Depending on the definition, sometimes the factor $4\pi\varepsilon_r$ is dropped.

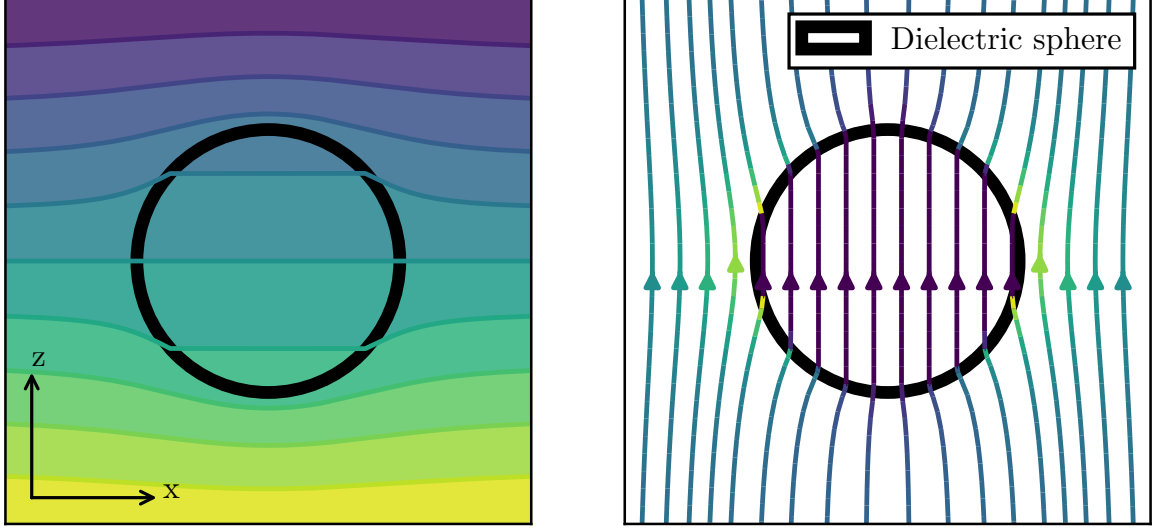


Figure A.1: **left:** Electric potential V of a dielectric sphere in an external electric field $\mathbf{E}_\infty \parallel \mathbf{e}_z$. **right:** The corresponding electric field lines inside and outside the dielectric sphere.

A.4 Blocking of the shield

Assume two spheres A and B with charge q_A and q_B separated by a distance $2L$ on the x -axis. A circular shield is placed perfectly in the center of the spheres orthogonal to the direct connection between them. The magnitude of the field at a distance z in the direction \mathbf{e}_x from this connection line is given by

$$E_x(z) = \frac{L(q_A - q_B)}{4\pi\epsilon_0(L^2 + z^2)^{3/2}} \quad (\text{A.20})$$

The total flux the circular shield with radius r_s is given by

$$\Phi = \int_0^{r_s} dz \int_0^{2\pi} z d\varphi E_x(z) = \frac{(q_A - q_B)}{2\epsilon_0} \left[1 - \frac{L}{\sqrt{L^2 + r_s^2}} \right]. \quad (\text{A.21})$$

Comparing the total flux for $r_s \rightarrow \infty$ with the flux through the shield, one can arrive at the charge-independent **effectiveness** η of the shield as

$$\eta = \frac{\Phi}{\Phi_\infty} = 1 - \frac{L}{\sqrt{L^2 + r_s^2}} \quad (\text{A.22})$$

and thus a shield with radius

$$r_s = L \sqrt{\frac{1 - (1 - \eta)^2}{(1 - \eta)^2}} \quad (\text{A.23})$$

will block a fraction η of the total field.

A.5 Thermal harmonic oscillator

The amplitude z of a single vibrational shield-mode (k, l) with frequency $\omega_{kl} \equiv \omega$ behaves like a quantum harmonic oscillator. The average amplitude $\langle z \rangle_n = 0$. The variance $(\Delta z)^2 = \langle z^2 \rangle - \langle z \rangle^2$ however is given by

$$(\Delta z)_n^2 = \langle z^2 \rangle_n = \frac{\hbar}{2m\omega}(1 + 2n). \quad (\text{A.24})$$

At a temperature T , the occupation of the modes is described by the boltzmann distribution:

$$\langle z^2 \rangle_T = \sum_{n=0}^{\infty} \frac{1}{Z} e^{-\beta E_n} \langle z^2 \rangle_n, \quad (\text{A.25})$$

where $\beta = 1/k_B T$, $E_n = \hbar\omega(n + 1/2)$ is the energy of mode n and

$$Z = \sum_{n=0}^{\infty} e^{-\beta E_n} = \frac{e^{-\beta \frac{\hbar\omega}{2}}}{1 - e^{-\beta \hbar\omega}} \quad (\text{A.26})$$

is the partition function. Using known series, the expression eq. (A.25) can be evaluated to

$$(\Delta z)_T^2 = \langle z^2 \rangle_T = \frac{\hbar}{2m\omega} \sum_{n=0}^{\infty} \frac{1}{Z} [e^{-\beta E_n} + 2ne^{-\beta E_n}] \quad (\text{A.27})$$

$$= \frac{\hbar}{2m\omega} \left[1 + \frac{2}{Z} \sum_{n=0}^{\infty} n e^{-\beta E_n} \right] \quad (\text{A.28})$$

$$= \frac{\hbar}{2m\omega} \left[1 + \frac{2e^{-\beta \hbar\omega}}{1 - e^{-\beta \hbar\omega}} \right] = \frac{\hbar}{2m\omega} \coth\left(\frac{\hbar\omega}{2k_B T}\right) \quad (\text{A.29})$$

B Primary calculations

B.1 Average density matrix

The series expansions of the Casimir terms in the PFA $1/(\mathcal{L}_{A(B)}^i)^2$ from eq. (4.7) are given by:

$$\begin{aligned} \frac{1}{(\mathcal{L}_{A(B)}^i)^2} &\approx \frac{4}{(d-2L+2R)^2} \pm \frac{8\Delta x_{A(B)} \sin \delta}{(d-2L+2R)^3} \pm \theta_{A(B)} \left(\frac{8\Delta x_{A(B)} \cos \delta}{(d-2L+2R)^3} \right) \\ &+ L_{A(B)} \left(\frac{16}{(d-2L+2R)^3} \pm \frac{48\Delta x_{A(B)} \sin \delta}{(d-2L+2R)^4} \right) \pm \theta_{A(B)} L_{A(B)} \frac{48\Delta x_{A(B)} \cos \delta}{(d-2L+2R)^4} \quad (\text{B.1}) \end{aligned}$$

where again the abbreviation $\delta = \alpha, \beta$ was used and the \pm terms align to the corresponding notation in eq. (4.7). The series expansion for the gravitational terms $1/L^{ij}$ with $i, j = 1, 2$ from eq. (4.10) is given by

$$\begin{aligned} \frac{1}{L^{ij}} &= \frac{1}{2L} \pm \frac{\Delta x_B \sin \beta - \Delta x_A \sin \alpha}{8L^2} \mp \theta_A \frac{\Delta x_A \cos \alpha}{8L^2} \pm \theta_B \frac{\Delta x_B \cos \beta}{8L^2} \\ &+ L_A \left(-\frac{1}{4L^2} \pm \frac{\Delta x_A \sin \alpha - \Delta x_B \sin \beta}{8L^3} \right) + L_B \left(-\frac{1}{4L^2} \pm \frac{\Delta x_A \sin \alpha - \Delta x_B \sin \beta}{8L^3} \right) \\ &\pm L_A \theta_A \frac{\Delta x_A \cos \alpha}{8L^3} \mp L_A \theta_B \frac{\Delta x_B \cos \beta}{8L^3} \pm L_B \theta_A \frac{\Delta x_A \cos \alpha}{8L^3} \mp L_B \theta_B \frac{\Delta x_B \cos \beta}{8L^3} \\ &+ L_A L_B \left(\frac{2}{4L^3} \pm \frac{3\Delta x_B \sin \beta - 3\Delta x_A \sin \alpha}{16L^4} \right) \\ &\mp L_A L_B \theta_A \frac{3\Delta x_A \cos \alpha}{16L^4} \pm L_A L_B \theta_B \frac{3\Delta x_B \cos \beta}{16L^4} \quad (\text{B.2}) \end{aligned}$$

The resulting average over $\theta_{A(B)}$ and $L_{A(B)}$ can be computed by

$$\int_{-\infty}^{\infty} d\theta_A d\theta_B dL_A dL_B p(\theta_A) p(\theta_B) p(L_A) p(L_B) e^{i\phi} \quad (\text{B.3})$$

where $p(\cdot)$ is a gaussian probability distribution in the form of

$$p(x) = \frac{1}{\sqrt{2\pi}\Delta x} e^{-\frac{x^2}{2(\Delta x)^2}} \quad (\text{B.4})$$

and ϕ is, as seen in the expansions above, linear in θ_i and L_i with occasional mixed terms. These mixed terms (here denoted by $\Delta A, \Delta B$ for either $\Delta\theta$ or ΔL) can be neglected in

first order because in the final result, they appear in the form of

$$\sim \exp\left\{-\frac{a^2(\Delta A)^2}{2b^2(\Delta A)^2(\Delta B)^2+2}\right\} \rightarrow 1 \quad (\text{B.5})$$

which tends to one for small variations $\Delta A, \Delta B \ll 1$ (a, b are constants). Each averaged element of the density matrix can therefore be analytically calculated using

$$\prod_{\Delta A=\{\Delta\theta_{A(B)}, \Delta L_{A(B)}\}} \int_{-\infty}^{\infty} dA \frac{1}{\sqrt{2\pi}\Delta A} e^{-\frac{A^2}{2(\Delta A)^2}} e^{i\xi A} e^{i\phi} = \prod_{\Delta A} e^{-\frac{\xi^2(\Delta A)^2}{2}} e^{i\phi} \quad (\text{B.6})$$

where again ξ is the lengthy linearized phase proportional to the series expansions above *and proportional to t* and ϕ is again the lengthy part of the phase independent of the integration parameter A .

As an example, the value of the element $\langle\rho_{12}\rangle$ is given: During time evolution, this element corresponding to $|\psi_A^1\psi_B^1\rangle\langle\psi_A^1\psi_B^1|$ picks up the phase (notation from section 4.1)

$$\phi = \phi_{A,\text{Casimir}}^1 + \phi_{B,\text{Casimir}}^1 - \phi_{A,\text{Casimir}}^1 - \phi_{B,\text{Casimir}}^2 + \phi_{\text{Gravity}}^{11} - \phi_{\text{Gravity}}^{12}. \quad (\text{B.7})$$

According to (B.3) and (B.6), the average density matrix element can be calculated analytically yielding

$$\langle\rho_{12}\rangle \approx \exp\left\{i\left(-\xi_{\text{Casimir}}\frac{16\Delta x_B \sin\beta}{(d-2L+2R)^3} + \zeta_{\text{Gravity}}\frac{\Delta x_B \sin\beta}{4L^2}\right)t + \mathcal{O}(\Delta x_A \Delta x_B)\right\} \quad (\text{B.8})$$

$$\exp\left\{-\left(\frac{16\Delta x_B \cos\beta}{(d-2L+2R)^3}\xi_{\text{Casimir}} - \frac{\Delta x_B \cos\beta}{4L^2}\zeta_{\text{Gravity}}\right)^2 \frac{(\Delta\theta_B)^2}{2}t^2\right\} \quad (\text{B.9})$$

$$\exp\left\{-\left(\frac{\Delta x_B \sin\beta}{4L^3}\zeta_{\text{Gravity}}\right)^2 \frac{(\Delta L_A)^2}{2}t^2\right\} \quad (\text{B.10})$$

$$\exp\left\{-\left(\frac{96\Delta x_B \sin\beta}{(d-2L+2R)^4}\xi_{\text{Casimir}} + \frac{\Delta x_B \sin\beta}{4L^3}\zeta_{\text{Gravity}}\right)^2 \frac{(\Delta L_B)^2}{2}t^2\right\} \quad (\text{B.11})$$

where

$$\xi_{\text{Casimir}} = \frac{c\pi^3}{720} \left(\frac{\varepsilon_r - 1}{\varepsilon_r + 1}\right) \varphi(\varepsilon_r) R \quad \text{and} \quad \zeta_{\text{Gravity}} = \frac{GM_A M_B}{\hbar} \quad (\text{B.12})$$

was used.

In the special case of $\Delta L_A = \Delta L_B$ and $\Delta\theta_A = \Delta\theta_B$ (or due to symmetry the other way around), $\Delta x_A = \Delta x_B$ and $\alpha = \pm\beta \equiv \delta$ the averaged density matrix is given by

$$\langle\rho\rangle = \frac{1}{4} \begin{pmatrix} 1 & e^{i\Delta\phi_1}e^{-\gamma} & e^{i\Delta\phi_2}e^{-\gamma} & e^{i(\Delta\phi_1+\Delta\phi_2)}e^{-2\gamma} \\ & 1 & e^{-i(\Delta\phi_1-\Delta\phi_2)}e^{-2\gamma} & e^{i\Delta\phi_2}e^{-\gamma} \\ & & 1 & e^{i\Delta\phi_1}e^{-\gamma} \\ & & & 1 \end{pmatrix} \quad (\text{B.13})$$

where $\Delta\phi_1 = \pm\Delta\phi_2$ are the phases due to gravity, dependent on the orientation α, β which are in the parallel orientation given by eq. (2.15) and

$$\gamma = \left(\frac{16\Delta x \cos \delta}{(d-2L+2R)^3} \xi_{\text{Casimir}} - \frac{\Delta x \cos \delta}{4L^3} \zeta_{\text{Gravity}} \right)^2 \frac{(\Delta\theta)^2}{2} t^2 + \left(\frac{96\Delta x \sin \delta}{(d-2L+2R)^4} \xi_{\text{Casimir}} + \frac{\Delta x \sin \delta}{2L^3} \zeta_{\text{Gravity}} \right)^2 \frac{(\Delta L)^2}{2} t^2 \quad (\text{B.14})$$

The resulting logarithmic negativity can be computed with **Mathematica** using $\Delta\phi$ defined in eq. (4.15) to

$$E_N(\langle\rho\rangle) \approx \max \left\{ 0, \log_2 \left(e^{-\gamma} (\cosh(\gamma) + |\sin(\Delta\phi)|) \right) \right\} \quad (\text{B.15})$$

$$= \log_2 \left(\frac{1}{2} e^{-\gamma} (|\sin \Delta\phi - \sinh \gamma| + |\sin \Delta\phi + \sinh \gamma| + 2 \cosh \gamma) \right) \quad (\text{B.16})$$

For general combinations of $\Delta L_A, \Delta L_B, \Delta\theta_A, \Delta\theta_B$, and more complex orientations, the logarithmic negativity of $\langle\rho\rangle$ was computed numerically.

B.2 Density matrix vibrating plate

The separations between the shield and the Particle state $A(B)_i$ in the parallel configuration are given by

$$d_{A(B)}^i = L \pm_{A(B)} z \left(|u| \mp_i |\nabla u| \frac{\Delta x}{2} \right) \quad (\text{B.17})$$

where the first \pm distinguishes between particle A and B and the second one between $i = 1$ and $i = 2$. The gravitational interaction is given as before in chapter 2. After averaging over z (normally distributed around $\langle z \rangle = 0$ and std. Δz) the resulting density matrix is now given by

$$\langle\rho\rangle = \frac{1}{4} \begin{pmatrix} 1 & e^{i\Delta\phi} e^{-\frac{1}{2}(\xi_{\text{Cas}})^2(\Delta z)^2} & e^{i\Delta\phi} e^{-\frac{1}{2}(\xi_{\text{Cas}})^2(\Delta z)^2} & 1 \\ & 1 & e^{-\frac{1}{2}(2\xi_{\text{Cas}})^2(\Delta z)^2} & e^{-i\Delta\phi} e^{-\frac{1}{2}(\xi_{\text{Cas}})^2(\Delta z)^2} \\ & & 1 & e^{-i\Delta\phi} e^{-\frac{1}{2}(\xi_{\text{Cas}})^2(\Delta z)^2} \\ & & & 1 \end{pmatrix} \quad (\text{B.18})$$

with

$$\Delta\phi = \frac{GM_A M_B}{\hbar} \left(\frac{1}{4L^2} - \frac{1}{\sqrt{2L + (\Delta x)^2}} \right) t \quad (\text{B.19})$$

$$\xi_{\text{Cas}} = \frac{c\pi^3 R}{720} \left(\frac{\varepsilon_r - 1}{\varepsilon_r + 1} \right) \varphi(\varepsilon_r) \cdot \frac{2|\nabla u| \Delta x}{\mathcal{L}^3} t \quad (\text{B.20})$$

which is only dependent on the gradient of the shape $|\nabla u|$. The logarithmic negativity is given by

$$E_N(\langle \rho \rangle) = \log_2 \left\{ \frac{1}{4} \left(3 + e^{-4\gamma} + \sqrt{(1 - e^{-4\gamma})^2 + 16e^{-2\gamma} \sin^2 \Delta\phi} \right) \right\} \quad (\text{B.21})$$

where

$$\gamma = \frac{1}{2}(\xi_{\text{Cas}})^2(\Delta z)^2. \quad (\text{B.22})$$

B.3 Time evolution in front of a thermal plate

The time evolution operator $\hat{U} = e^{-i\hat{H}t/\hbar}$ of the hamiltonian eq. (5.29) can be calculated in the interaction picture using the “Magnus expansion” [68]. In the following calculations, the direct gravitational interactions between the two particles are ignored as they don’t depend on the shield vibrations at all. The final evolution due to these couplings were already studied in chapter 4 and can just be added in the end. The interaction picture hamiltonian in the $\{|\psi_A^1\psi_B^1\rangle, |\psi_A^1\psi_B^2\rangle, |\psi_A^2\psi_B^1\rangle, |\psi_A^2\psi_B^2\rangle\}$ -basis is given by

$$\hat{H}_{\text{int}} = \sum_{m \in \{(k,l)\}} \begin{pmatrix} g_{A,m}^1 + g_{B,m}^1 & & & \\ & g_{A,m}^1 + g_{B,m}^2 & & \\ & & g_{A,m}^2 + g_{B,m}^1 & \\ & & & g_{A,m}^2 + g_{B,m}^2 \end{pmatrix} (\hat{a}e^{-i\omega_m t} + \hat{a}^\dagger e^{i\omega_m t}) \quad (\text{B.23})$$

The operator at the beginning is referred to as \hat{G} in the following. The time evolution in the Magnus expansion here given by [68]

$$\hat{U}(t) = \exp \left\{ -\frac{i}{\hbar} \int_0^t dt_1 \hat{H}_{\text{int}}(t_1) - \frac{1}{2\hbar^2} \int_0^t dt_1 \int_0^{t_1} dt_2 [\hat{H}_{\text{int}}(t_1), \hat{H}_{\text{int}}(t_2)] \right\}. \quad (\text{B.24})$$

All higher order terms vanish, so this is an exact result. After substitution, the result is given by

$$\hat{U}(t) = \exp \left\{ \hat{G}(f_1 \hat{a}^\dagger - f_1^* \hat{a}) + i\hat{G}^2 f_2 \right\} \quad (\text{B.25})$$

$$= \hat{D} \left(f_1 (g_{A,m}^1 + g_{B,m}^1) \right) \exp \left\{ i f_2 (g_{A,m}^1 + g_{B,m}^1)^2 \right\} |\psi_A^1 \psi_B^1\rangle \langle \psi_A^1 \psi_B^1| + \dots \quad (\text{B.26})$$

with

$$f_1 = \frac{(1 - e^{i\omega_m t})}{\hbar\omega_m} \quad \text{and} \quad f_2 = \frac{t\omega_m - \sin(t\omega_m)}{\hbar^2\omega_m^2} \quad (\text{B.27})$$

and the displacement operator $\hat{D}(\alpha) = \exp\{\alpha\hat{a}^\dagger - \alpha^*\hat{a}\}$. The evolved state $\rho(t) = \hat{U}(t)\rho_0\hat{U}^\dagger(t)$ is now given by

$$\begin{aligned} \rho(t) = & \bigotimes_{m \in \{(k,l)\}} \hat{D}(f_1(g_A^1 + g_B^1)) \rho_{\text{th},m} \hat{D}^\dagger(f_1(g_A^1 + g_B^1)) \otimes \frac{1}{4} |\psi_A^1 \psi_B^1\rangle\langle\psi_A^1 \psi_B^1| \\ & + \hat{D}(f_1(g_A^1 + g_B^1)) \rho_{\text{th},m} \hat{D}^\dagger(f_1(g_A^1 + g_B^2)) \otimes \frac{1}{4} e^{if_2(g_A^1 + g_B^1)^2} |\psi_A^1 \psi_B^1\rangle\langle\psi_A^1 \psi_B^2| e^{-if_2(g_A^1 + g_B^2)^2} \\ & + \dots \\ & + \hat{D}(f_1(g_A^2 + g_B^2)) \rho_{\text{th},m} \hat{D}^\dagger(f_1(g_A^2 + g_B^1)) \otimes \frac{1}{4} e^{if_2(g_A^2 + g_B^2)^2} |\psi_A^2 \psi_B^2\rangle\langle\psi_A^2 \psi_B^1| e^{-if_2(g_A^2 + g_B^1)^2} \\ & + \hat{D}(f_1(g_A^2 + g_B^2)) \rho_{\text{th},m} \hat{D}^\dagger(f_1(g_A^2 + g_B^2)) \otimes \frac{1}{4} |\psi_A^2 \psi_B^2\rangle\langle\psi_A^2 \psi_B^2| \end{aligned} \quad (\text{B.28})$$

We are interested in the evolution of the two-particle system. This is given by tracing out the thermal shield $\rho_{\text{sys.}} = \text{tr}_{th} \{\rho(t)\}$. Using $\text{tr}\{A \otimes B\} = \text{tr}\{A\} \text{tr}\{B\}$, it follows:

$$\rho_{\text{sys.}} = \frac{1}{4} \begin{pmatrix} 1 & \text{tr}_m \text{tr} \left\{ \hat{D}(f_1(g_A^1 + g_B^1)) \rho_{\text{th},m} \hat{D}^\dagger(f_1(g_A^1 + g_B^2)) \right\} e^{if_2((g_A^1 + g_B^1)^2 - (g_A^1 + g_B^2)^2)} & \dots \\ \vdots & \ddots & \end{pmatrix} \quad (\text{B.29})$$

To calculate $\text{tr}\{\hat{D}(\zeta_i) \rho_{\text{th}} \hat{D}^\dagger(\zeta_j)\}$, we expand ρ_{th} into coherent states [57]

$$\rho_{\text{th}} = \int d\alpha^2 \frac{1}{\bar{n}\pi} e^{-\frac{|\alpha|^2}{\bar{n}}} |\alpha\rangle\langle\alpha| \quad (\text{B.30})$$

and calculate the required trace [57]:

$$\text{tr}\{\hat{D}(\zeta_i) \rho_{\text{th}} \hat{D}^\dagger(\zeta_j)\} = \exp\left\{\phi - |\Delta\zeta|^2 \left(\frac{1}{2} + \bar{n}\right)\right\} \quad (\text{B.31})$$

where $\Delta\zeta = \zeta_i - \zeta_j$ and $\phi = (\zeta_j^* \zeta_i - \zeta_j \zeta_i^*)/2 = 0$. The final decoherence elements of the evolved state therefore all have the form

$$e^{-\gamma_{1,2}} = \exp\left\{-\sum_m \left|(g_{A,m}^1 + g_{B,m}^1) - (g_{A,m}^1 + g_{B,m}^2)\right|^2 f_1 f_1^* \left(\frac{1}{2} + \bar{n}_m\right)\right\} \quad (\text{B.32})$$

C Additional figures

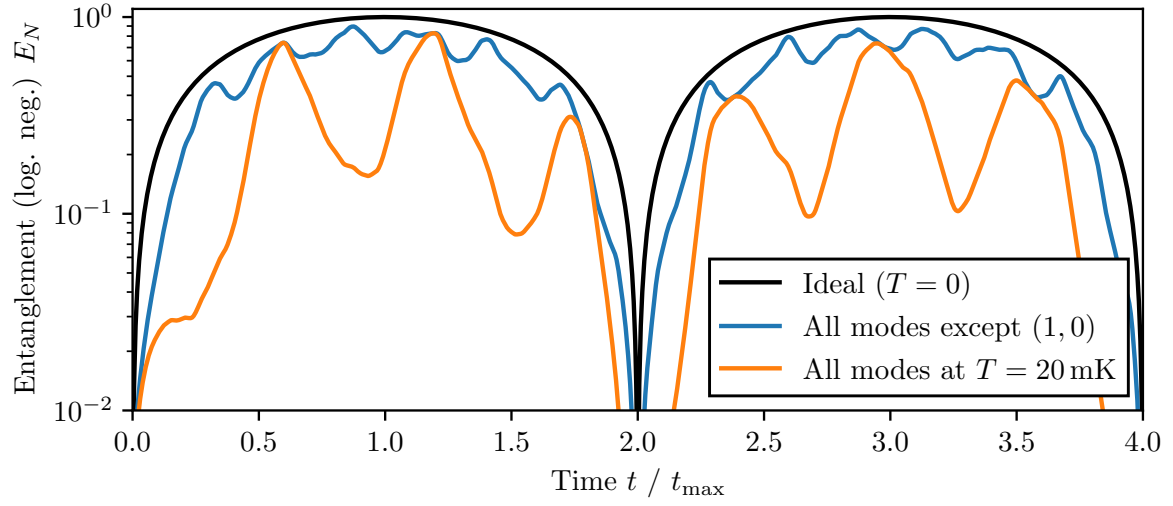


Figure C.1: Similar to fig. 5.7 at $T = 20$ mK for a slightly smaller shield with $r_s = 5$ mm.